Conf-9106329--1

Fermi National Accelerator Laboratory

FNAL/C--91/341-E

DE92 007202 -E

The Physics of Proton Antiproton Collisions

M. Shochet

Enrico Fermi Institute and Department of Physics, University of Chicago
Chicago, Illinois 60637

December 1991

*Lectures from Les Houches Summer School, *Particles in the 90s, Ecole d'Ete de Physique Theorique*, Les Houches, France, June 30-July 26, 1991.

MASTER

DISTRIBUTION OF THIS DOCUMENT IS UNLIMITED

Operated by Universities Research Association Inc. under Contract No. DE-AC02-76CHO3000 with the United States Department of Energy

Disclaimer

This report was prepared as an account of work sponsored by an agency of the United States Government. Neither the United States Government nor any agency thereof, nor any of their employees, makes any warranty, express or implied, or assumes any legal liability or responsibility for the accuracy, completeness, or usefullness of any information, apparatus, product, or process disclosed, or represents that its use would not infringe privately owned rights. Reference herein to any specific commercial product, process, or service by trade name, trademark, manufacturer, or otherwise, does not necessarily constitute or imply its endorsement, recommendation, or favoring by the United States Government or any agency thereof. The views and opinions of authors expressed herein do not necessarily state or reflect those of the United States Government or any agency thereof.

CDF/PUB/CDF/PUBLIC/1637
FERMILAB-CONF-91/341-E
December 3, 1991

THE PHYSICS OF PROTON ANTIPROTON COLLISIONS

MELVYN J. SHOCHET

Enrico Fermi Institute and Department of Physics,
University of Chicago,
Chicago, IL 60637,
USA

Lectures delivered at the Les Houches Summer School, July 1991

Published Lectures from Les Houches Summer School, Particles in the 90's,
Ecole d'Ete de Physique Theorique, Les Houches, France, June 30-July 26, 1991.

Contents

1. Accelerator and Detector 5
   1.1. Accelerator 5
   1.2. Detector 13
2. QCD Studies 21
   2.1. Essential Features of QCD 21
   2.2. QCD in $\bar{p}p$ Collisions 24
   2.3. Dijet Production 28
   2.4. Multjet Production 30
   2.5. Large P_T γ, W, and Z Production 34
3. Studies of the Electroweak Force 37
   3.1. Overview of the Standard Model 37
   3.2. The W Mass 41
   3.3. Charge Asymmetries 46
      3.3.1. $q\bar{q} \to e^+e^-$ 46
      3.3.2. $W \to e\nu$ 47
   3.4. The W Lifetime 50
   3.5. Lepton Universality at $q^2 = M_W^2$ 51
4. The Search for the Top Quark 53
   4.1. Introduction 53
   4.2. $t\bar{t} \to e\mu X$ 55
   4.3. $t\bar{t} \to e\nu +$ jets 60
   4.4. Extended Dilepton Search 64
   4.5. Extended Single Lepton Search 66
   4.6. Top Searches at the $Sp\bar{p}S$ Collider 69
5. b Physics at Hadron Colliders 71
   5.1. b Production 72
      5.1.1. Inclusive Lepton Channels 73
      5.1.2. Inclusive J/ψ Channels 78
      5.1.3. Exclusive Final States 80
   5.2. $B^0 \to \mu^+\mu^-$ 83
   5.3. $B^0, \overline{B}^0$ Mixing 84
6. The Search for Exotic Objects and Prospects for the Future 88
   6.1. The Search for Exotic Objects 88
      6.1.1. Heavy Z Bosons 88
      6.1.2. Heavy W Bosons 89
      6.1.3. Quark Compositeness 90
      6.1.4. Supersymmetry 92
   6.2. Collider Physics with the Fermilab Main Injector 94
      6.2.1. Search for the Top Quark 95
      6.2.2. Precision Measurement of the W Mass 98
      6.2.3. The W Lifetime and Hidden Top 98

6.2.4. Vector Boson Pair Production 99
6.2.5. Other Heavy Particles 100
6.2.6. B Physics 100
7. Acknowledgements 103
References 103

1. Accelerator and Detector

Since this is a set of experimental lectures, I will begin with an introduction to the experimental tools which allow the physics issues to be attacked. First we will look at the accelerator with a special emphasis on the production of antiprotons. Then we will briefly consider the elements of a large general purpose collider detector.

1.1. Accelerator

Much of the success of both the CERN and Fermilab hadron collider programs is due to the achievement of the accelerator physicists in providing very large collision rates of high energy protons and antiprotons.

The accelerator energy is critical for many physics processes such as high Q^2 QCD scattering, W production, top quark production, b quark production, and SUSY production (Fig. 1). In each case, to get high mass or Q^2, energetic initial state partons are needed. Since the parton distribution in the proton is peaked at small $x = P_{parton}/P_{proton}$ (Fig. 2), a high flux of energetic partons requires large proton energy.

To observe processes with small production cross sections, a large number of $\bar{p}p$ collisions must occur. The parameter that gives the rate of collisions is the luminosity, defined by the relation $N = \sigma L$, where N is the number of events produced per second for some final state, σ is the production cross section for that state, and L is the luminosity in units of $cm^{-2} - sec^{-1}$. Thus if the Fermilab Collider reaches a luminosity of $1 \times 10^{31} cm^{-3} - sec^{-1}$ next year, the total rate of inelastic collisions will be 0.5 MHz, since the inelastic cross section is $50 \times 10^{-27} cm^2$.

For an accelerator in which the particles are distributed in bunches rather than continuously around the ring, the luminosity is given by

$$L = \frac{N_p N_{\bar{p}} B f_0}{4\pi\sigma^2}$$

where N_p ($N_{\bar{p}}$) is the number of protons (antiprotons) in each bunch, B is the number of bunches of each type in the accelerator, f_0 is the revolution frequency of the accelerator (50 KHz for Fermilab), and σ is the transverse cross sectional size of the bunches.

The transverse bunch size, σ, is determined by both the characteristics of the beam and the magnetic focusing properties of the accelerator. The beam emittance ($\epsilon \equiv \int dx' dx$) is the phase space area occupied by the beam (Fig. 3). Often the invariant emittance $\epsilon_N \equiv \gamma\epsilon$ is used. It is more nearly independent of the beam energy because of the natural compacting of phase space by the Lorentz transformation. A particle with momentum components P_x and P_z in the bunch rest frame will have an angle in the lab frame (x') that is inversely proportional to the Lorentz factor, γ, connecting

the bunch rest frame and the lab frame because P_z is Lorentz boosted while P_x is an invariant.

The focusing properties of the accelerator quadrupoles produce a phase space rotation of the beam (Fig. 4). For a particle with coordinates ($x_0 = 0$, x'_0) at location A, the position at location B is

$$x = \sqrt{\beta\beta_0} sin\phi x'_0$$

where ϕ is the phase advance and the magnitude of the oscillation is determined by the β function whose value at each point around the ring depends on the configuration of the accelerator's quadrupole magnets. The luminosity is maximized by having the minimum value of the β function (β^*) located at the $\bar{p}p$ collision point in the center of the detector. The minimum β occurs when the phase space ellipse has its major axis oriented vertically in the (x, x') plane.

In terms of the beam emittance and β^*, the transverse bunch size is

$$\pi\sigma^2 = \epsilon\beta^* = \frac{\epsilon_N\beta^*}{\gamma}$$

Since the proton and antiproton beams can have different emittances, the effective bunch size for a collider is

$$\sigma^2 = \frac{\beta^*}{\pi\gamma}\left(\frac{\epsilon_N^p + \epsilon_N^{\bar{p}}}{2}\right)$$

Thus to maximize the luminosity, β^* and the beam emittance should be minimized, and the beam energy or γ should be maximized.

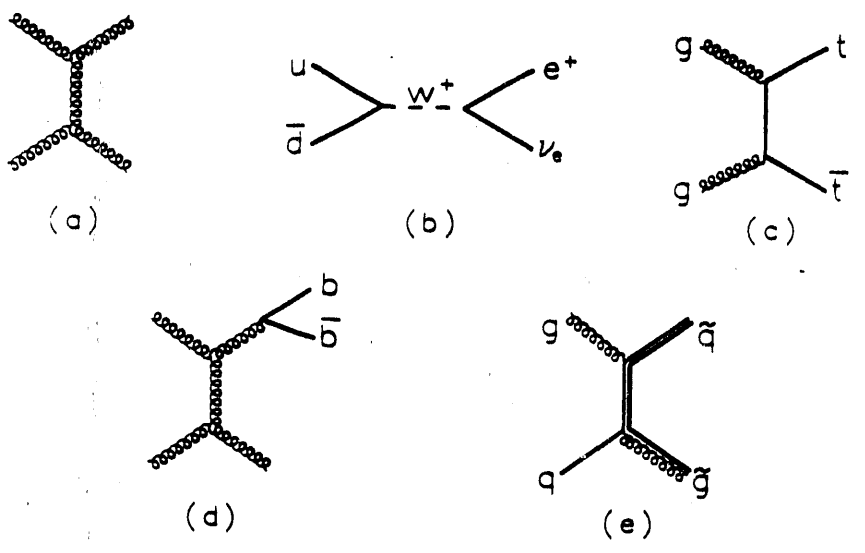

Fig. 1. Production diagrams for (a) high Q^2 QCD scattering, (b) W production, (c) top quark production, (d) b quark production, and (e) SUSY production.

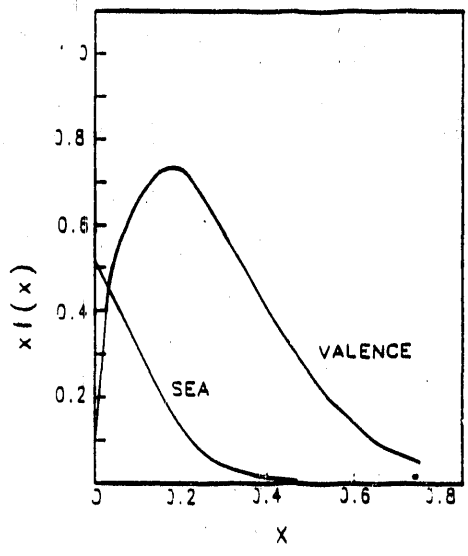

Fig. 2. The valence and sea quark distribution functions. Note that these are momentum densities; to get the number densities, divide the functions by x.

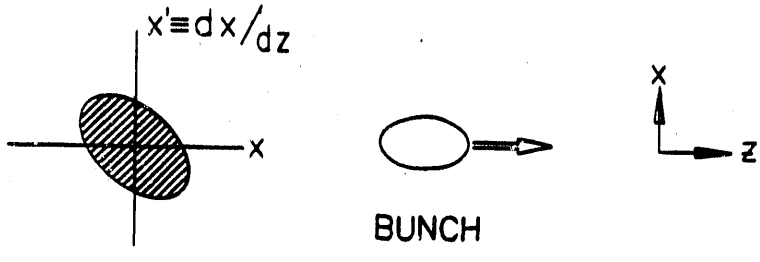

Fig. 3. The phase space diagram for one of the directions perpendicular to the beam direction.

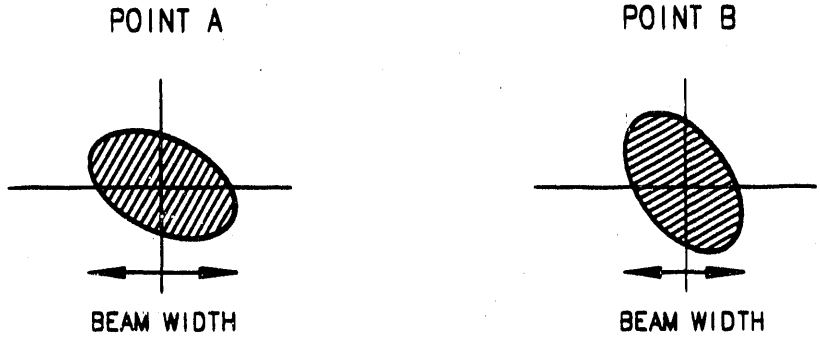

Fig. 4. The phase space rotation of the beam between two locations around the accelerator. The width of the beam at each location is indicated.

A sketch of the accelerator complex at Fermilab is shown in Fig. 5. Protons are accelerated to 200 MeV in the Linac and then to 8 GeV in the Booster accelerator. The protons are then transferred to the Main Ring, the original Fermilab accelerator located in the large tunnel. Here the protons are accelerated to 120 GeV. They are then extracted and strike the antiproton target. Antiprotons with momentum near 8 GeV/c are collected, stored, and phase space compressed in the Debuncher and Accumulator rings. When the $\overline{p}$ intensity is sufficiently large, the antiprotons are reinjected into the Main Ring where they are accelerated to 150 GeV and then transferred into the Tevatron, the superconducting accelerator that is located just below the Main Ring in the Fermilab tunnel. The Tevatron also contains bunches of protons that were injected from the Main Ring just before the antiprotons were transferred out of the Accumulator. The counter-rotating p and $\overline{p}$ Tevatron beams are then accelerated together up to 900 GeV. Finally the focussing quadrupoles are raised to full power to obtain the minimum β^* and thus the maximum luminosity.

Let us consider the antiproton collection system [1] in more detail. The central problem is to produce and collect a large number of antiprotons with small enough momentum spread and angular divergence to be captured with high efficiency in the Main Ring and Tevatron accelerators. In the proton-nucleus collisions in the target, antiprotons are produced with a large angular divergence. A lithium lens (Fig. 6a) is used to focus the antiprotons into a beam. Lithium is the material of choice because it is the conductor with the smallest atomic number. A very large focusing magnetic field gradient is produced when a 0.5×10^6 ampere current pulse passes down the length of the lens. This can be easily seen by considering an Ampere circuit as shown in Fig. 6b.

$$\begin{aligned}
\oint \boldsymbol{B} \cdot d\boldsymbol{l} &= \mu_0 i = \mu_0 \int \boldsymbol{j} \cdot d\boldsymbol{a} \\
B 2\pi r &= \mu_0 \frac{I}{\pi R^2} \pi r^2 \\
B &= \frac{\mu_0 I}{2\pi R^2} r \\
\frac{dB}{dr} &= \frac{\mu_0 I}{2\pi R^2} \\
&= 1000 \text{ Tesla/meter}
\end{aligned}$$

Both the maximum proton flux striking the target and the maximum current in the lens are limited by the thermal properties of the materials (melting point and effects of thermal shock).

The antiproton beam is transported from the lithium lens to the Debuncher ring where a phase space rotation reduces the longitudinal momentum spread. The longitudinal phase space area ($\Delta p_z \Delta z$) remains constant, with Δp_z decreasing as Δz increases. The antiproton beam entering the Debuncher has the same bunched structure as the proton beam that struck the antiproton target (Fig. 7). The phase space rotation causes the bunches to become wider spatially, and consequently narrower in momentum (Fig 8). Before the antiproton beam leaves the Debuncher, its momentum spread is reduced from 3.5% to 0.2%.

The Accumulator ring receives pulses of antiprotons from the Debuncher, stores the antiprotons for up to 24 hours until $> 2 \times 10^{11}$ antiprotons are in the Accumulator, and during that time reduces the momentum spread ("cools" the beam) in all three

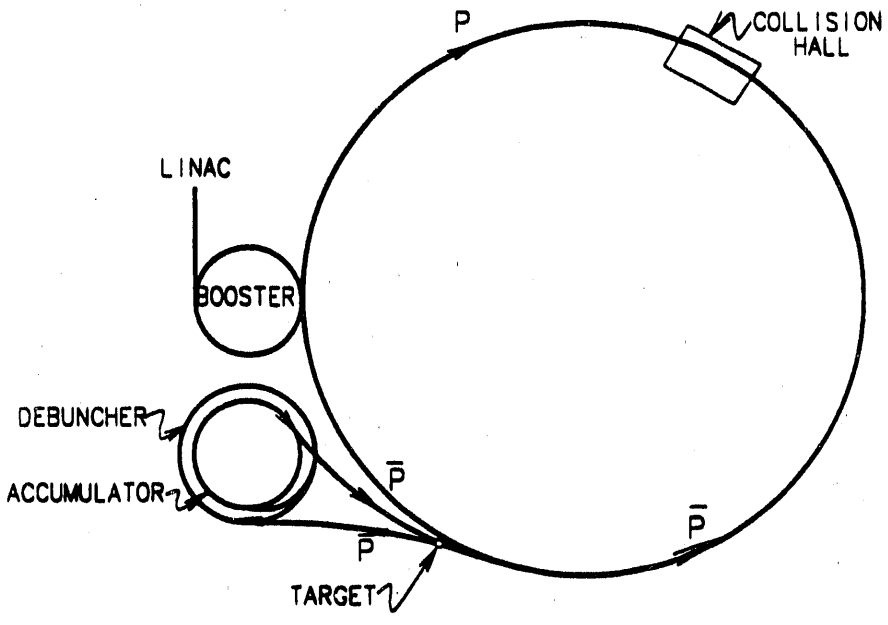

Fig. 5. The Fermilab Accelerator Complex.

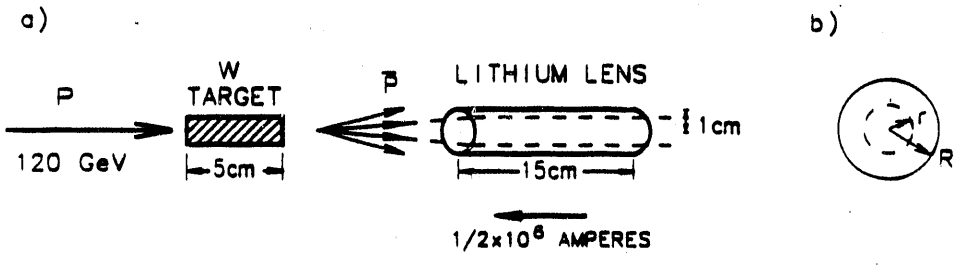

Fig. 6. (a) The lithium lens follows the $\bar{p}$ production target. (b) A transverse cross section of the lens with an Ampere circuit of radius r.

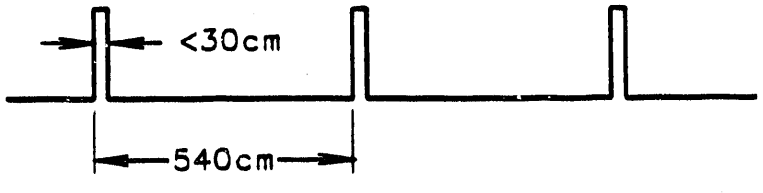

Fig. 7. The bunch structure of the antiproton beam entering the Debuncher.

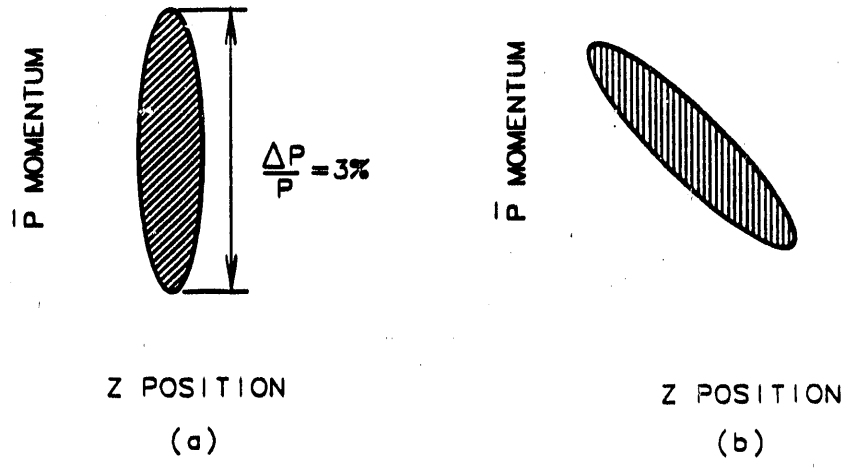

Fig. 8. The parti'' density within a bunch in longitudinal phase space (a) when the beam enters the debuncher and (b) after 30 turns in the debuncher.

dimensions so that the beam can be efficiently captured in the Main Ring accelerator. Cooling is achieved using Stochastic Cooling, sort of a legal Maxwell Demon.

The Stochastic Cooling system consists of a set of pick-ups, amplifiers, and beam kickers (Fig. 9). The pick-ups detect the position of an antiproton that is not on the central orbit of the Accumulator. The signal is amplified and sent across the ring where it reaches the kickers before the $\overline{p}$ does. The kickers apply an electric field in order to move the particle back onto the central orbit. Since the field also affects other nearby particles, noise is introduced into the system. Consequently the cooling process is quite slow. Figure 10 shows the antiproton energy distribution as a function of time after $\overline{p}$ accumulation begins. Notice that this is a logarithmic plot and that after 4 hours there is a very dense core with a width of only a few MeV.

The performance of the Fermilab Tevatron Collider during the 1988-89 run is summarized in Table 1. Using these numbers in the relation for luminosity does not give the expected result because the quoted invariant emittances are for 95% beam containment, i.e. they correspond to $3\sigma^2$ not σ^2.

During the next four years there will be a major upgrade of the Fermilab Collider [2]. The goal of the project is to reach a peak luminosity of at least 5×10^{31}. The most significant change will be replacing the Main Ring accelerator by a new superconducting Main Injector. As shown in Fig. 11, it will be built in a new tunnel adjacent to the Tevatron. The Main Injector will have a significantly larger phase space aperture for the beam and thus will be able to capture larger proton and antiproton fluxes. Moreover the new machine will have a 1.5 second cycle time, compared to the 2.5 second Main Ring cycle. Thus there will be a larger number of proton pulses per hour on the $\overline{p}$ target, and consequently a higher $\overline{p}$ production rate.

The number of proton and antiproton bunches in the Tevatron will also be increased

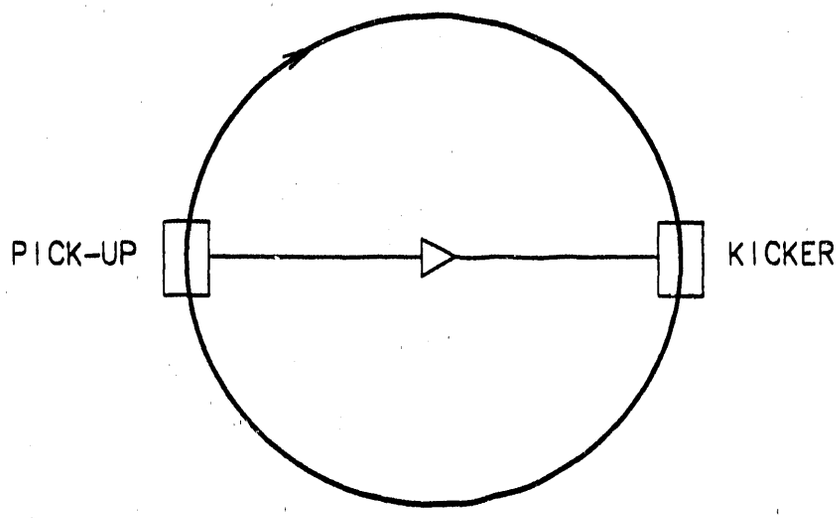

Fig. 9. A schematic representation of the Stochastic Cooling system. A pick-up on one side of the ring detects the $\bar{p}$ position. The signal is then amplified and sent to a kicker on the other side of the ring to move the $\bar{p}$ back onto the Accumulator's central orbit. The typical amplifier bandwidth is 2×10^9 Hz, with a gain of 3×10^7.

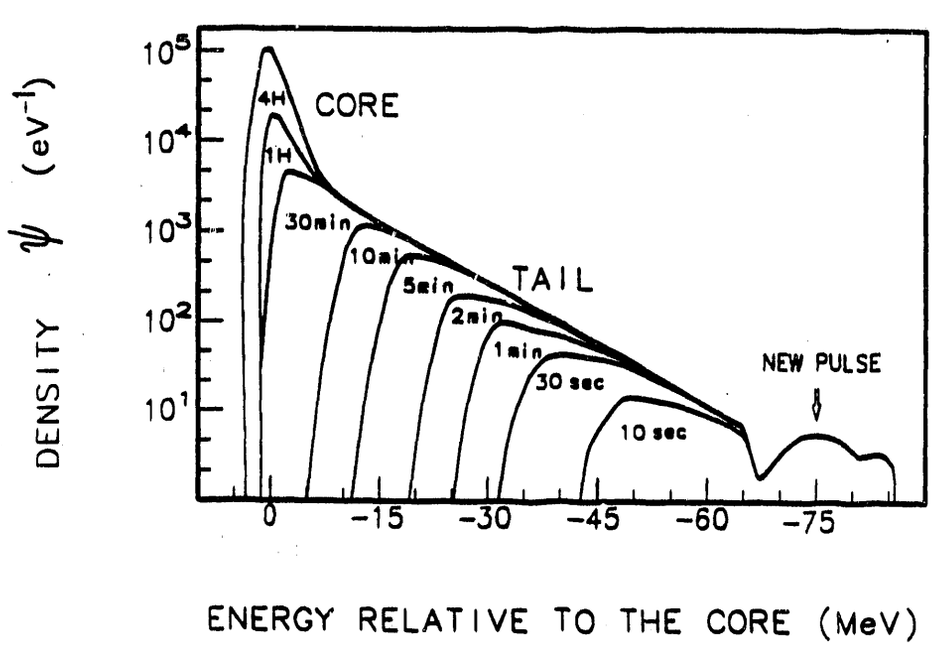

Fig. 10. The time evolution of the energy distribution of antiprotons in the Accumulator.

E	900 GeV
B	6
N_p	7×10^{10}
$N_{\bar{p}}$	3×10^{10}
ϵ_N^p	25π mm-mrad
$\epsilon_N^{\bar{p}}$	15π mm-mrad
β^*	0.5 m
L	$1.6 \times 10^{30} cm^{-2} - sec^{-1}$

Table 1
Fermilab Tevatron performance during the 1988-89 run

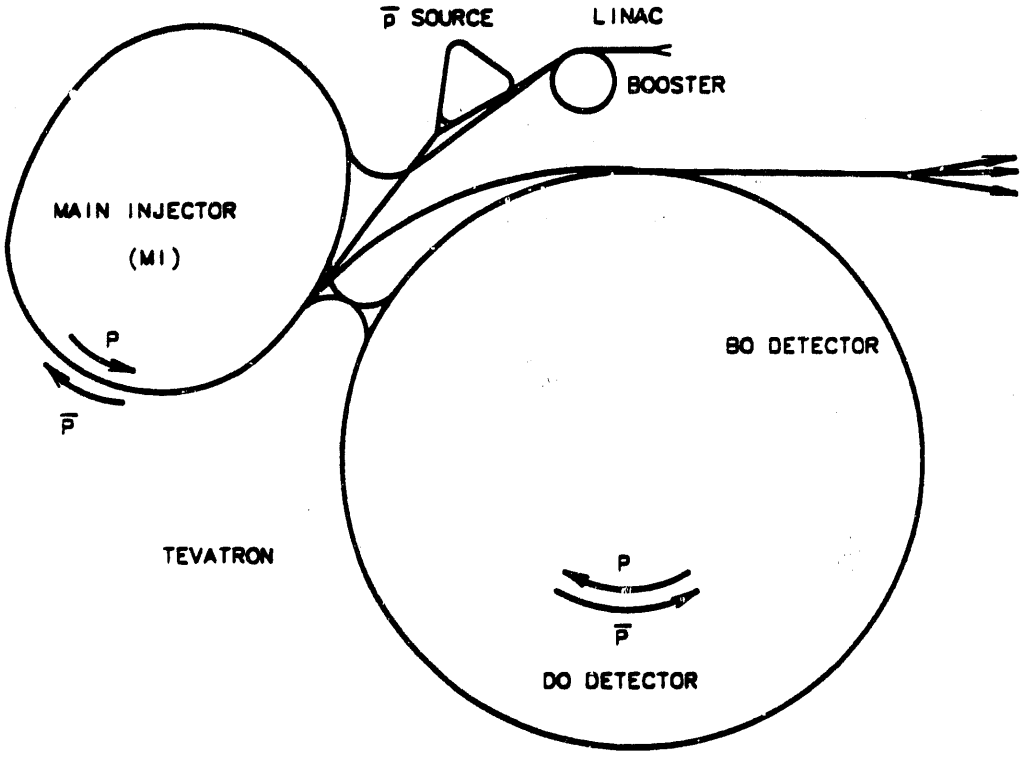

Fig. 11. The Fermilab accelerator complex as it will look after the Main Injector is built.

	1988-89	1996
E_{beam}	900 GeV (1.8 TeV E_{cm})	1 TeV (2 TeV E_{cm})
B	6	36
N_p	7×10^{10}	33×10^{10}
$N_{\bar{p}}$	3×10^{10} (18×10^{10} total)	3.7×10^{10} (134×10^{10} total)
ϵ_N^p	25π mm-mrad	30π mm-mrad
$\epsilon_N^{\bar{p}}$	15π mm-mrad	22π mm-mrad
β^*	0.5 m	0.5 m (0.25 m possible)
L	$1.6 \times 10^{30}\ cm^{-2} - sec^{-1}$	$5.5 \times 10^{31}\ cm^{-2} - sec^{-1}$

Table 2
Characteristics of the Fermilab Tevatron before and after the planned upgrade

as part of the accelerator improvement project. To see why this is necessary, we will calculate the mean number of $\bar{p}p$ interactions per bunch crossing at $L = 5 \times 10^{31} cm^{-2} - sec^{-1}$ assuming the number of bunches remains at 6 ($\Rightarrow$ 1 bunch crossing per 3.5 μsec). If R is the mean number of interactions per bunch crossing, and N is the mean number of interactions per second, then

$$\begin{aligned} R &= N \times 3.5 \times 10^{-6} sec \\ &= \sigma_{inel} L \times 3.5 \times 10^{-6} sec \\ &= (50 \times 10^{-27} cm^2)(5 \times 10^{31} cm^{-2} - sec^{-1})(3.5 \times 10^{-6} sec) \\ &= 8.75 \end{aligned}$$

Having 8 or 9 overlapping interactions would greatly complicate many measurements, including the W mass, top quark search, and secondary vertex identification in b events.

To solve this problem, the number of proton and antiproton bunches in the Tevatron will be increased from 6 to 36. However since the p and $\bar{p}$ bunches counter-rotate in the same accelerator ring, each antiproton bunch would pass through a proton bunch 72 times per revolution around the accelerator ring. The resulting long range electromagnetic interaction (beam-beam tuneshift) would cause the beam's emittance to blow up and the luminosity to be greatly reduced. This will be avoided with the use of 22 high field (35 KV/cm) electrostatic separators which will keep the protons and antiprotons in helical orbits that only intersect at the CDF and D0 detectors.

The expected improvement in the accelerator performance is shown in Table 2. With this and planned detector improvements, CDF should collect 100 times the 1988-89 data for each year of running after 1996.

1.2. Detector

The physics program at the colliders is determined to no small extent by the capabilities and limitations of the detectors. Here I will discuss the major components of a collider detector and indicate how leptons and hadrons are identified. To be concrete I will focus on CDF, but the essential elements, tracking and calorimetry, are common to most general purpose detectors at hadron and electron colliders.

The goal in the design of CDF was to detect and measure the momenta of electrons, muons, quarks and gluons (hadron jets), and neutrinos (through momentum imbalance)

over as much of the total solid angle as possible. A sketch of the detector is shown in Figure 12. A superconducting coil produces a 1.5 Tesla magnetic field uniform over the volume of the tracking chambers. There are two components to the tracking system. Adjacent to the beam pipe, a set of time projection chambers (VTPC) accurately locates the interaction vertex for each event. The large central tracking chamber (CTC) measures the radii of curvature in the B field of charged particles, and thus their momenta. Beyond the tracking chambers, a set of finely segmented electromagnetic and hadronic calorimeters covers most of the solid angle (polar angle, θ, between 2° and 178°; azimuthal angle, ϕ, between 0° and 360°). These calorimeters measure the energy of electrons, photons, and hadrons. Muons are detected in the central region by drift chambers that are outside of the calorimeters, and in the forward regions by chambers in front of and behind large magnetized iron toroids. The details of the design and construction of the CDF detector can be found in a series of articles in Nuclear Instruments and Methods [3].

The central tracking chamber makes 84 measurements of a charged particle's trajectory, each with an uncertainty of approximately 180 microns (Fig 13). This results in an uncertainty in the track curvature, $k \equiv \frac{1}{\text{radius of curvature}}$, of

$$\sigma_k = 0.5 \times 10^{-3} m^{-1}$$

Since the transverse momentum, $P_T \equiv \sqrt{P_x^2 + P_y^2}$, is related to the curvature by

$$P_T = \frac{0.3B}{k}$$

where P_T, B, and k are in units of GeV/c, Tesla, and meter^{-1} respectively, the curvature uncertainty translates into a P_T uncertainty of

$$\frac{\sigma_{P_T}}{P_T^2} = \frac{\sigma_k}{0.3B} = 1 \times 10^{-3}$$

$$\frac{\sigma_{P_T}}{P_T} = 0.001 P_T$$

This gives a P_T uncertainty of 4% for typical leptons from W decay ($P_T \approx M_W/2$).

The calorimeters consist of an electromagnetic section followed by a hadronic section. The electromagnetic calorimeter measures the energies of electrons, positrons, and photons by sampling the energy deposited in an electromagnetic cascade. The detector (Fig. 14a) consists of plates of lead radiator sandwiched between sheets of scintillating plastic. Bremsstrahlung and pair production in the lead produce an $e^{\pm}$ and γ cascade. The charged particles pass through the scintillator producing light which is transmitted to a phototube by waveshifting plastic. The mean number of charged particles at depth x in the calorimeter (in terms of the radiation length in that material) for an electron initiated electromagnetic cascade is

$$N_{e\pm} = N_0 x^a e^{-bx}$$

where a has a logarithmic dependence on the electron energy and, most importantly, N_0 is proportional to the energy of the incident electron. Typical values for a and b for a lead calorimeter are $a = 3.3$ and $b = 0.46$ for a 40 GeV incident electron. Figure 14b shows a sketch of the development of the cascade. It builds to a peak by 6-7 radiation lengths and then exponentially dies away as electrons and positrons lose energy by

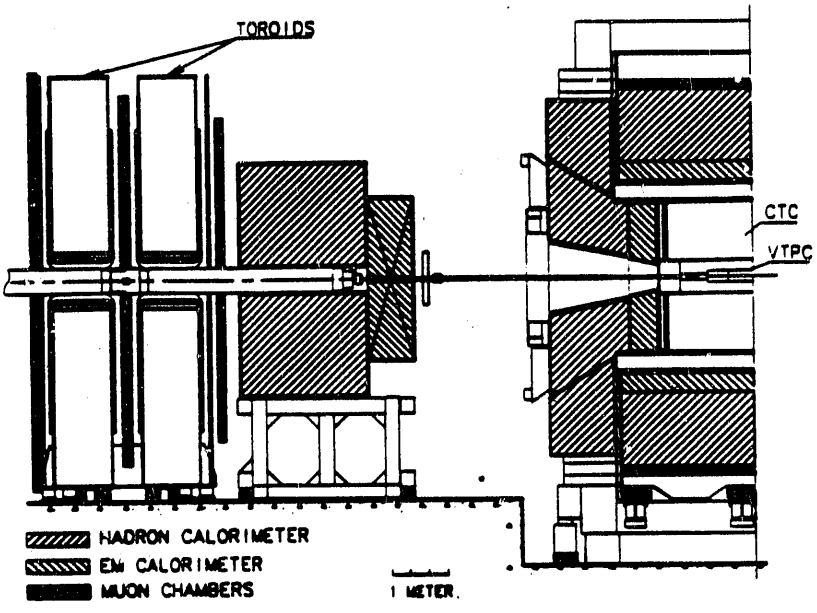

Fig. 12. The CDF detector.

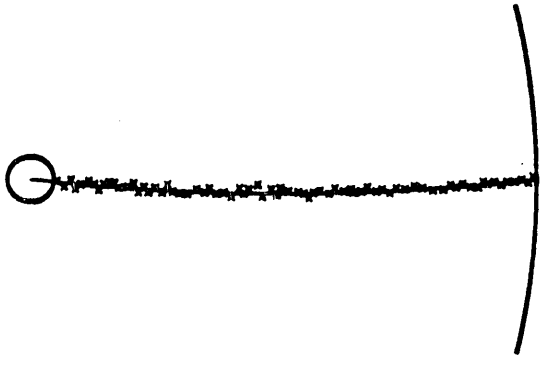

Fig. 13. The trajectory of a charged particle is measured at 84 radial positions.

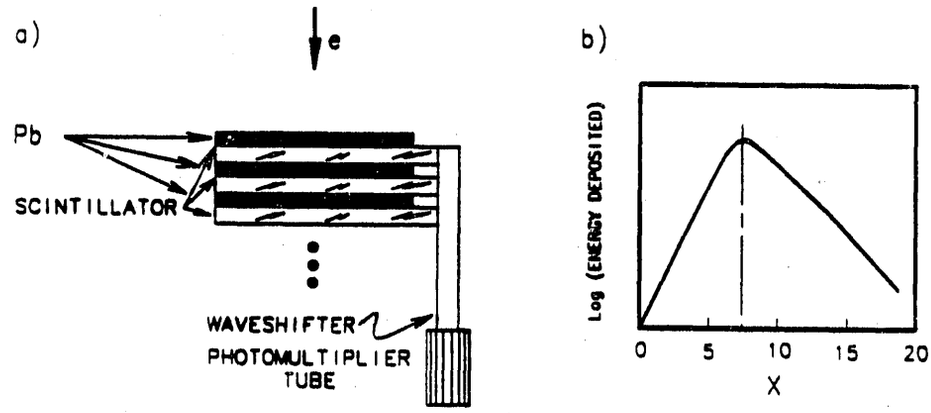

Fig. 14. (a) A sampling electromagnetic calorimeter. (b) Sketch of the longitudinal development of an electromagnetic cascade.

ionization energy loss and no longer are energetic enough to produce the high energy photons that can create additional e^+e^- pairs.

In the CDF electromagnetic calorimeter in the central region, the cascade is sampled at ~ 30 depths. The dominant uncertainty in determining the energy of the incident electron is the statistical uncertainty in the number of cascade electrons passing through the scintillator. Thus

$$\sigma_E \propto \sqrt{N_{e\pm}}$$

Since $N_{e\pm}$ is proportional to the incident electron energy, E, the uncertainty becomes

$$\sigma_E \propto \sqrt{E}$$
$$\frac{\sigma_E}{E} \propto \frac{1}{\sqrt{E}}$$

For the CDF calorimeter,

$$\frac{\sigma_E}{E} = \frac{13.5\%}{\sqrt{E}} \oplus 1.7\%$$

where E is in GeV and the second term is due to cell to cell variations in the energy calibration and is added in quadrature to the first term.

The hadronic calorimeter operates in a similar fashion, but here the incident hadron loses energy by a nuclear cascade. At least 5 nuclear absorption lengths ($\sim$ 1 meter of iron) are needed to contain the shower. Many fewer particles are produced in a nuclear cascade than in an electromagnetic cascade. Consequently the statistical fluctuations are much larger. The CDF calorimeter has an energy resolution for incident pions of

$$\frac{\sigma_E}{E} = \frac{70\%}{\sqrt{E}} \oplus few\,\%$$

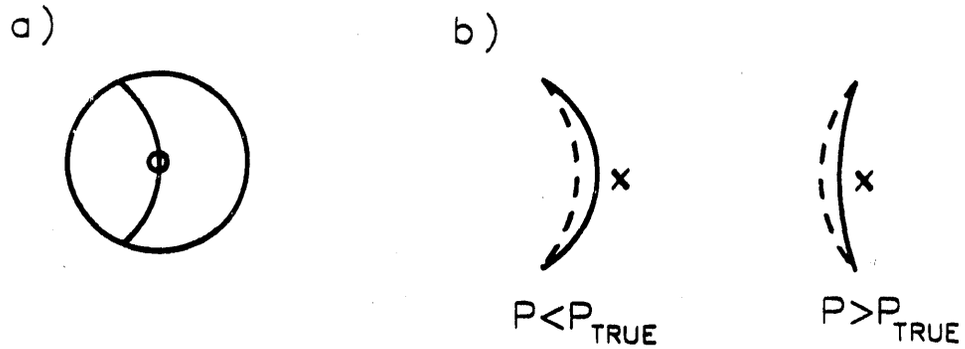

Fig. 15. (a) A cosmic ray muon passing close to the center of the detector. For calibration purposes, it is analyzed as if there were two oppositely charged particles emanating from the detector center. (b)The actual trajectories (dashed curves) of positive and negative tracks of the same momentum but opposite charge. The solid curves show how the tracks would be reconstructed if the central plane of chamber wires were believed to be further to the right.

The ability to make precision energy measurements depends critically on the calibration of the detector elements and the associated systematic uncertainties. At CDF the initial calibration of the calorimeters was done in a test beam with electrons, pions, and muons of known momenta. The initial calibration of the tracking chamber was carried out using cosmic rays (Fig 15a). A cosmic ray that passes close to the center of the detector can be analyzed as if it were two tracks of opposite charge emanating from the detector center. By minimizing the difference in curvature, the difference in initial azimuthal angle, and the distance of closest approach of these "tracks" for a large sample of cosmic rays, slight corrections to the locations of the wires in the chamber can be deduced.

Although these initial calibrations are quite important, the final calibration is done with Collider data since the hostile environment of a high luminosity hadron collider can cause slight alterations in the detector calibration. CDF uses the tracking chamber to check the calorimeter calibration, and the calorimeter to check the tracking chamber. This is not the circular argument it seems because the tracking chamber (calorimeter) response is antisymmetric (symmetric) with respect to the electric charge of an $e^{\pm}$. Figure 15b shows that if the assumed location of the chamber wires is incorrect, the reconstructed curvature of a positive (negative) track will be larger (smaller) than the true curvature. That is,

$$\frac{1}{P^{\pm}} = \frac{1}{P_0} \pm \frac{1}{P_{false}}$$

where $P^{\pm}$ is the reconstructed momentum for a positron or electron, P_0 is the actual momentum, and $\frac{1}{P_{false}}$ is the false curvature caused by the error in the position of the chamber wires. The electromagnetic calorimeter, on the other hand, responds the same to electrons and positrons. If there is a calibration error (ϵ), then the reconstructed and actual energies of the electron and positron are related by

$$E^{\pm} = E_0 \times (1 + \epsilon)$$

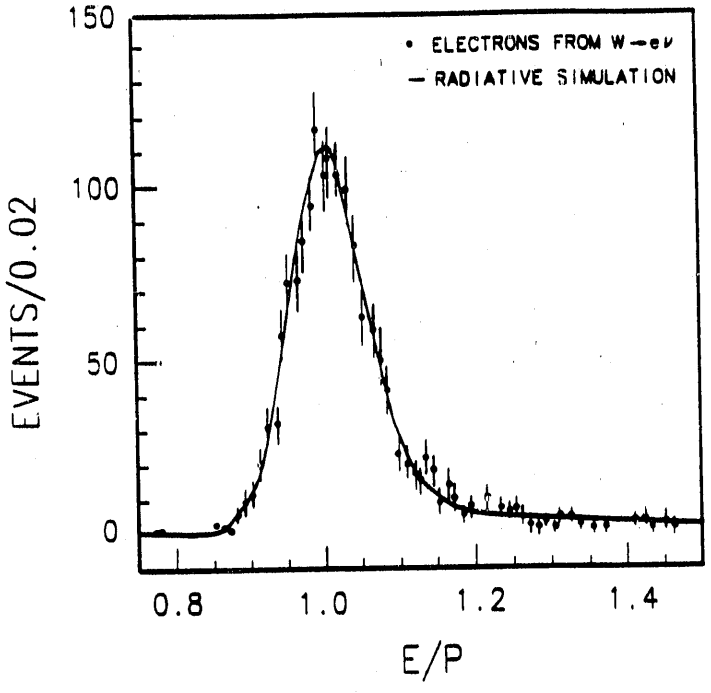

Fig. 16. The E/P distribution for electrons and positrons from W decay. The curve is the result of a detector simulation that includes radiation from the electrons.

The calorimeter calibration error and the tracking chamber false curvature can be determined using a sample of high energy electrons and positrons, where $E = P$. From the above two equations, we get

$$1 + \epsilon = \frac{\left[\left(\frac{E}{P}\right)^{+} + \left(\frac{E}{P}\right)^{-}\right]}{2}$$

$$\frac{1}{P_{false}} = \frac{\left[\left(\frac{E}{P}\right)^{+} - \left(\frac{E}{P}\right)^{-}\right]}{2E}$$

Figure 16 shows E/P for a samples of electrons and positrons from W decay along with the result of a detector simulation. The tail on the high side is due to bremsstrahlung; the calorimeter detects the electron and colinear photons, while the tracking chamber measures the momentum only of the charged electron.

This *in situ* technique was successfully used to achieve the tracking resolution of $\sigma_{P_T}/P_T = 0.0011 P_T$. Geometric distortions in the chamber can still be observed, but they correspond to a false radius of curvature of $\approx$ 50 kilometers! Although this method removes relative errors in the calorimeter and tracking chamber calibration, it does not set the absolute momentum scale. This is obtained from the tracking chamber geometry and the measured B field. The scale is checked by comparing the masses of the J/ψ, Υ, and Z^0 resonances measured by CDF (3.097 ± 0.001, 9.469 ± 0.010, and 90.9 ± 0.36

GeV/c^2) to the world averages (3.0969 ± 0.0001, 9.4603 ± 0.0002, and 91.174 ± 0.021 GeV/c^2)[4].

Separation of leptons from the much more copiously produced hadrons is accomplished using information from all of the detector systems. Figure 17a is a schematic view of an electron in the CDF detector. After passing through the central tracking chamber, the electron loses all of its energy in the electromagnetic calorimeter. The distinguishing feature is the small lateral and transverse size of an electromagnetic cascade, which results in all of the energy being deposited in a single electromagnetic calorimeter tower with little or no energy leaking into the hadronic section. In addition, a strip proportional chamber located near shower maximum depth in the electromagnetic calorimeter provides a transverse profile of the shower. For each electron candidate, a fit of the transverse profile is made to the shape measured in an electron test beam. The χ^2 of the fit is used to distinguish electrons from hadrons. The extrapolated trajectory measured in the tracking chamber must also pass through the center of the shower profile, and the electron's energy measured in the calorimeter must agree with the momentum as measured in the tracking chamber. Finally for some analyses, such as in W and Z decay, the electron is required to be isolated, with little energy in any of the nearby calorimeter cells. This greatly suppresses the background from hadrons, which are usually part of jets and thus are not isolated.

A detected muon is sketched in Figure 17b. The muon passes through the lead and steel of the calorimeters with an energy deposition consistent with a minimum ionizing particle ($\approx$ 0.5 GeV equivalent in the electromagnetic compartment and $\approx$ 2.0 GeV equivalent in the hadronic section). The muon then passes through the muon drift chambers, where the resulting track stub must be consistent with the extrapolated central tracking chamber track within the uncertainty due to multiple Coulomb scattering.

These charged leptons look very different than a hadron jet from the fragmentation of a quark or gluon (Fig. 17c). The large number of hadrons in a jet produces many tracks in the tracking chamber and a large transverse and longitudinal calorimeter energy deposition typical of multiple overlapping hadronic cascades.

The neutrino of course passes through the detector without interacting at all (Fig 17d). As we will see when we get to W decay, the presence of a high energy neutrino is inferred from the lack of momentum balance for the particles detected in a $\bar{p}p$ collision.

There is one technique new to hadron collider detectors that could be quite important in the future – secondary vertex detection. It could have a major impact in top quark physics in separating the W + multijet QCD background from $t\bar{t}$ events which contain two b jets in the final state. The identification of the b jets can also help reduce the combinatoric problem when trying to reconstruct the top decay in order to determine the top mass. Identifying the secondary vertices from b decay will of course also greatly improve prospects for b physics at hadron colliders: b meson and baryon spectroscopy, measuring lifetimes of b states, directly observing the decay distributions from $B\bar{B}$ mixing, and perhaps observing CP violation in B decay.

For the upcoming run, CDF is installing a new vertex detector consisting of four layers of silicon detectors located just outside the beam pipe (Fig. 18). With strip electrodes on a 50μ pitch, the position resolution will be $\approx 15\mu$ (the standard deviation for a square distribution of full width W is $W/\sqrt{12}$). This device will provide an impact parameter resolution for large P_T tracks of $\approx 15\mu$, to be compared with the typical

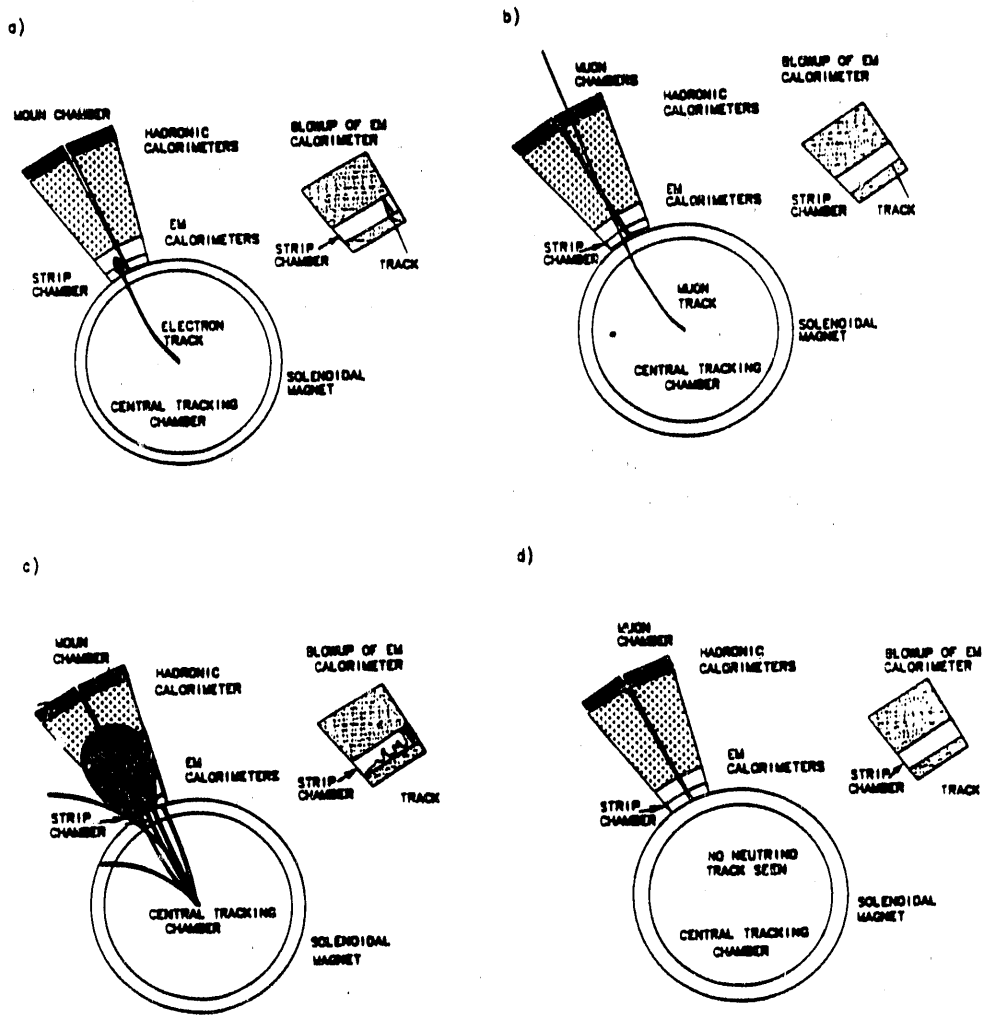

Fig. 17. Schematic drawings of particles in the CDF detector: (a) electron, (b) muon, (c) hadron jet, and (d)neutrino.

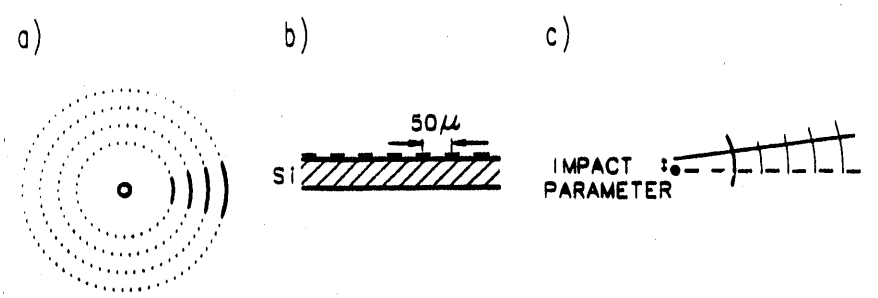

Fig. 18. (a) A sketch of the silicon vertex detector to be installed in the CDF detector. (b) The detector consists of silicon wafers biased to produce a depletion layer with electrodes on a 50μ pitch. (c) The impact parameter for a track relative to the primary interaction vertex.

expected impact parameter for tracks from B decay of 300μ.

2. QCD Studies

2.1. Essential Features of QCD

Before looking at the data, we will briefly review the features of the QCD theory of the strong interaction. QCD is a non-abelian local gauge theory with a three dimensional gauge symmetry (SU(3) of color) in which the generators do not commute. This is to be contrasted to QED, which is based on invariance under a one dimensional local phase rotation (U(1) of electric charge). This difference in the underlying symmetry produces a significant difference in how the carriers of the forces interact. In QED, the photon only interacts with fermion- antifermion pairs because the photon does not carry electric charge. In QCD, on the other hand, the gluons do carry the color charge; the result is 3-gluon and 4-gluon vertices, as well as gluon-fermion-antifermion vertices.

There is by now a great deal of experimental evidence for the color degree of freedom with three colors.

– It is required if the usual spin statistics relation is to be maintained for baryons. In particular, the Δ^{++} contains three u quarks with no orbital angular momentum in a symmetric S = 3/2 spin state. An additional degree of freedom is needed in order to antisymmetrize the wavefunction for these three identical fermions.

– The ratio $R = \frac{\sigma(e^+e^- \to \text{hadrons})}{\sigma(e^+e^- \to \mu^+\mu^-)}$ depends on the sum of the squares of the electric charges for all types of quarks, because the hadrons are produced when an intermediate state virtual photon produces a quark-antiquark pair. The experimental data require that there be three distinct types of quark for each flavor. This is satisfied by having three colors.

– The experimental cross section for producing lepton pairs in hadron collisions is consistent with the prediction of quark-antiquark annihilation when a factor of 1/3 is included in the cross section formula. This is expected with color SU(3), since a quark can only annihilate an antiquark to produce a photon if the antiquark has the same color as the quark. Since there are three colors, the probability that the quark strikes

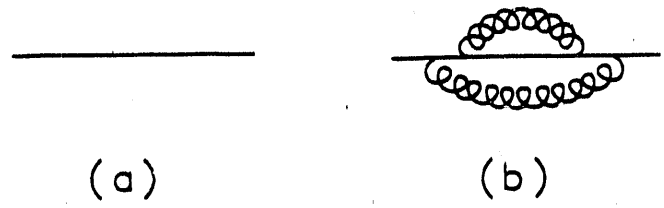

Fig. 19. (a) A quark viewed with a moderate q^2 probe. (b) A high q^2 probe might catch the quark in a quantum fluctuation.

an antiquark of the same color is 1/3.
– The relative branching ratios of the tau lepton into leptons or hadrons agree with expectations if each quark flavor comes in three colors.
– The measured π^0 lifetime agrees with the calculation of $\pi^0 \rightarrow$ quark loop $\rightarrow \gamma\gamma$ if there are three quark colors.
– Anomaly cancellation in electroweak interactions is needed for divergence free calculations. The cancellation occurs if, for each generation,

$$\sum_{quarks} Q_i + \sum_{leptons} Q_i = 0$$

This is satisfied if there are three quark colors.

There are a number of important general consequences of the QCD theory of the strong interaction. First there is the evolution of the structure functions. In the naive parton model, the structure functions, F(x), depend only on the Feynman x of the parton and not on the q^2 of the interaction. In QCD, however, there is a q^2 variation. As the q^2 of a probe increases, the spatial region or time interval probed decreases. This raises the probability of finding a quantum fluctuation. For example, if a moderate q^2 probe observes a quark, a high q^2 probe might see a quark plus two gluons that were virtually emitted (Fig. 19). Consequently at large q^2 there is a smaller probability of finding a large $x = \frac{P_{parton}}{P_{proton}}$ quark or gluon and a larger probability of finding a small x quark or gluon. Figure 20 shows the measured q^2 variation of the structure function [5].

The evolution can be calculated quantitatively by considering radiation graphs like those in Figure 21. The internal consistency of these graphs plus the constraints of conservation of momentum and fermion number lead to the Altarelli-Parisi evolution equations [6]. For example, the variation of the quark distribution function with q^2 is given by

$$\frac{d\,F(x)}{d\,ln(q^2)} = \frac{\alpha_s(q^2)}{2\pi}\left[\int_x^1 \frac{dy}{y}F(y)P^{qq}(\frac{x}{y}) + 2N_F\int_x^1 \frac{dy}{y}G(y)P^{qg}(\frac{x}{y})\right]$$

where the factor in front of the bracket is the vertex factor, N_F is the number of quark flavors that can be produced, and the two integrals correspond to the quark production in Figures 21a and 21c respectively. The functions F and G are the quark and gluon distribution functions. The splitting functions P are calculated for each radiation graph. For example the splitting function for getting a quark from a gluon

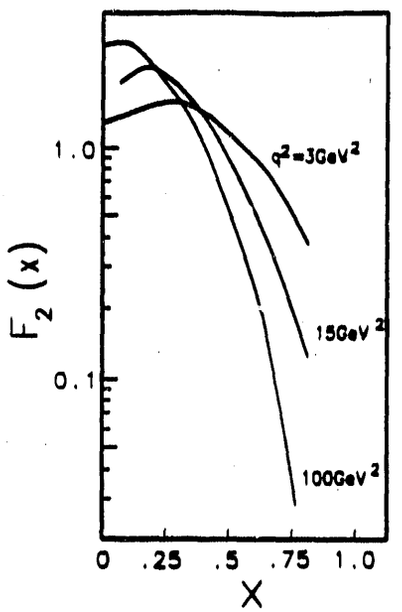

Fig. 20. The proton structure function $F_2(x)$ for three values of q^2.

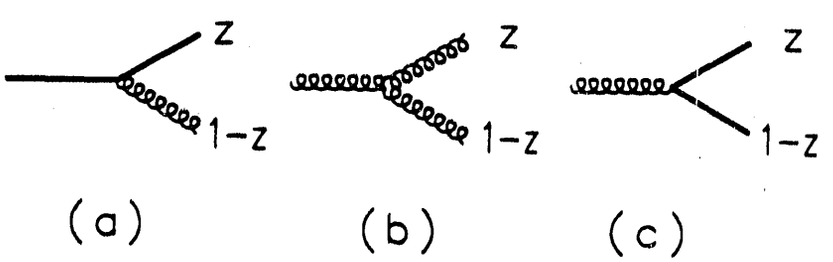

Fig. 21. Radiation graphs for calculating structure function evolution.

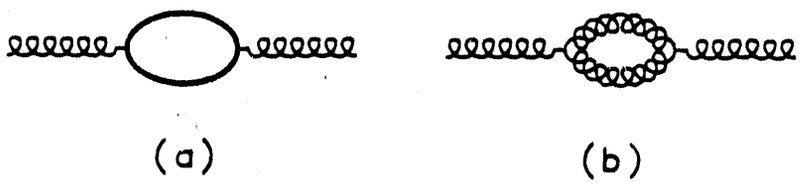

Fig. 22. Gluon propagator corrections that produce (a) screening and (b) anti-screening.

(Fig. 21c) is

$$P^{qg}(x) = \frac{1}{2}(x^2 + (1-x)^2)$$

while that for getting a gluon from a quark (Fig 21a) has the usual bremsstrahlung $\frac{1}{x}$ behavior

$$P^{gq}(x) = \frac{4}{3}\left(\frac{1+(1-x)^2}{x}\right)$$

Another important feature of QCD is the running of the coupling constant. In QED, vacuum polarization screens a particle's bare charge. Consequently the force on a test charge grows faster than $\frac{1}{r^2}$ when probing closer to the source charge (i.e. with a larger q^2 probe). This means that $\alpha_{em}(q^2)$ increases with increasing q^2. As we shall see later, this has been measured, with $\alpha_{em}(q^2)$ increasing from 1/137 at low q^2 to 1/128 at $q^2 = M_Z^2$.

QCD provides mechanisms for both screening and anti-screening (Fig 22). The former is produced by the fermion loop correction to the gluon propagator, in complete analogy with the QED case. Anti-screening is produced by gluon loop corrections to the gluon propagator. Whether screening or anti-screening dominates is determined by the number of types of gluons (colors) and quarks (flavors) that can be excited at a given q^2. For an SU(N) theory

$$\frac{1}{\alpha_s(q^2)} = \frac{1}{\alpha_s(\mu_0^2)} + \frac{11N_C - 2N_F}{12\pi} ln\left(\frac{-q^2}{\mu_0^2}\right)$$

where μ_0 is the renormalization point. For SU(3), another common notation is to collect the constants in the two terms above and write

$$\frac{1}{\alpha_s(q^2)} = \frac{33 - 2N_F}{12\pi} ln\left(\frac{-q^2}{\Lambda^2}\right)$$

where Λ is the QCD scale parameter. Note that $33-2N_F$ is positive for N_F=3,4,5, and 6. Thus anti-screening dominates, and $\alpha_s(q^2)$ decreases with increasing q^2. At small q^2 this means large α_s and quark confinement, while at large q^2 it means asymptotic freedom and the utility of using a perturbation expansion.

2.2. QCD in $\bar{p}p$ Collisions

The proton and antiproton each contains quarks, antiquarks, and gluons. A QCD scattering thus occurs as in Figure 23. The observed differential cross section can be

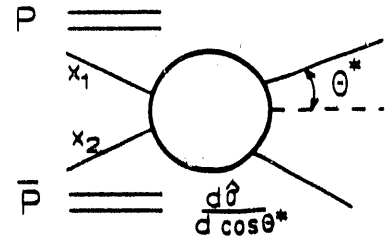

Fig. 23. A hard scattering between two partons in a $\bar{p}p$ collision.

written as

$$\frac{d\sigma}{dx_1\,dx_2\,dcos\theta^*} = \sum_{i,j}\left[f_i^p(x_1,q^2)f_j^{\bar{p}}(x_2,q^2) + f_j^p(x_1,q^2)f_i^{\bar{p}}(x_2,q^2)\right]\frac{d\hat{\sigma}_{ij}}{dcos\theta^*}$$

where $f_i^p(x_1,q^2)$ is the number density (not momentum density) in a proton of partons of type i carrying momentum fraction x_1, and $\frac{d\hat{\sigma}_{ij}}{dcos\theta^*}$ is the differential cross section for partons of types i and j to scatter at an angle θ^* in the parton-parton center of mass frame.

An obvious leading order diagram is the strong interaction analog of e^+e^- scattering (Fig. 24a). However since the gluon carries color charge and therefore interacts with other gluons, there are other lowest order t-channel diagrams (Fig. 24b,c) as well as s-channel diagrams (Fig. 24d,e). The s-channel diagrams tend to give small contributions because the hard scattering cross section has a factor

$$\frac{d\hat{\sigma}}{dq^2} \propto \frac{1}{q^4}$$

(as in Rutherford scattering) where q is the 4-momentum carried by the propagator, and q^2 is typically much larger in s-channel diagrams than in t-channel diagrams.

The three t-channel diagrams have different weights due to the number of colors of gluons that can be exchanged and the number of colors of quarks that can be produced. A quark-quark-gluon vertex has a vertex factor $\frac{4}{3}\alpha_s$, while a three gluon vertex has strength $3\alpha_s$. The other difference among these diagrams is the angular distribution. The hard scattering cross section can be written as

$$\frac{d\hat{\sigma}}{dcos\theta^*} = \frac{\pi\alpha_s^2}{\hat{s}}\frac{f(\theta^*)}{(1-cos\theta^*)^2}$$

where $f(\theta^*)$ depends on the graph. For example, it is $\frac{9}{16}(3+cos^2\theta^*)^3$ for the $g\,g \rightarrow g\,g$ diagram. As we will see in a moment, the angular distribution is dominated by the Rutherford pole in the denominator, and thus the cross sections for the gg, gq, and qq initial states all have a similar angular dependence. The consequence of this is that the full $\bar{p}p$ cross section can be written as

$$\frac{d\sigma}{dx_1\,dx_2\,dcos\theta^*} \simeq \frac{F(x_1)}{x_1}\frac{F(x_2)}{x_2}\frac{d\hat{\sigma}}{dcos\theta^*} \tag{1}$$

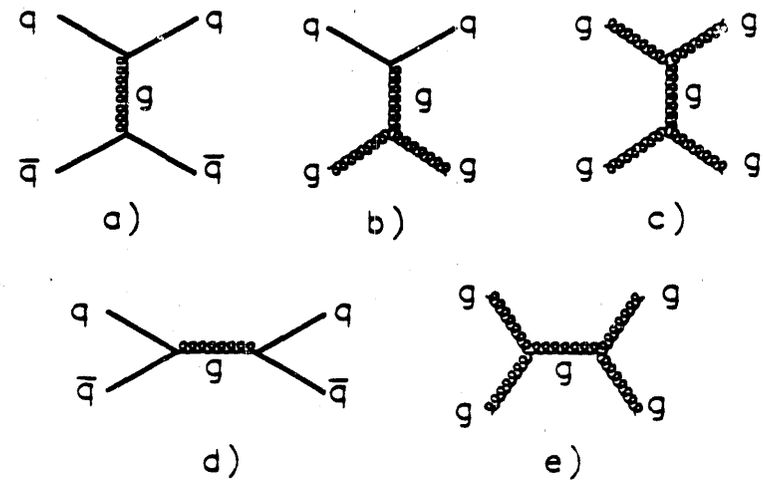

Fig. 24. Leading order diagrams for parton-parton scattering.

where

$$F(x) = G(x) + \frac{4}{9}\left[Q(x) + \overline{Q}(x)\right]$$

Here G, Q, and $\overline{Q}$ are the total gluon, quark, and antiquark momentum densities, and the $\frac{4}{9}$ is a consequence of the $gq\overline{q}$ and ggg vertex factors. Note that C invariance requires that $F^p(x) = F^{\overline{p}}(x)$.

If this picture of parton elastic scattering is correct, then large q^2 events should predominantly contain two large P_T jets, the fragmentation products of the scattered partons in Fig. 23. The experimental jet finding algorithm is important, since the jet energy and size as well as the number of jets in an event depend on the algorithm. CDF [7] begins with a cluster seed, which is a calorimeter tower with E_T above a seed tower threshold. ($E_T \equiv E sin\theta$ is essentially the same as $P_T = P sin\theta$ except that the measurement comes from the calorimeter rather than the tracking chamber.) A cone of half angle R in $\eta - \phi$ space (typically 0.7) is drawn around the seed tower. The E_T weighted centroid of the towers within the cone becomes the new cluster centroid. A new cone is drawn, and the process is iterated until the cluster is identical after two successive iterations.

Hadron jets are easily seen in high energy $\overline{p}p$ collisions (Fig. 25). To see if jets dominate, let us consider the observables H_n [8].

$$H_1 \equiv \frac{E_T(\text{largest } E_T \text{ jet})}{\sum E_T}$$

$$H_2 \equiv \frac{E_T(\text{largest } E_T \text{ jet}) + E_T(\text{second largest } E_T \text{ jet})}{\sum E_T}$$

$$\vdots$$

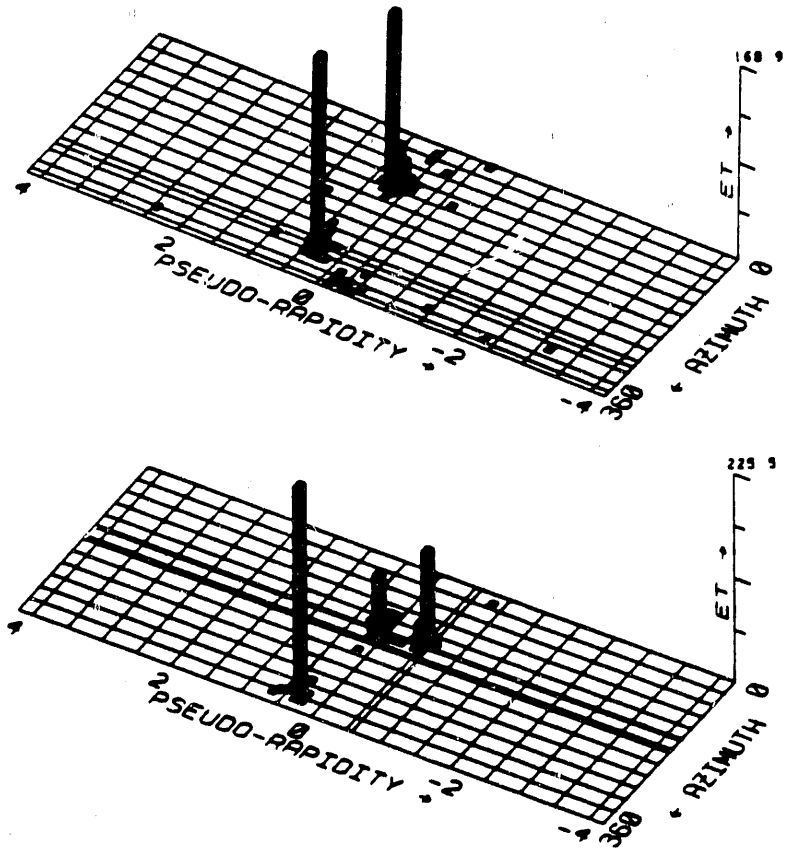

Fig. 25. (a) A dijet event in the CDF detector. The E_T is shown for each electromagnetic (solid) and hadronic (hatched) calorimeter tower (b) A three jet event.

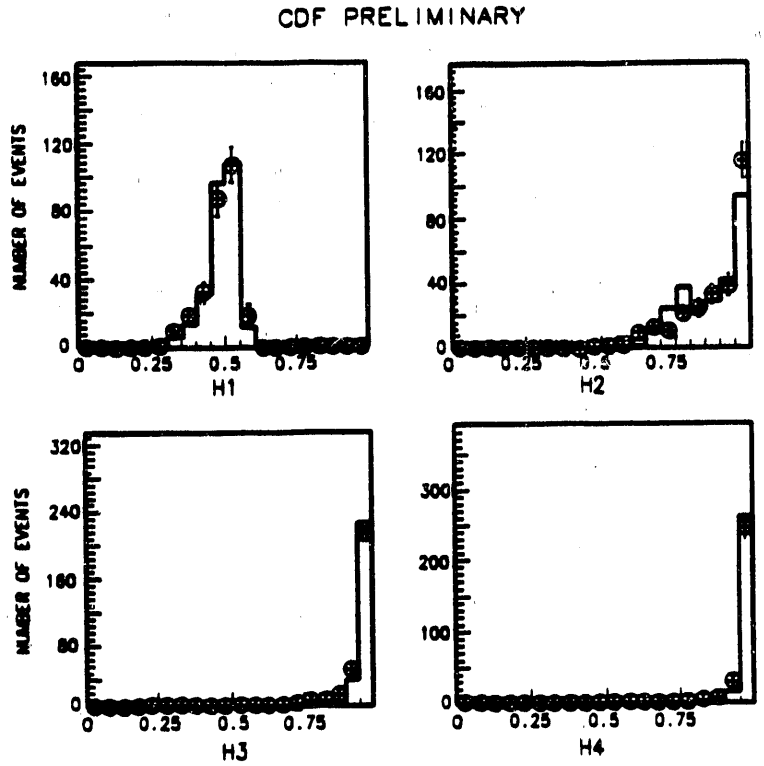

Fig. 26. The jet E_T fractions for large $\sum E_T$ CDF events. The solid lines come from the Herwig parton shower Monte Carlo.

where

$$\sum E_T = \sum |E sin\theta|$$

Distributions for the first four H_n variables from CDF events with $\sum E_T > 400\ GeV$ [9] are compared with theory [10] in Figure 26. H_1 peaks at 0.5; H_2 peaks at 1.0 with a tail; and H_3 peaks sharply at 1.0. This is consistent with the leading order QCD diagrams plus the next to leading order correction in which a hard gluon is radiated from one of the scattered partons (Fig. 25b).

2.3. Dijet Production

The CDF inclusive jet cross section [11] is shown in Figure 27. The theoretical calculation uses quark and gluon distribution functions measured in other processes like deep inelastic scattering, with α_s and structure functions evolved to $q^2 = P_T^2$. The agreement between data and theory over 7 decades is excellent. UA1 used equation 1 and theoretical calculations of the hard scattering cross section to extract the effective structure function, F(x), from their data (Fig 28) [14]. If it is assumed that the jets are produced only from the scattering of quarks, then the prediction is much too small at low x; thus gluon scattering is required. From this comparison, it is also clear that

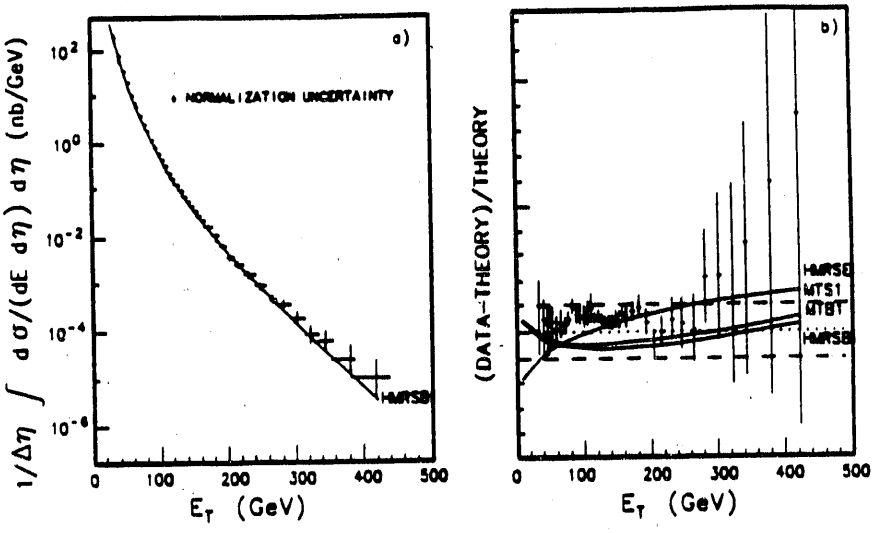

Fig. 27. (a) The CDF inclusive jet cross section compared to a theoretical calculation [12] using the HMRSB structure functions [13]. (b) The difference between the data and theory shown on a linear scale. The variation in the theoretical prediction when the structure functions are changed is also shown.

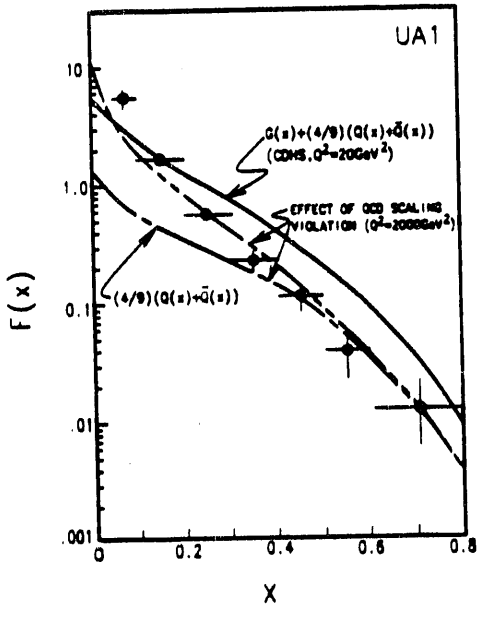

Fig. 28. The effective structure function, F(x), as measured by UA1. The data are compared with a number of theoretical calculations.

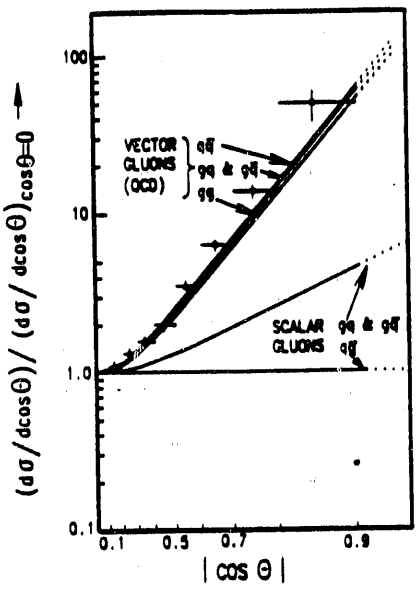

Fig. 29. The UA1 jet angular distribution compared to theoretical predictions.

quarks dominate at large x while gluons dominate at small x, as expected given the bremsstrahlung origin of gluons. Also if the theoretical prediction uses the structure functions as measured at low q^2 without evolving them to $q^2 = P_T^2$, then the result is much larger than the data at high x.

We can also look at the jet angular distribution. UA1 data [15] are shown in Figure 29. Note that the predictions for $q\bar{q}$, gq, and gg scattering are very similar; they are dominated by the Rutherford pole. The result would be quite different, however, for an abelian scalar gluon theory, where the propagator would have spin 0 or 1/2 but not 1. The large cross section variation due to the Rutherford pole makes it difficult to discern how well the data and theory agree. This effect can be removed if another angular variable is used.

$$\chi \equiv \frac{1 + cos\theta^*}{1 - cos\theta^*}$$

$$d\chi = \frac{2}{(1 - cos\theta^*)^2} dcos\theta^*$$

$$\frac{d\sigma}{d\chi} = \frac{(1 - cos\theta^*)^2}{2} \frac{d\sigma}{dcos\theta^*}$$

The CDF angular distribution is shown in Figure 30 [59]. There is good agreement with the QCD prediction.

2.4. Multjet Production

Beyond leading order in the perturbation expansion, additional diagrams appear. There are diagrams, like vertex corrections, with additional internal lines (Fig. 31a,b,c) as

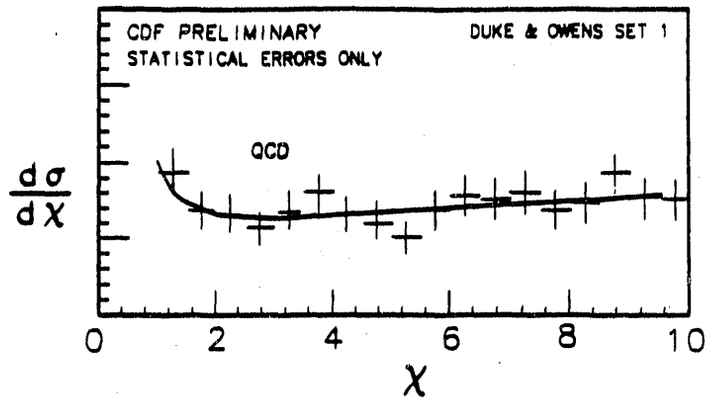

Fig. 30. CDF data on the jet angular distribution compared with a QCD calculation. The data contain dijet events with $M_{jj} > 200\ GeV/c^2$.

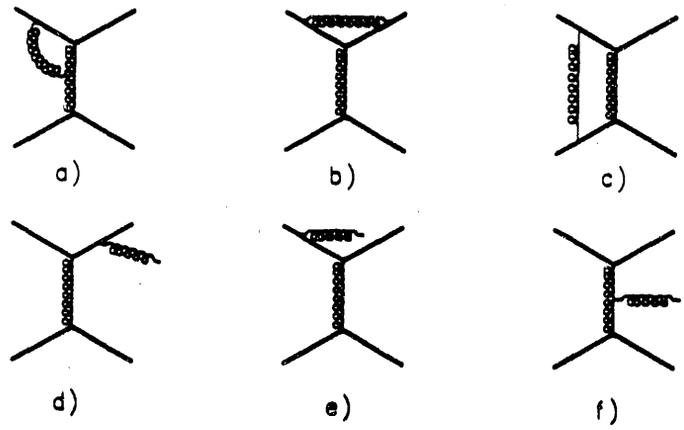

Fig. 31. Higher order corrections to the leading order parton-parton scattering.

well as diagrams with additional external lines like gluon bremsstrahlung (Fig. 31d,e,f). The latter diagrams should produce 3-jet final states, have a cross section down by a factor of $\sim \alpha_s$ relative to the 2-jet cross section, and have a bremsstrahlung like third jet energy distribution (recall the Altarelli-Parisi splitting function $P^{gq}(x) \sim \frac{1}{x}$). Figure 32 shows the ratio of 3-jet to 2-jet event rates for UA1 data [17]. As expected, the ratio is $\simeq \alpha_s$, and although statistics are limited, the data is consistent with a running $\alpha_s(q^2)$. The data have been corrected both for the loss of 3-jet events due to the spatial overlap of jets and for events in which the third detected jet was due to a fluctuation in the parton fragmentation or in the underlying event. Both UA1 [17] and UA2 [18] have used the 3-jet to 2-jet ratio to deduce α_s.

$$\frac{K_3}{K_2}\alpha_s = 0.22 \pm 0.02 \pm 0.03 \qquad (UA1)$$

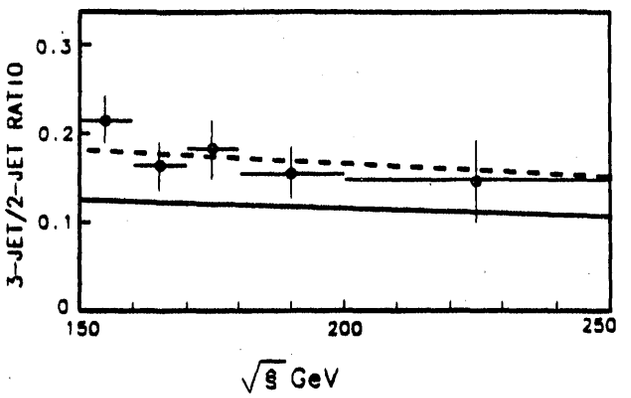

Fig. 32. The UA1 ratio of the 3-jet to 2-jet cross sections as a function of the multi-jet center of mass energy. The lines correspond to different choices of the 3-jet q^2 scale.

$$= 0.23 \pm 0.01 \pm 0.04 \qquad (UA2)$$

where K_3 and K_2 are the corrections ("K factor") for the uncalculated higher order diagrams.

To look for the expected bremsstrahlung like distribution, one can study the energy sharing among the three final state jets. By convention, the parton numbering scheme has the initial state parton that is more (less) energetic in the $\bar{p}p$ rest frame denoted 1 (2). In the center of mass frame of partons 1 and 2, the three outgoing partons are labeled 3, 4, and 5, where 3 is the most energetic and 5 is the least energetic. Figure 33 shows the jet energy fractions X_3 and X_4, where $X_i \equiv \frac{2E_i}{E_3+E_4+E_5}$ in the center of mass frame of partons 1 and 2. The leading jet (parton 3) carries more energy than 3-body phase space would predict, as expected in QCD since this jet did not radiate a gluon. The same is true for the next to leading jet, since although it did radiate a gluon, that gluon is typically very soft. Since $X_3 + X_4 + X_5 = 2$ and jets 3 and 4 have more energy than predicted by phase space, jet 5 has less energy than phase space predicts, as expected for a bremsstrahlung product.

The variables θ^* and ψ^* used to describe the 3-jet angular distributions are defined in Figure 34. As expected, the $cos\theta^*$ distribution peaks at 1.0 (Fig. 35a), because, as in the 2-jet case, t-channel gluon exchange dominates. The ψ^* distribution (Fig. 35b) peaks toward 0° and 180° because in that region jet 5 can be close in angle not only to jet 4 but also to jet 1 or 2. Thus there are large contributions here from the initial state gluon bremsstrahlung diagrams.

Beyond leading order in QCD, the inclusive jet differential cross section depends on the cone size used in finding the jet clusters. For leading order diagrams, as long as the cone is large enough to contain the parton's hadronic fragments, the E_T in the cone will not change. Thus the value of the abscissa in Fig. 27 where an event is plotted does not change. For higher order diagrams that contain hard gluon bremsstrahlung, as the clustering cone gets larger more of the bremsstrahlung products are included in the cone. Thus the E_T of the jet increases, and the event is plotted at a larger value of the abscissa. This has the effect of increasing the differential cross section, $\frac{d\sigma}{dE_T}$. Figure 36

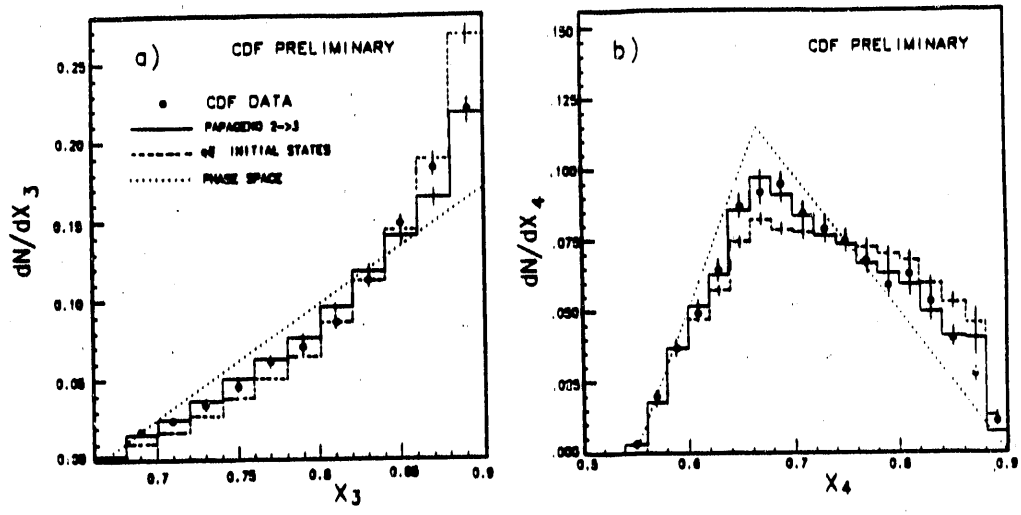

Fig. 33. The jet energy fraction for the leading and next to leading jets in three jet events. The CDF data [19] are compared to a next to leading order QCD calculation[20], the same calculation without gluons as initial state partons, and 3-body phase space.

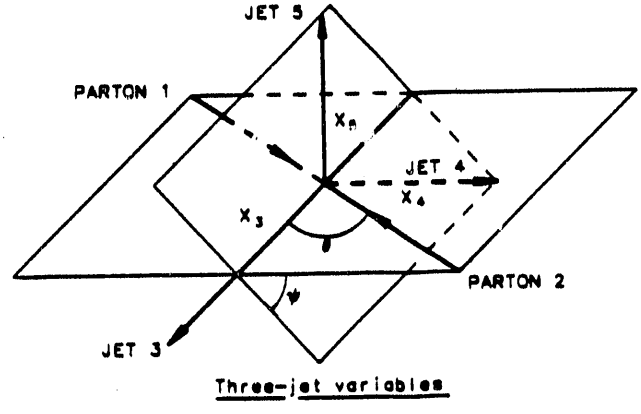

Fig. 34. The angular variables used to describe 3-jet events.

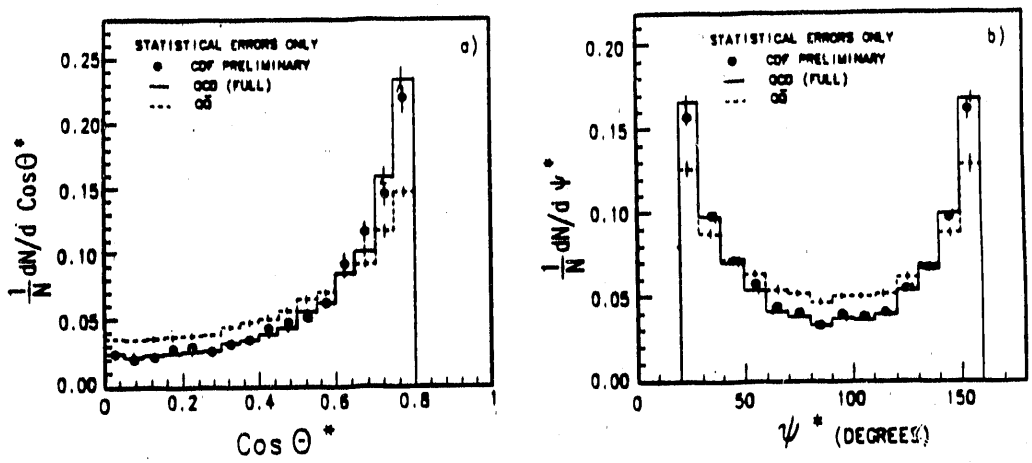

Fig. 35. The (a) $cos\theta^*$ and (b) ψ^* distributions from CDF 3-jet data [21] compared with QCD calculations with and without hard scattering of initial state gluons. The cuts in $cos\theta^*$ and ψ^* are made to ensure that the jets are well separated from each other and from the beam.

shows this for CDF data [22] and a next to leading order calculation[23]. The data and calculation have the same trend, but the data increases somewhat more rapidly as the cone size increases. It is expected that the predicted slope would be larger if more gluons were allowed to radiate (QCD diagrams beyond next to leading order).

2.5. Large P_T γ, W, and Z Production

The strong interaction can also be studied with a large P_T γ, W, or Z in the final state (Fig. 37a). The utility of these processes for studying QCD comes from both an experimental and a theoretical simplification. The experimental advantage is that the γ, e, and μ detection efficiency and resolution are straightforward to evaluate. This contrasts with quarks and gluons for which multihadron fragmentation and its effect on detector resolution as well as the dependence on clustering size due to gluon bremsstrahlung result in serious systematic difficulties. From a theoretical point of view, vector boson production has simpler higher order corrections; the next to leading order diagrams are of order α_s^2, to be compared with jet production where the corrections are of order α_s^3. This means fewer diagrams and interference terms to calculate.

In the case of photon production, there is an experimental complication that arises from the bremsstrahlung diagram (Fig. 37b) in which the photon is not produced at a hard scattering vertex, but is radiated from one of the scattered partons. The difficulty is that photon identification usually requires isolation (no energetic hadrons nearby), and thus the size of the bremsstrahlung diagram contribution depends on the details of the γ isolation requirement. However, by imposing a rather strict isolation requirement, the effect of the bremsstrahlung diagrams can be minimized.

Figure 38 shows the UA1 [24] and UA2 [25] photon production cross section. Note the similarity of the cross section shape to that for jet production. This reflects the common proton structure functions as well as the dominance of the similar $2 \rightarrow 2$ hard

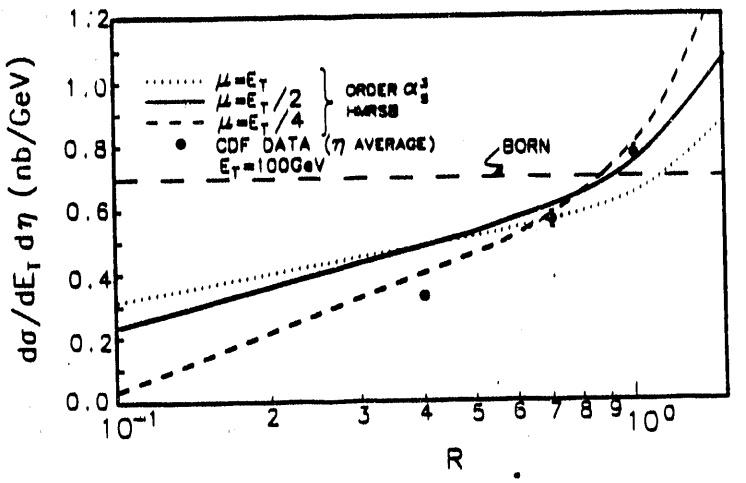

Fig. 36. The dependence of the inclusive cross section on the radius of the clustering cone. The next to leading order calculations have been made for a number of choices of the renormalization scale.

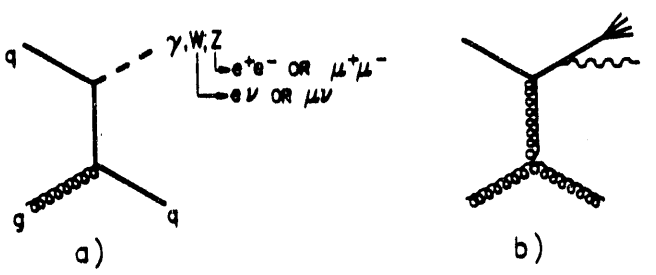

Fig. 37. (a) Leading order diagram for large P_T vector boson production. (b) The photon bremsstrahlung diagram.

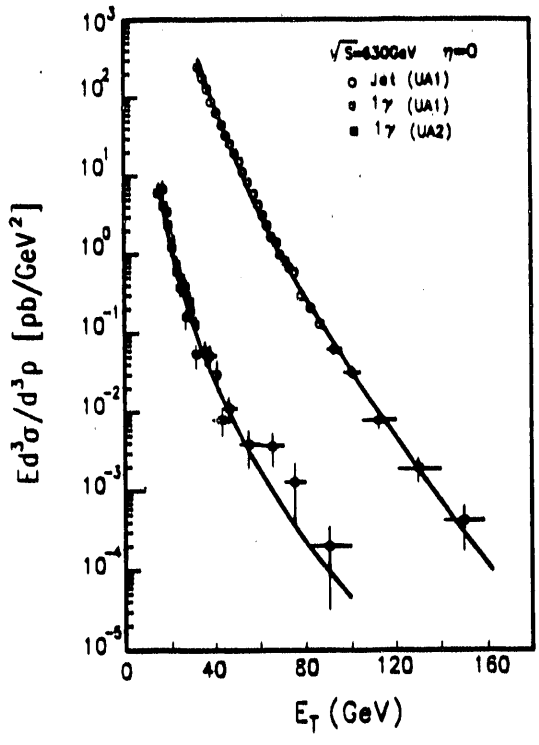

Fig. 38. Photon and jet production cross sections from UA1 and UA2 compared with theoretical predictions.

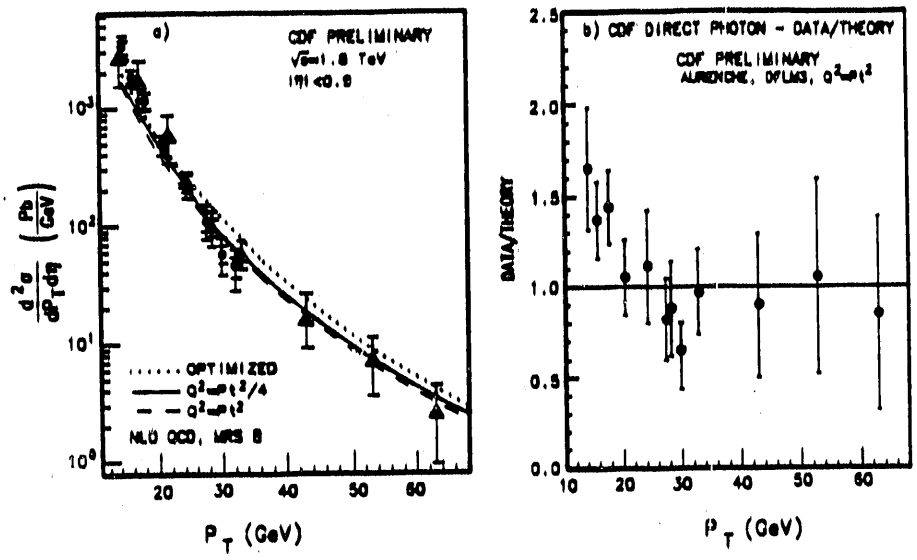

Fig. 39. (a) CDF photon production cross section compared to theoretical predictions. (b) Data divided by theory on a linear scale.

scattering diagrams. The photon data agree well with the order $\alpha_s^2\alpha_{em}$ calculation [26]. CDF has measured the photon cross section at $\sqrt{s} = 1.8$ TeV [27]. Figure 39 shows good agreement except at the lowest P_T where the bremsstrahlung diagrams make the largest contribution and where the uncertainty in the structure function (gluon $x < 0.02$) is largest. UA1 [28] has observed the difference in the jet and photon angular distributions due to the propagator spin (1 for jets, $\frac{1}{2}$ for photons). Figure 40 shows agreement between data and the predicted behavior. The prediction includes the effect of the $\sim 35\%$ π^0 background in the photon data sample.

UA2 has measured $\alpha_s(M_W^2)$ by comparing the numbers of W + 1 jet and W + 0 jet events [29]. They find

$$\alpha_s(M_W^2) = 0.13 \pm 0.03 \pm 0.03 \pm 0.02$$

where the first uncertainty is statistical, the second is due to experimental systematics such as the detector's jet energy scale, the underlying event, and uncertainties in the structure functions, and the third is due to uncertainties in estimating the higher order corrections to the theoretical calculation.

3. Studies of the Electroweak Force

3.1. Overview of the Standard Model

The electroweak interaction is produced by local gauge invariance under the gauge group $SU(2)_L$ of weak isospin $\times$ U(1) of weak hypercharge. The elementary fermions are in left handed weak isodoublets and right handed weak isosinglets.

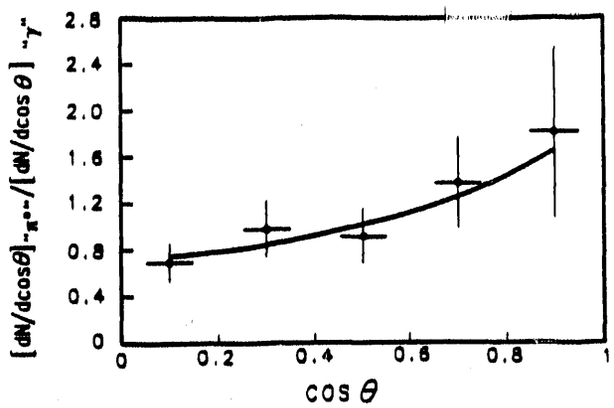

Fig. 40. The ratio of the π^0 to γ angular distributions from UA1 compared with expectations.

$$\begin{pmatrix} \nu_e \\ e^- \end{pmatrix}_L \quad \begin{pmatrix} \nu_\mu \\ \mu^- \end{pmatrix}_L \quad \begin{pmatrix} \nu_\tau \\ \tau^- \end{pmatrix}_L \quad e^-_R \quad \mu^-_R \quad \tau^-_R \quad \nu_{eR} \quad \nu_{\mu R} \quad \nu_{\tau R}$$

$$\begin{pmatrix} u \\ d' \end{pmatrix}_L \quad \begin{pmatrix} c \\ s' \end{pmatrix}_L \quad \begin{pmatrix} t \\ b' \end{pmatrix}_L \quad d'_R \quad s'_R \quad b'_R \quad u_R \quad c_R \quad t_R$$

where the right handed neutrinos are present if the neutrinos have rest mass. The weak eigenstates denoted by primes are related to the strong eigenstates by the CKM matrix

$$\begin{pmatrix} d' \\ s' \\ b' \end{pmatrix} = V \begin{pmatrix} d \\ s \\ b \end{pmatrix}$$

$$V = \begin{pmatrix} V_{ud} & V_{us} & V_{ub} \\ V_{cd} & V_{cs} & V_{cb} \\ V_{td} & V_{ts} & V_{tb} \end{pmatrix}$$

The generators or gauge bosons are

$$\begin{array}{lll} W^1_\mu & W^2_\mu & W^3_\mu \qquad SU(2) \\ B_\mu & & \qquad\quad U(1) \end{array}$$

The interaction Lagrangian, as in electromagnetism ($\mathcal{L}_{int} = eA_\mu \cdot J^\mu$), has the gauge fields coupled to the fermion currents,

$$\mathcal{L}_{int} = g_2 \boldsymbol{J}_\mu \cdot \boldsymbol{W}_\mu + g_1 J^Y_\mu B_\mu$$

where $\boldsymbol{J}_\mu$ is the fermion weak isospin current, and J^Y_μ is the fermion weak hypercharge current. With the usual definitions of raising and lowering operators

$$x^\pm \propto x^1 \pm ix^2$$

this becomes

$$\mathcal{L}_{int} = \frac{g_2}{\sqrt{2}} \left[J^-_\mu W^+_\mu + J^+_\mu W^-_\mu \right] + g_2 J^3_\mu W^3_\mu + g_1 J^Y_\mu B_\mu$$

where the first term is the charged current and the rest is the neutral current. The connection between electric charge, weak isospin, and hypercharge

$$Q = I_3 + Y$$

or its current equivalent

$$J_\mu^{EM} = J_\mu^3 + J_\mu^Y$$

and our knowledge of the electromagnetic term in the interaction Lagrangian

$$eJ_\mu^{EM} A_\mu = e(J_\mu^3 + J_\mu^Y)A_\mu$$

allows us to find the linear combinations of W_μ^3 and B_μ that correspond to the photon (A_μ) and the Z^0 (Z_μ)

$$W_\mu^3 = \frac{g_2 Z_\mu + g_1 A_\mu}{\sqrt{g_2^2+g_1^2}} \qquad B_\mu = \frac{-g_1 Z_\mu + g_2 A_\mu}{\sqrt{g_2^2+g_1^2}}$$

This gives

$$\begin{aligned}
\mathcal{L}_{int} &= \frac{g_2}{\sqrt{2}}\left[J_\mu^- W_\mu^+ + J_\mu^+ W_\mu^-\right] + \left[\sqrt{g_2^2+g_1^2}\, J_\mu^3 - \frac{g_1^2}{\sqrt{g_2^2+g_1^2}} J_\mu^{EM}\right] Z_\mu \\
&\quad + \frac{g_2 g_1}{\sqrt{g_2^2+g_1^2}} J_\mu^{EM} A_\mu \\
&= \frac{g_2}{\sqrt{2}}\left[J_\mu^- W_\mu^+ + J_\mu^+ W_\mu^-\right] + \frac{g_2}{cos\theta_W}\left[J_\mu^3 - sin^2\theta_W\, J_\mu^{EM}\right] Z_\mu \\
&\quad + g_2\, sin\theta_W\, J_\mu^{EM} A_\mu
\end{aligned}$$

where instead of g_2 and g_1, we choose to use g_2 and θ_W. The weak angle, θ_W, is defined through $tan\theta_W = \frac{g_1}{g_2}$.

We can relate g_2 and θ_W to the physical constants e and G_F which have been measured accurately.

$$\begin{aligned}
g_2 sin\theta_W &= e \\
\frac{g_2^2}{8M_W^2} &= \frac{G_F}{\sqrt{2}}
\end{aligned}$$

The latter comes from the requirement that $\mathcal{L}^\dagger\mathcal{L}$ at $q^2 \simeq 0$ reduce to the Fermi four-fermion interaction. These equations can be rewritten to give the mass of the W,

$$M_W^2 = \frac{1}{2}g_2^2 \frac{1}{2\sqrt{2}G_F} = \frac{\pi\alpha_{EM}}{\sqrt{2}G_F sin^2\theta_W}$$

Since the W and Z masses are produced by the Higgs mechanism and the Lagrangian terms in which the W and Z interact with the Higgs have coefficients g_2^2 and $\frac{g_2^2}{cos^2\theta_W}$, the Z mass is given by

$$\begin{aligned}
M_Z^2 &= \frac{M_W^2}{cos^2\theta_W} \\
&= \frac{1}{2}(g_2^2+g_1^2)\frac{1}{2\sqrt{2}G_F} = \frac{\pi\alpha_{EM}}{\sqrt{2}G_F sin^2\theta_W\, cos^2\theta_W}
\end{aligned}$$

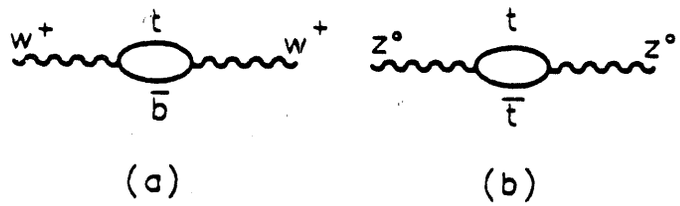

Fig. 41. Heavy quark loop corrections to the (a) W and (b) Z propagators.

So far we have only considered the lowest order electroweak effects. To this order, three experimental inputs are needed to fully specify the electroweak sector, for example α_{EM}, G_F, and M_Z.

The dominant radiative correction results from vacuum polarization loops in the propagators [30]. This produces a running of the coupling constants, $g_2(q^2)$ and $g_1(q^2)$. It also further splits the W and Z masses if there are heavy fermion doublets with large mass splitting, because the loop corrections (Fig. 41) have different kinematic suppression. The W and Z masses can be written as

$$M_W^2 = \frac{1}{2}g_2^2(M_W)v_W^2$$
$$M_Z^2 = \frac{1}{2}(g_1^2(M_Z) + g_2^2(M_Z))v_Z^2$$

where v comes from the Higgs vacuum expectation value. As before,

$$v_W^3 = \frac{1}{2\sqrt{2}G_F}$$

since in beta decay G_F is the square of the coupling constant divided by the propagator

$$G_F \propto \frac{g_2^2}{M_W^2} \propto \frac{1}{v_W^2}$$

In lowest order, v_Z is the same as v_W, but in higher order v_Z is modified by radiative corrections. The effect of these corrections can be described by

$$\rho \equiv \frac{v_W^2}{v_Z^2} = \frac{M_W^2}{M_Z^2 cos^2\bar{\theta}_W}$$

where $\bar{\theta}_W$ is the weak mixing angle defined as before, but now in terms of the running coupling constants. The dominant correction is due to the top quark loop which gives

$$v_Z^2 \simeq v_W^2 - \frac{3m_t^2}{32\pi^2} \tag{2}$$

There is also a weak logarithmic dependence on the Higgs mass that is not included here. The resulting expression for the Z mass is

$$M_Z^2 = \frac{1}{2}(g_1^2(M_Z) + g_2^2(M_Z))\left(\frac{1}{2\sqrt{2}G_F} - \frac{3m_t^2}{32\pi^2}\right)$$
$$= \frac{2\pi\alpha(M_Z)}{sin^2\bar{\theta}_W cos^2\bar{\theta}_W}\left(\frac{1}{2\sqrt{2}G_F} - \frac{3m_t^2}{32\pi^2}\right)$$

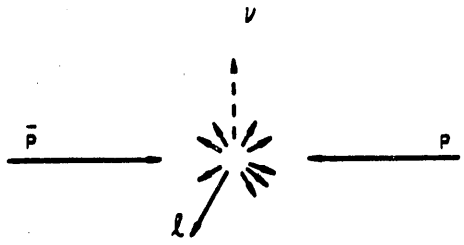

Fig. 42. W decay into $l\nu$ in a $\bar{p}p$ collision.

At this level, four experimental inputs are needed to specify the electroweak sector. For example with α_{EM}, G_F, M_Z, and one other (M_W or $sin^2\bar{\theta}_W$), the values of m_t and $sin^2\bar{\theta}_W$ or M_W can be predicted. Measuring these would provide a test of the Standard Model at the level of the electroweak radiative corrections.

9.2. The W Mass

UA2 [31] and CDF [32] have produced the first precision measurements ($\sim \frac{1}{2}\%$) of the W mass. This is a difficult measurement because of the neutrino in the final state. As opposed to the leptonic decay of the Z ($Z \rightarrow l^+l^-$) in which there are two well measured particles with a well understood resolution function, the leptonic decay of the W ($W \rightarrow l^{\pm}\nu$) yields one well measured particle plus the neutrino. Since the neutrino does not interact in the detector, its momentum can only be inferred using conservation of momentum. Figure 42 shows a $\bar{p}p$ collision producing hadronic debris plus a W that decays into $l\nu$. Since the initial $\bar{p}p$ state has zero net momentum, the final state must also have no net momentum.

$$\sum P_f = 0$$

$$P_l + P_\nu + \sum_{\text{hadrons}} P = 0$$

$$P_\nu = -P_l - \sum_{\text{hadrons}} P$$

In principle this can be measured well. In practice there are two major difficulties. First, only the transverse components of P_ν can be calculated, because in hadron collisions significant longitudinal momentum can be carried by particles going undetected down the beam pipe. Second, the energy resolution for the neutrino is much worse than for the charged lepton, and the resolution function is difficult to measure. This is so because the determination of P_T^ν (actually E_T in the calorimeter) depends on the measurement of the transverse momenta of all other particles, charged and neutral, produced in the event. Moreover, the energy response of detectors is not perfectly linear. Thus the signal produced by many low energy particles is not the same as that of a single particle with the same total energy.

In order to understand the measurement of P_T^ν, a variety of studies have been carried out.

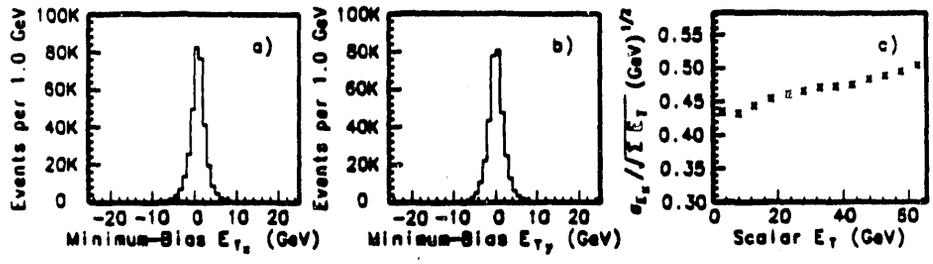

Fig. 43. (a) E_{T_x} and (b) E_{T_y} for CDF minimum bias events. (c) The resolution in E_{T_x} as a function of the net scalar E_T.

– An event sample obtained with a simple $\bar{p}p$ interaction trigger (minimum bias data) was used to study the resolution in the $\boldsymbol{E}_T$ balance for the underlying event, the soft hadronic debris produced along with the W. Figure 43a,b shows, for minimum bias events, the x and y components of the net $\boldsymbol{E}_T \equiv \sum_i \boldsymbol{E}_{T_i}$, where the sum is over all calorimeter cells and $\boldsymbol{E}_{T_i}$ is directed from the interaction vertex to the calorimeter cell. The mean is zero as it should be, and the resolution is plotted verses the net scalar E_T ($\equiv \sum |E_{T_i}|$) in Figure 43c.
– To minimize the dependence on higher order QCD W production diagrams as well as on jet fragmentation, both CDF and UA2 restrict their data sample to low P_T Ws. CDF removes events containing hadron jets with $P_T > 7$ GeV/c; UA2 excludes events in which the reconstructed P_T^W is greater than 20 GeV/c. Even with these restrictions, there remain lower energy jets recoiling against the W. Both groups measure the calorimeter response as a function of hadron energy so that the detector response to the recoil jet can be correctly modeled.
– If the P_T of the W is to be correctly measured, the calorimeter energy deposited by the charged lepton must be separated from that due to the recoil jets and underlying event. This requires understanding the transverse size of the lepton deposition. If the lepton energy is properly removed, $\boldsymbol{E}_T^\nu + \boldsymbol{E}_T^l$ should agree with a simulation of $-\sum_{\text{hadrons}} \boldsymbol{E}_T$ both parallel and perpendicular to the charged lepton direction. This comparison is shown for CDF data in Figure 44.
– Much of the understanding and modeling of the detector's hadron response can be checked by studying $Z \to l^+l^-$ events, which are kinematically similar to W events but in which the neutrino is replaced by a well measured charged lepton. The comparison of data to the prediction of the detector model for UA2 is shown in Figure 45.

The mass of the W is obtained from the shape of the transverse mass distribution. Transverse mass is the three dimensional analog of the four dimensional invariant mass.

$$M_T = \sqrt{2P_T^l P_T^\nu (1 - \cos\Delta\phi^{l\nu})}$$

where $\Delta\phi^{l\nu}$ is the azimuthal separation between the leptons. The transverse mass must be used because P_z^ν is not measured. The expected shape is simulated as a function of the W mass, and a maximum likelihood fit to the data establishes the W mass and its uncertainty. Figure 46 shows the data and the expected shape for the best fit mass for both the UA2 and CDF samples. The high mass falling edge, which is most sensitive to M_W, is well modeled. As a further check that the detector modeling used in the

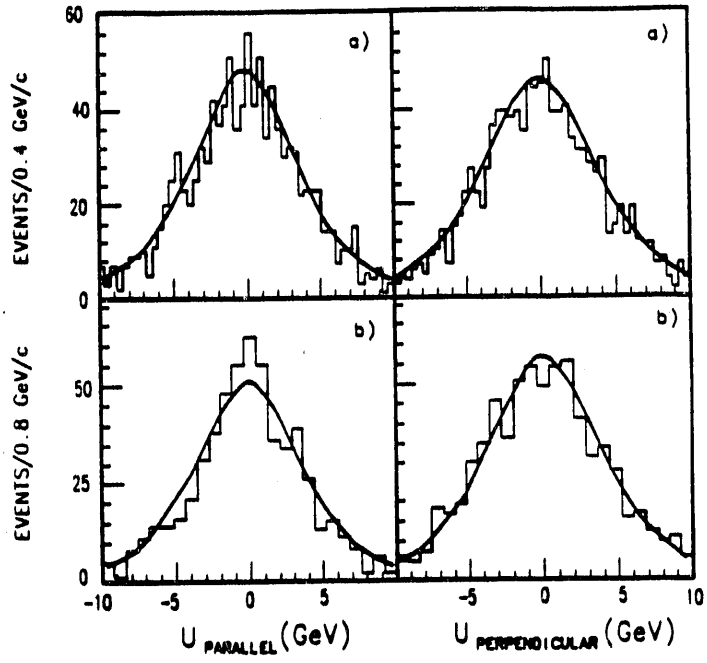

Fig. 44. Projections of the net hadronic vector E_T parallel to and perpendicular to the charged lepton in CDF (a) $W \to e\nu$ and (b) $W \to \mu\nu$ events. The curves are the predictions of the detector simulation.

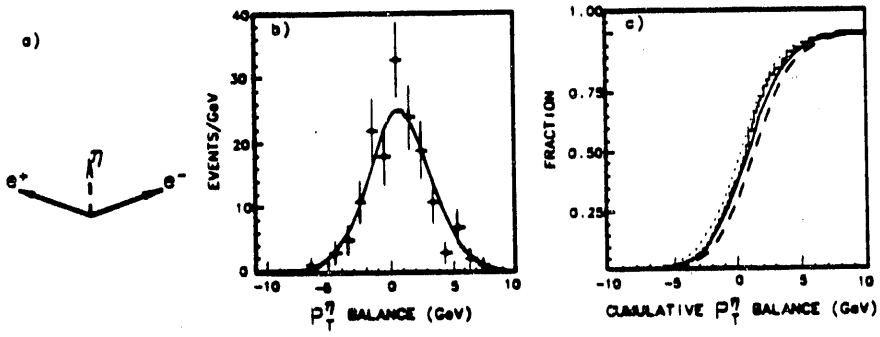

Fig. 45. Momentum balance in the η direction in UA2 $Z \to e^+e^-$ events. (a) Definition of η direction. (b) Data distribution compared with the prediction of the detector model. (c) The cumulative distribution. The dotted and dashed lines show limits of the detector model used for assigning systematic uncertainty.

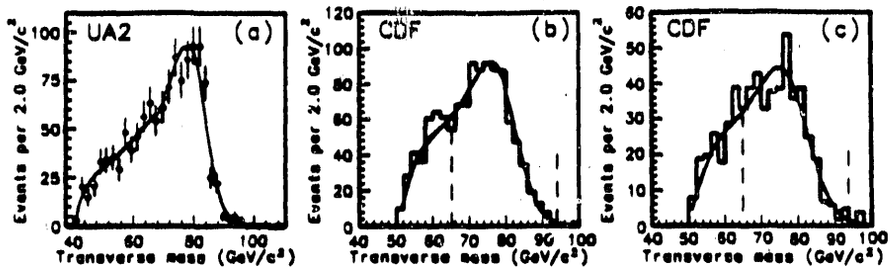

Fig. 46. Transverse mass distributions for (a) UA2 $W \to e^+e^-$ (b) CDF $W \to e^+e^-$ and (c) CDF $W \to \mu^+\mu^-$ data.

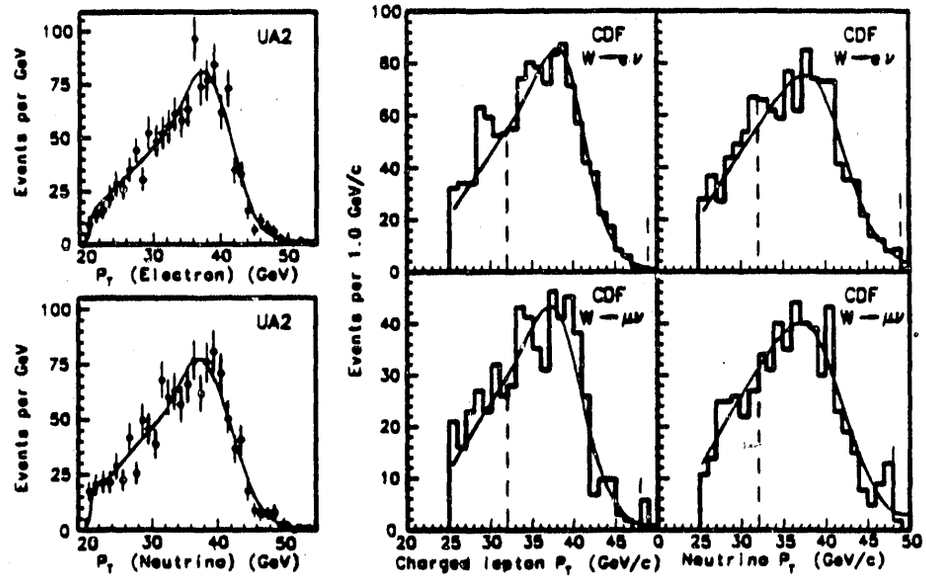

Fig. 47. Comparison of data and detector modeling for each type of lepton in W decay.

mass determination is correct, the data and predictions for the lepton P_T spectra are compared in Figure 47.

The results of the mass measurement are quoted with statistical, systematic, and scale uncertainties. The major sources of systematic uncertainty are the detector hadron and missing E_T resolutions, the shape of the W P_T spectrum, and the proton structure functions. The uncertainty in the detector's energy scale is quoted separately because it cancels in the ratio of masses measured in the same detector. The UA2 result is

$$M_W = 80.79 \pm 0.31(\text{stat}) \pm 0.21(\text{syst}) \pm 0.81(\text{scale})\ GeV/c^2$$

They reduce the effect of the large scale uncertainty by measuring the ratio of the W

and Z masses

$$\frac{M_W}{M_Z} = 0.8831 \pm 0.0048(\text{stat}) \pm 0.0026(\text{syst})\ GeV/c^2$$

and then using the precision LEP value for M_Z to get

$$M_W = 80.49 \pm 0.43(\text{stat}) \pm 0.24(\text{syst})\ GeV/c^2$$

CDF results from $W \rightarrow e\nu$ and $W \rightarrow \mu\nu$ decays are

$$M_W = 79.91 \pm 0.35(\text{stat}) \pm 0.24(\text{syst}) \pm 0.19(\text{scale})\ GeV/c^2 \qquad (W \rightarrow e\nu)$$
$$M_W = 79.90 \pm 0.53(\text{stat}) \pm 0.32(\text{syst}) \pm 0.08(\text{scale})\ GeV/c^2 \qquad (W \rightarrow \mu\nu)$$

The CDF magnetic spectrometer has a small enough scale error so that calculating M_W/M_Z and normalizing to the LEP M_Z produces a slightly larger overall M_W uncertainty due to the large statistical error in the Z sample. The final CDF result after combining the two samples is

$$M_W = 79.91 \pm 0.39\ GeV/c^2$$

The CDF and UA2 results are consistent.

$$M_W^{UA2} - M_W^{CDF} = 0.58 \pm 0.63\ GeV/c^2$$

The combined UA2 and CDF result is

$$M_W^{CDF+UA2} = 80.13 \pm 0.31\ GeV/c^2$$

What does this tell us about the consistency of the Standard Model? Five quantities have been measured accurately: G_F and α_{EM} in beta decay and atomic physics experiments, M_Z and $sin^2\overline{\theta}_W$ at LEP, and M_W in $\overline{p}p$ experiments. A global fit to the Standard Model equations can be done with the overall χ^2 indicating whether the data are consistent with the theory. We will not do that here. Rather, for pedagogic value, we will make a few comparisons of data and theory.

The measured W mass can be compared to the predicted value using

$$M_W^2 = \frac{\pi\alpha(M_Z)}{\sqrt{2}G_F sin^2\overline{\theta}_W}$$

and the quantities

$$G_F = 1.1664 \times 10^{-5}\ GeV^{-2}$$
$$\alpha_{EM}^{-1}(M_Z) = 128.8\ (\pm 0.2) \qquad [33]$$
$$sin^2\overline{\theta}_W = 0.2318 \pm 0.0011 \qquad (LEP)[34]$$

The Standard Model prediction and the measured value are in good agreement.

$$M_W^{sm} = 79.87 \pm 0.20\ GeV/c^2$$
$$M_W^{\overline{p}p} = 80.13 \pm 0.31\ GeV/c^2$$
$$M_W^{\overline{p}p} - M_W^{sm} = 0.26 \pm 0.37\ GeV/c^2$$

Alternatively we can turn this around and use the measured W mass to deduce the value of the fine structure constant at $q^2 = M_Z^2$.

$$\alpha_{EM}(M_Z) = \frac{\sqrt{2}}{\pi} G_F M_W^2 sin^2\overline{\theta}_W$$
$$\alpha_{EM}^{-1}(M_Z) = 128.0 \pm 1.2$$

This is 7.5 σ away from the low q^2 value of 137.0. Thus within the context of the Standard Model, the fine structure constant is observed to run.

We can also place an upper limit on the mass of the top quark using the Standard Model formalism. The ρ parameter can be calculated from the values noted above plus the LEP Z mass, $91.17 \pm 0.020\ GeV/c^2$ [34].

$$\rho = \frac{v_W^2}{v_Z^2} = \frac{M_W^2}{M_Z^2 cos^2\overline{\theta}_W}$$
$$= 1.006 \pm 0.009$$

This places a limit the top quark mass when we use the correction to v_Z (equation 2).

$$\rho = \frac{v_W^2}{v_Z^2} \simeq 1 + \frac{3M_{\text{top}}^2 G_F}{8\sqrt{2}\pi^2}$$
$$\overline{M}_{\text{top}} = 138\ GeV/c^2 \qquad (149 \text{ if } M_{\text{Higgs}} = 250\ GeV/c^2)$$
$$M_{\text{top}} < 236\ GeV/c^2 \quad @90\%CL$$

These numbers are similar to those obtained from LEP measurements of the Z mass, the Z partial widths, etc. (mean value of 142 GeV/c^2, 90% CL limit of 200 GeV/c^2 [34]).

9.3. Charge Asymmetries

In W and Z decay, the decay angular distributions in the vector boson rest frame are sensitive to the weak couplings. When viewed in the laboratory frame, these distributions also depend on the proton structure functions.

9.3.1. $q\overline{q} \rightarrow e^+e^-$

The e^+e^- final state can be produced by either a virtual photon or a Z^0. Thus the cross section contains three terms corresponding to $q\overline{q} \rightarrow \gamma^* \rightarrow e^+e^-$, $q\overline{q} \rightarrow Z^0 \rightarrow e^+e^-$, and an interference term. If the measurement is made near the Z^0 pole, the γ^* term is very small. Moreover, the interference term changes sign across the resonance; thus the integrated effect across the resonance is small. Therefore it is the Z^0 term that dominates, and the cross section can be written as follows.

$$\frac{d\sigma}{d\Omega} = \frac{3\alpha^2 s}{4\left[(s - M_Z^2)^2 + M_Z^2\Gamma_Z^2\right]}\left[(v_e^2 + a_e^2)(v_q^2 + a_q^2)(1 + cos^2\theta) + 8v_e a_e v_q a_q cos\theta\right]$$

where v and a are the vector and axialvector charges, and θ is the angle between the quark and the e^-. Note that the $cos\theta$ term is the interference between the vector and axialvector currents and is explicitly parity violating. The angular distribution thus can be written as

$$1 + cos^2\theta + x\, cos\theta$$
$$x = \frac{8v_e a_e v_q a_q}{(v_e^2 + a_e^2)(v_q^2 + a_q^2)}$$

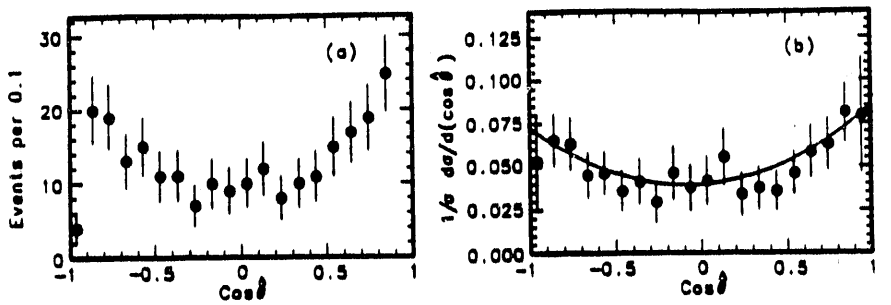

Fig. 48. (a) The raw angular distribution for Z decay in CDF data. (b) The distribution after correcting for the detector acceptance.

and the asymmetry as

$$A = \frac{\int_0^1 \frac{d\sigma}{d\Omega} d\,cos\theta - \int_{-1}^0 \frac{d\sigma}{d\Omega} d\,cos\theta}{\int_{-1}^1 \frac{d\sigma}{d\Omega} d\,cos\theta} = \frac{3x}{8}$$

In $\bar{p}p$ collisions, the quark almost always comes from the proton. Thus there is little ambiguity in the angle θ. What differentiates this measurement from easily measured asymmetries at LEP ($e^+e^- \rightarrow \mu^+\mu^-$) is the dependence on the light quark weak charges. However because the weak vector charge of the electron is proportional to $4\,sin^2\theta_W - 1$, which is close to zero, only a large departure of the light quark weak charges from expectations would produce an observable effect.

The angular distribution in Z decay for the CDF data [35] is shown in Figure 48. The measured asymmetry in the 250 event CDF sample is

$$A = 0.053 \pm 0.059(\text{stat}) \pm 0.004(\text{syst})$$

From this the weak angle is determined to be

$$sin^2\bar{\theta}_W = 0.228^{+0.017}_{-0.015}(\text{stat}) \pm 0.002(\text{syst})$$

This is consistent with the much more precise values of $sin^2\bar{\theta}_W$ measured in other processes at LEP.

3.3.2. $W \rightarrow e\nu$

The charged current is pure V-A. Thus the angular distribution in W decay follows from simple helicity arguments. Figure 49a shows the production of a W^+. Since the u quark almost always comes from the proton and only left handed fermions and right handed antifermions interact via the charged weak interaction, the W^+ is produced polarized in the antiproton direction. Conservation of angular momentum in the decay causes the positron to be emitted preferentially in the antiproton direction. Similarly the electron from W^- decay tends to be produced in the proton direction (Fig. 49b). This results in the decay angular distribution in the W rest frame

$$\frac{d\sigma}{d\,cos\theta^*} \sim (1 + cos\theta^*)^2$$

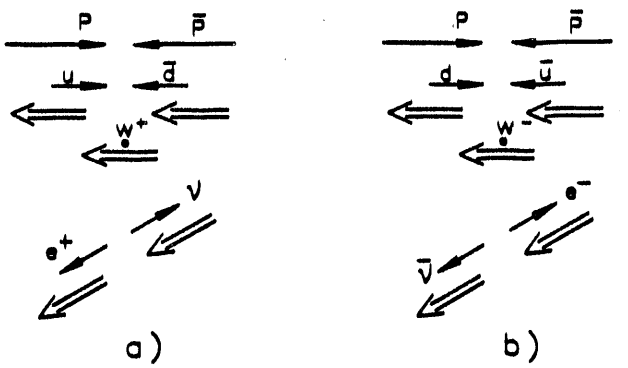

Fig. 49. (a) W^+ and (b) W^- production and decay in $\bar{p}p$ interactions. The double arrows indicate the spin directions.

where θ^* is the angle between the electron and proton or between the positron and antiproton.

In order to transform into the W rest frame, P_z^ν is needed. Although it can't be measured directly, the constraint

$$M_W^2 = (E_l + E_\nu)^2 - (P_l + P_\nu)^2$$

can be used to calculate P_z^ν. Unfortunately a quadratic ambiguity remains. At CERN Collider energies, the correct solution is most often the one with the lower P_z^W. Figure 50 shows UA1 data in good agreement with the V-A prediction [36]. At Fermilab energy, both solutions are quite probable because the Feynman x of produced W bosons is so small. Thus CDF must look at the angular distribution in the lab frame. Here a structure function effect produces an asymmetry larger than that from V-A and of the opposite sign. In the proton, the u quark momentum distribution, $u(x)$, is harder than the d quark distribution, $d(x)$. Thus a W^+, produced from $u\bar{d}$ annihilation, tends to be moving in the u or proton direction. This throws the decay products of the W^+, in particular the e^+, in the proton direction. Thus the structure functions cause e^+ to go in the p direction and e^- to go in the $\bar{p}$ direction, opposite to the V-A helicity effect. Figure 51 shows the CDF W decay asymmetry in the lab frame [37]. The asymmetry $A(\eta)$ is defined as

$$A(\eta) \equiv \frac{\sigma^+(\eta) - \sigma^-(\eta)}{\sigma^+(\eta) + \sigma^-(\eta)}$$

where η is the pseudorapidity ($\eta = -ln\ tan\frac{\theta}{2}$), and the + (-) cross section contains events where the product of the lepton charge and the pseudorapidity is > (<) zero. The data are consistent with the u to d ratio in most of the modern sets of structure functions.

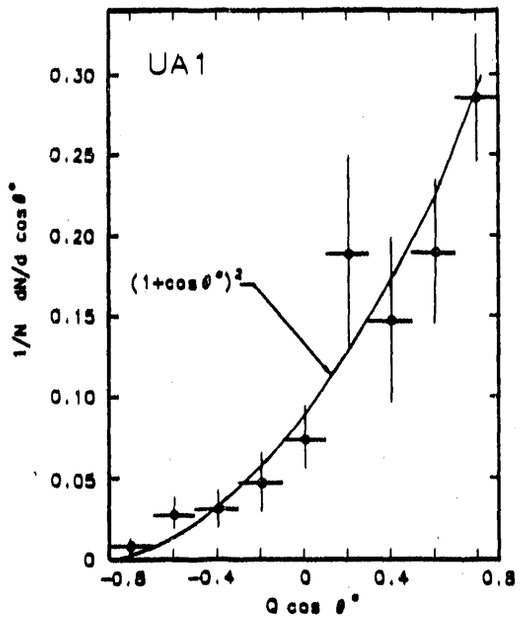

Fig. 50. The UA1 W decay angular distribution in the W rest frame compared with the V-A prediction.

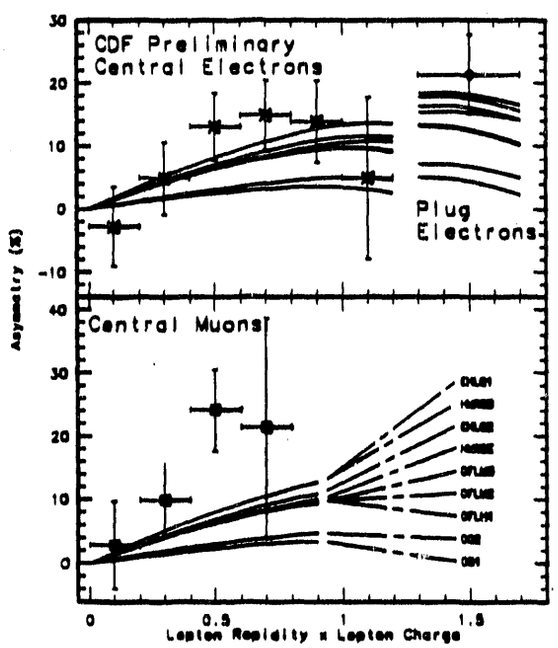

Fig. 51. The CDF W decay angular distribution in the lab frame compared to theoretical expectations for a number of sets of proton structure functions.

3.4. The W Lifetime

The lifetime of the W can be deduced from the ratio of the production cross section times branching ratio for $W \to e\nu$ and $Z \to e^+e^-$.

$$R \equiv \frac{\sigma B(W \to e\nu)}{\sigma B(Z \to ee)}$$

This quantity is relatively free from experimental systematic uncertainties, since uncertainties in the integrated luminosity of the data sample, acceptance, trigger efficiencies, etc. largely cancel in the ratio. Writing the branching ratio as the partial width over the total width, we get

$$R = \frac{\sigma(\bar{p}p \to W + X)\Gamma(W \to e\nu)\Gamma(Z)}{\sigma(\bar{p}p \to Z + X)\Gamma(Z \to ee)\Gamma(W)}$$

The ratio of the production cross sections is well predicted by QCD and the known structure functions [38].

$$\frac{\sigma(\bar{p}p \to W + X)}{\sigma(\bar{p}p \to Z + X)} = 3.23 \pm 0.03 \qquad @\ \sqrt{s} = 1.8\,TeV$$

$$3.20 \pm 0.07 \qquad @\ \sqrt{s} = 0.63\,TeV$$

The partial width of the W is a standard charged current calculation

$$\Gamma(W \to e\nu) = 223.6 \pm 0.3\,MeV$$

and the Z widths have been measured at LEP [34]

$$\Gamma(Z \to ee) = 83.2 \pm 0.4\,MeV$$
$$\Gamma(Z) = 2.485 \pm 0.009\,GeV$$

Values for R have been measured by UA1 [39], UA2 [40], and CDF [41].

$$\begin{array}{lcll} R & = & 10.2 \pm 0.8\,(\text{stat}) \pm 0.4\,(\text{syst}) & CDF \\ & & 9.38^{+0.82}_{-0.72}\,(\text{stat}) \pm 0.25\,(\text{syst}) & UA2 \\ & & 9.5^{+1.1}_{-1.0} & UA1 \end{array}$$

Using this and the quoted values for the widths and the cross section ratio, we get for the full width of the W

$$\begin{array}{lcll} \Gamma(W) & = & 2.11 \pm 0.19\,GeV & CDF \\ & & 2.28 \pm 0.21\,GeV & UA2 \\ & & 2.25 \pm 0.27\,GeV & UA1 \end{array}$$

Since the dominant uncertainty is statistical in each case, we can average these values to obtain

$$\Gamma(W) = 2.20 \pm 0.12\,GeV$$

The total W width is sensitive to any open W decay channel beyond $u\bar{d}$, $c\bar{s}$, $e\nu$, $\mu\nu$, and $\tau\nu$. For example, if $W \to t\bar{b}$ were kinematically allowed, then the predicted $\Gamma(W)$ would increase. Although $t\bar{b}$ would be an open channel only up to $M_{\text{top}} \approx 75\,GeV/c^2$, this measurement is still important. Unlike direct top searches, this one is valid no

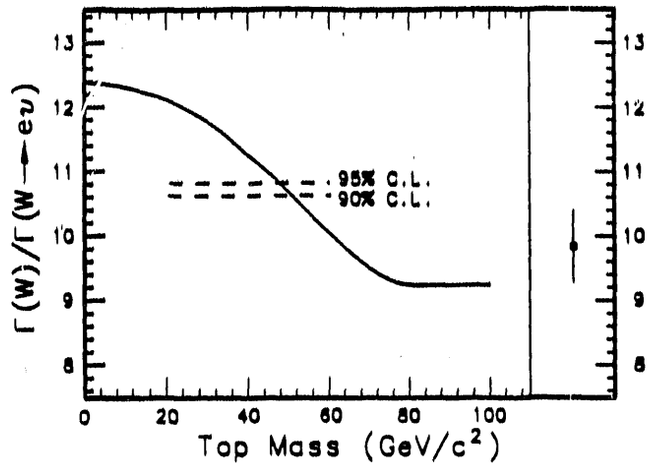

Fig. 52. The world average $W \to e\nu$ inverse branching ratio is shown as the data point on the right. The Standard Model prediction as a function of the top quark mass is shown as the solid line. The experimental 90% and 95% confidence level limits are shown with dashed lines.

matter how the top quark decays, for example top decaying into a charged Higgs which then decays into $c\bar{s}$. Such decay schemes contain no isolated leptons and thus would be missed in the direct top quark searches.

In order to set a top quark mass limit, we calculate the inverse branching ratio $\Gamma(W)/\Gamma(W \to e\nu)$. Unlike $\Gamma(W)$ alone, this ratio should be independent of the precise value of M_W. Moreover, there is a gaussian uncertainty in the inverse branching ratio since it is proportional to the number of Z events observed, and the statistical fluctuation on N_Z dominates the uncertainty. The three collaborations find

$\frac{\Gamma(W)}{\Gamma(W\to e\nu)}$	=	9.44 ± 0.85	CDF
		10.20 ± 0.94	$UA2$
		10.06 ± 1.21	$UA1$
Average	:	9.84 ± 0.56	

The resulting lower limits on the top quark mass are (Fig. 52)

$> 51\ GeV/c^2$	@ 90% CL
$> 48\ GeV/c^2$	@ 95% CL

independent of how the top quark decays.

3.5. Lepton Universality at $q^2 = M_W^2$

We know from $\pi \to l\nu$ decay, ν deep inelastic scattering, and the τ lifetime that at low to moderate q^2 the charged current couplings to the leptons (g_e, g_μ, g_τ) are approximately equal. Since gauge couplings run, it is interesting to compare the coupling constants at large q^2, specifically at $q^2 = M_{W,Z}^2$. For the neutral current, LEP results

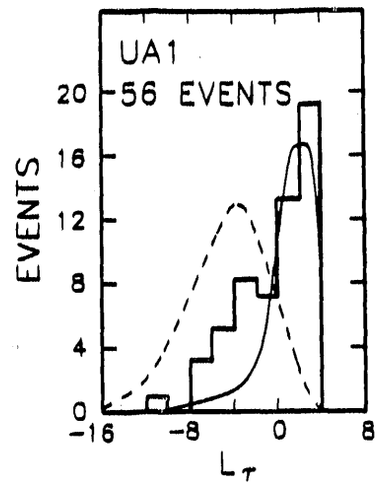

Fig. 53. The τ log-likelihood for the UA1 data (histogram) compared to the prediction from a τ Monte Carlo (solid curve) and to UA1 jet data (dashed curve).

on the partial widths of the Z to ee, $\mu\mu$, and $\tau\tau$ confirm lepton universality at the $\sim 2\%$ level.

For the charged current, we similarly compare the partial widths of the W into leptons.

$$\Gamma(W \to \tau\nu)/\Gamma(W \to \mu\nu)/\Gamma(W \to e\nu) = g_\tau^2/g_\mu^2/g_e^2$$

At hadron colliders, τ identification is a difficult problem. The leptonic decays of the τ cannot be used because $W \to \tau\nu \to e\nu\nu\nu$ cannot be separated from $W \to e\nu$. Thus one is forced to look for hadronic τ decay which is quite difficult because of the enormous cross section for QCD produced jet background.

UA1 [42], UA2 [43], and CDF [44] rely on two important event characteristics to separate the signal from background, the large missing E_T in $\bar{p}p \to W \to \tau\nu \to$ hadrons $+ \nu + \nu$, and the fact that τ decay produces narrow, low multiplicity jets. For example, UA1 forms a τ log-likelihood function based on the size of the jet, the angular separation between the highest P_T track and the jet axis, and the charged particle multiplicity (Fig. 53). CDF is able to confirm that its signal is indeed from τ decay by looking at the track multiplicity distribution (Fig. 54). Clusters from τ decay should have mostly 1 or 3 prongs.

The results from the three groups are:

$$\begin{aligned}
UA1: \quad & g_\tau/g_e = 1.01 \pm 0.09 \pm 0.05 \\
& g_\mu/g_e = 1.05 \pm 0.07 \pm 0.08 \\
UA2: \quad & g_\tau/g_e = 0.997 \pm 0.056 \pm 0.042 \\
CDF: \quad & g_\tau/g_e = 0.97 \pm 0.07
\end{aligned}$$

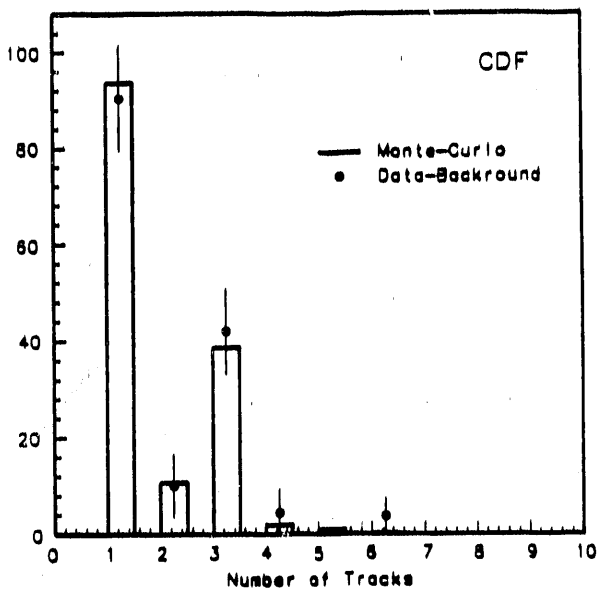

Fig. 54. Number of tracks in a 10° cone around the center of the τ cluster for CDF data. The background subtracted data are compared to a Monte Carlo prediction.

The UA2 and CDF results are preliminary. The combined result for W decay is

$$\frac{g_\tau}{g_e} = 0.99 \pm 0.04$$

in agreement with lepton universality.

4. The Search for the Top Quark

This is purely an experimental question of the strategy for searching for this as yet unobserved heavy fermion. I will present in detail the methods employed by the most sensitive experiment, CDF [48]. At the end I will summarize the results from UA1 and UA2.

4.1. Introduction

Within the context of the Standard Model, the top quark must exist. The b quark must have a partner since it has a measured weak isospin of 1/2 [45]. Moreover, anomaly cancellation requires that for each generation

$$N_c \sum_{\text{quarks}} Q_i + \sum_{\text{leptons}} Q_i = 0$$

This fails for the third generation unless the top quark exists.

The search for the top quark has been underway since the bottom quark was discovered at Fermilab in 1977. The initial guess for the top mass was 15 GeV/c^2 based

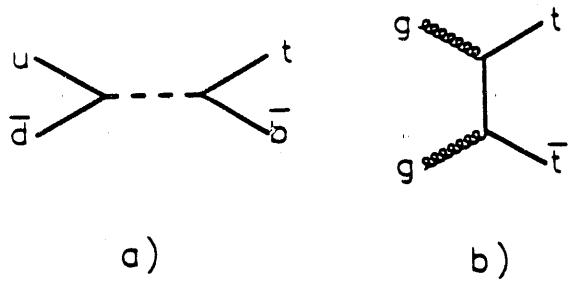

Fig. 55. Top quark production via (a) W decay and (b) gluon fusion.

on the apparent geometric progression of the quark masses: M_s (0.5 GeV/c^2), M_c (1.5 GeV/c^2), M_b (5 GeV/c^2). Since that time there has been a steady increase in the experimental lower limit on the mass as shown in Table 3 [46]. The $\bar{p}p$ limit from the W width was presented in the previous section. Here we will consider the direct top quark searches.

e^+e^-:	Limit:	Method:
PETRA/PEP	15 - 22 GeV/c^2	R, event shape
Tristan	30 GeV/c^2	R, event shape
SLC	41 GeV/c^2	Z^0 width, event shape
LEP	45 GeV/c^2	Z^0 width, event shape
$\bar{p}p$:		
Tevatron and Sp$\bar{p}$S	48 GeV/c^2	W width
UA1	60 GeV/c^2	isolated leptons
UA2	69 GeV/c^2	isolated leptons
CDF	91 GeV/c^2	isolated leptons

Table 3
Lower limits on the top quark mass

In $\bar{p}p$ collisions, there are two major top quark production mechanisms as shown in Figure 55, from W decay and through gluon fusion. The W decay diagram only contributes significantly if $M_{top} < M_W - M_b \approx 75\ GeV/c^2$. At $\sqrt{s} = 1.8\ TeV$, $t\bar{t}$ production through gluon fusion dominates for all M_{top} (Fig 56) [47].

The decay of the top quark in the minimal Standard Model occurs via the charged weak current, $t \to Wb$, with the W real or virtual depending on the top quark mass.

$$gg \to t\bar{t} \to W^{(*)}b + W^{(*)}\bar{b}$$

Each W decays with a branching ratio of 1/9 into each generation of leptons, and a branching ratio of 3/9 (due to color) into $u\bar{d}$ or $c\bar{s}$. The all hadronic final state has the largest combined branching ratio (4/9), but the $t\bar{t}$ signal would be overwhelmed by QCD production of multiple quark and gluon jets.

Thus in order to observe a signal above background, at least one W must be required to decay into leptons. We will first consider the case where both W bosons decay into leptons, one into $e\nu$ and the other into $\mu\nu$. Then we will look at the final state in which

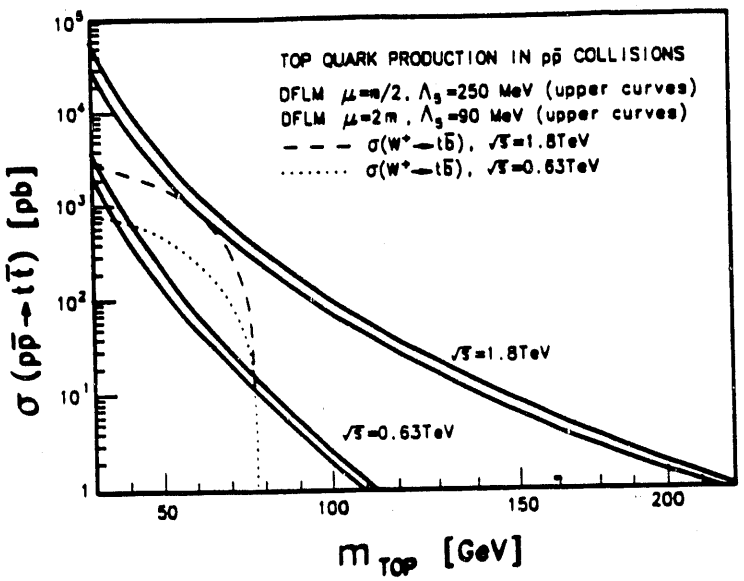

Fig. 56. Expected top quark production cross section in $\bar{p}p$ collisions at both CERN and Fermilab energies.

one W decays into $e\nu$ with the other W decaying into quarks. Finally we will consider extensions to both of these searches.

4.2. $t\bar{t} \to e\mu X$

The decay chain

$$t\bar{t} \to WbW\bar{b} \to e\nu b\mu\nu\bar{b}$$

provides the final state with the lowest background. Unlike the single lepton modes, QCD production of W + jets doesn't contribute. And unlike the decay into two electrons or two muons, there is no background from the production of γ^*, Z^0, J/ψ, or Υ. The major background

$$gg \to b\bar{b} \to ce\nu\bar{c}\mu\nu$$

produces relatively low P_T leptons. Another possible background, W pair production ($q\bar{q} \to W^+W^- \to e\nu\mu\nu$) doesn't have a cross section competitive with $t\bar{t}$ for $M_{top} \lesssim 150\ GeV/c^2$. Possible background from $Z \to \tau\tau \to e\nu\nu\mu\nu\nu$ can be easily removed as we shall see.

It is important to note that large P_T charged leptons provide a good signature because they can be cleanly separated from the much more abundant charged hadrons. Figures 57 and 58 show the electron and muon selection variables for $W \to l\nu$ events. The hadron background is rather flat in these variables. The detection efficiency for high P_T electrons or muons incident on the active part of the detector is 75-95% depending on the criteria used.

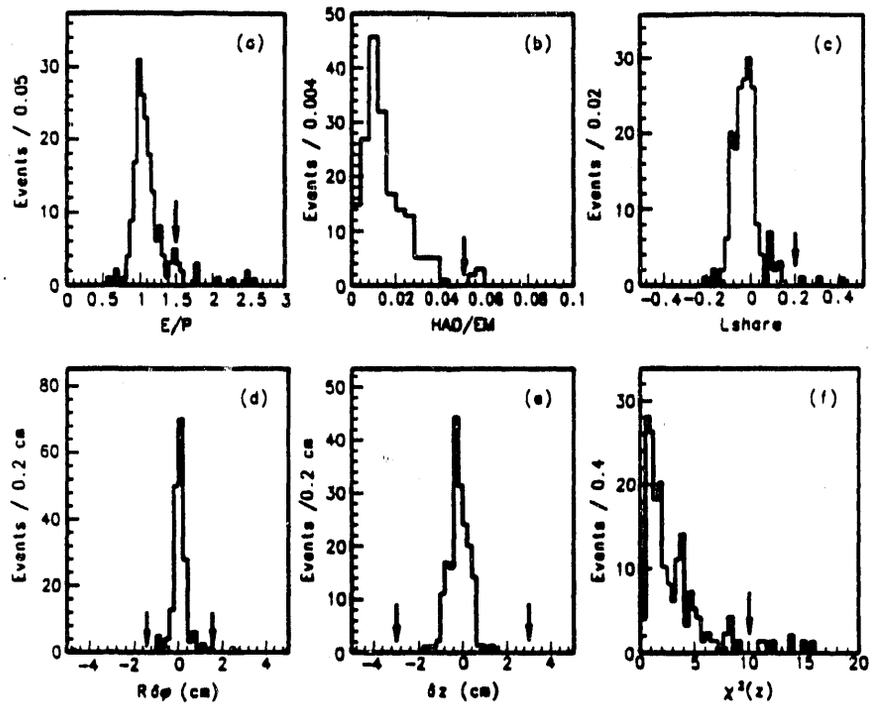

Fig. 57. Distributions from $W \to e\nu$ events of variables used to select electrons. The arrows show the location of the usual cuts. (a) The ratio of the calorimeter energy to the track momentum. (b) The ratio of energies deposited in the hadronic and electromagnetic calorimeters. (c) A variable that describes the transverse size of the calorimeter shower. (d) Matching between the extrapolated track and the shower centroid in the azimuthal direction. (e) Matching between the extrapolated track and the shower centroid in the beam direction. (f) The chisquare for the comparison of the transverse shower shape with that measured in an electron test beam.

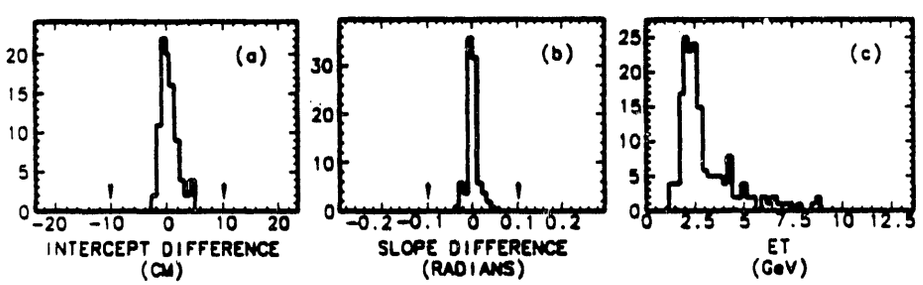

Fig. 58. Distributions from $W \to \mu\nu$ events of variables used to select muons. (a) The difference between the extrapolated track from the central tracking chamber and the location of the track stub in the muon chamber. (b) The difference in slope between the extrapolated track and the muon chamber track stub. (c) The total E_T in the calorimeter cell through which the muon passes.

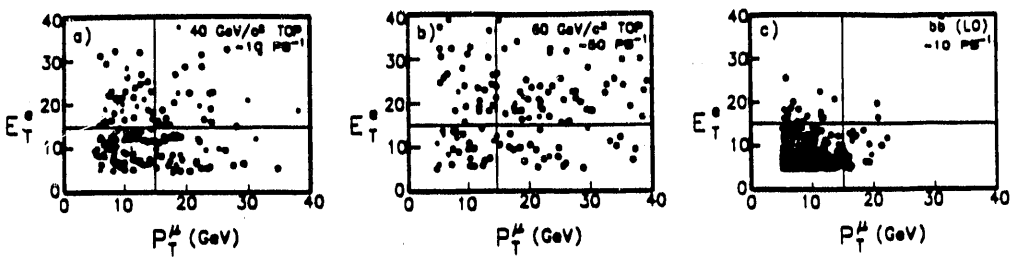

Fig. 59. Electron E_T versus muon P_T for Monte Carlo simulations of (a) 40 GeV/c^2 top, (b) 60 GeV/c^2 top, and (c) leading order $b\bar{b}$ production. The location of the cuts that will be applied to the data are shown.

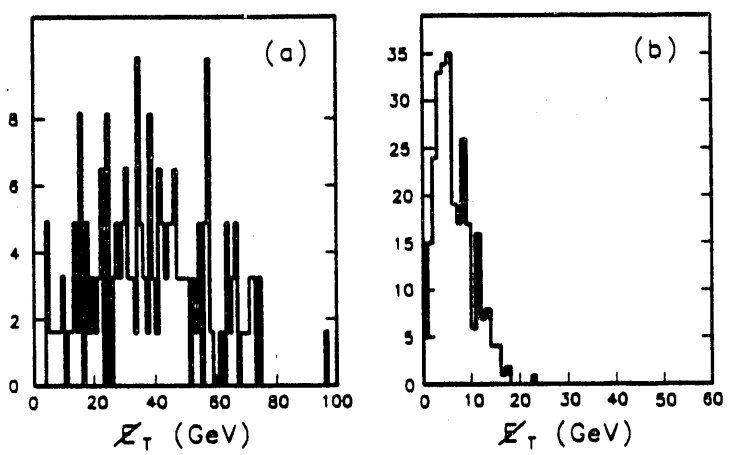

Fig. 60. Missing E_T distributions from (a) 80 GeV/c^2 top and (b) $b\bar{b}$ Monte Carlo samples. Note the difference in the missing E_T scales for the two figures.

There are a number of variables that are useful in separating signal from background.
– E_T of the electron and P_T of the muon. Top decay produces large P_T leptons, while $b\bar{b}$ background produces leptons with much lower P_T (Fig. 59).
– The missing E_T in the event. Events from $t\bar{t}$ production have large missing E_T due to the two large E_T neutrinos. Bottom events, on the other hand, have small missing E_T because the requirements of large E_T^e and P_T^μ select the region of the b decay Dalitz plot where P_T^μ is small (Fig. 60).
– The azimuthal angular separation, $\Delta\phi^{e\mu}$, between the electron and the muon. Top events would produce a broad $\Delta\phi^{e\mu}$ distribution because of the large mass of the decaying mesons. Bottom production is characterized by peaks near 0° and 180° (Fig. 61). Z decay, $Z \rightarrow \tau\tau \rightarrow e\nu\mu\nu$, produces a peak at 180° because of the low τ mass. Figure 62 shows these expected distributions.

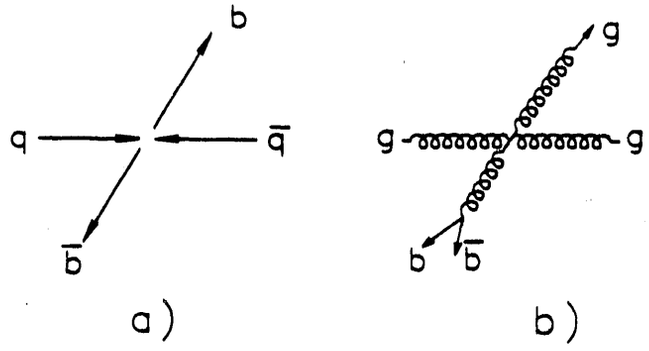

Fig. 61. (a) The leading order diagram for b production produces b quarks 180° apart in azimuth. (b) The gluon splitting next to leading order diagram produces b quarks very close in azimuth.

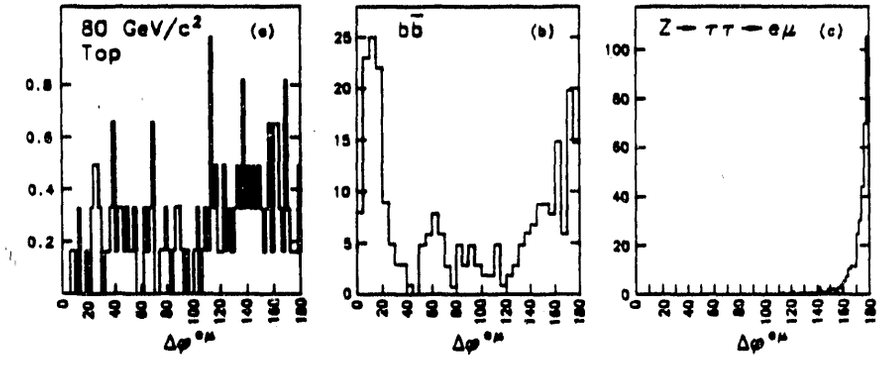

Fig. 62. The expected $e\mu$ azimuthal separation for (a) an 80 GeV/c^2 top quark, (b) $b\bar{b}$ production, and (c) $Z \to \tau\tau \to e\mu\nu\nu$.

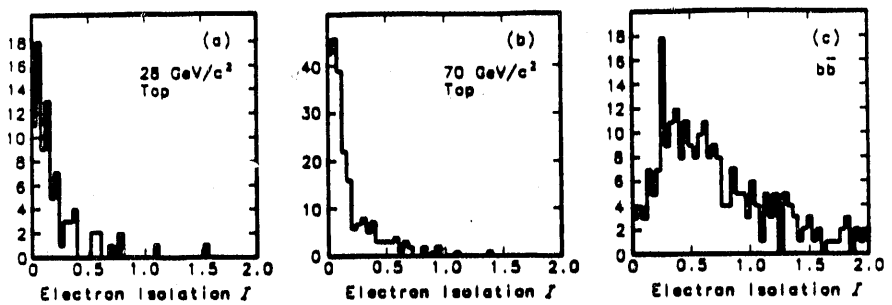

Fig. 63. Electron isolation in Monte Carlo samples of (a) 28 GeV/c^2 top, (b) 70 GeV/c^2 top, and (c) $b\bar{b}$ events.

– Lepton isolation. The isolation of an electron can be characterized by

$$I = \frac{E_T(\text{cone, R} = 0.7) - E_T^e}{E_T^e}$$

where E_T(cone, R = 0.7) is the transverse energy deposited in the calorimeter within a cone of radius 0.7 in $\eta - \phi$ space centered on the electron. For top decay ($t \rightarrow Wb \rightarrow e\nu b$), the large top mass results in a large separation between the e and b and thus an isolated electron. In bottom decay ($b \rightarrow e\nu c$), the electron is much closer to the charm quark and thus less isolated (Fig. 63).

The CDF $e\mu$ data were selected solely on the basis of E_T^e and P_T^μ. Figure 64 shows why the requirement on both variables was > 15 GeV. Only one $b\bar{b}$ background event was expected above that value for the integrated luminosity collected by CDF (4.1 pb^{-1}). Figure 65 shows the CDF data. The bulk of the data looks like $b\bar{b}$ production (compare Figure 65b,c,d with Figures 60, 62, and 63). However there is one event with very large E_T^e and P_T^μ. The characteristics of this event are given in Table 4. The event could be from $t\bar{t}$ decay, but it could just as well be a background event. With only one candidate, positive identification is impossible.

	Charge	P_T [GeV/c]	η	ϕ [degrees]
Central Electron	+	31.7	-0.8	132
Central Muon	–	42.5	-0.8	269
Forward Muon	+	9.9	-2.0	98
Jet 1		14	1.1	341
Jet 2		5	-2.8	88

Table 4
Characteristics of the top candidate event. Calorimeter E_T is used in the P_T column for the electron and jet clusters.

CDF calculated the upper limit on the $t\bar{t}$ production cross section using the calculated detection efficiency and Poisson statistics based on one observed event. Including the event without performing a background subtraction is conservative since it raises the calculated cross section upper limit. Also included in the calculation are the

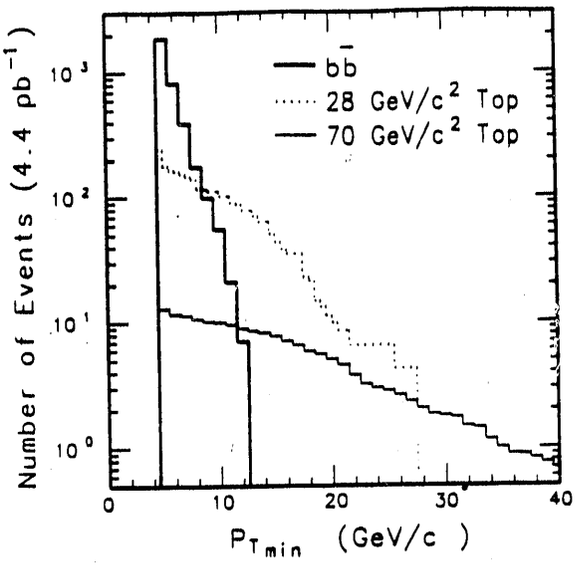

Fig. 64. Monte Carlo predictions for the event rates as a function of the minimum lepton P_T accepted.

systematic uncertainties from lepton identification efficiency, the calculated P_T distribution for $t\bar{t}$ production, the top quark fragmentation function, and the experiment's integrated luminosity. The 95% confidence level upper limit on the cross section as a function of the top mass is shown in Figure 66 along with the next to leading order theoretical prediction [47]. The mass limit is taken where the experimental upper limit crosses the lower end of the theoretical prediction. From this, CDF concluded that the top mass is greater than 72 GeV/c^2 at the 95% confidence level.

4.3. $t\bar{t} \rightarrow e\nu$ + jets

The final state containing a single electron plus jets

$$gg \rightarrow \bar{t}t \rightarrow W\bar{b}Wb \rightarrow e\nu\bar{b}q\bar{q}b$$

has a combined branching ratio 6 times larger than that for the $e\mu$ final state. There are however experimental difficulties that complicate this search. For $M_{top} \lesssim 120\ GeV/c^2$, the probability of detecting all four quark jets is small because the b quarks have low energy and consequently don't appear jetlike in the detector. This forced CDF to search for events with an electron, missing E_T, and at least two jets of observed $E_T > 10$ GeV.

There are two major sources of background. The production of b quarks

$$gg \rightarrow \bar{b}b \rightarrow e\nu\bar{c}q\bar{q}c$$

produces low E_T electrons and neutrinos. Moreover this background can be reduced by requiring the electron to be isolated (Fig. 67). In this analysis, isolation is defined as the E_T in the calorimeter cells surrounding the cell hit by the electron. The more serious

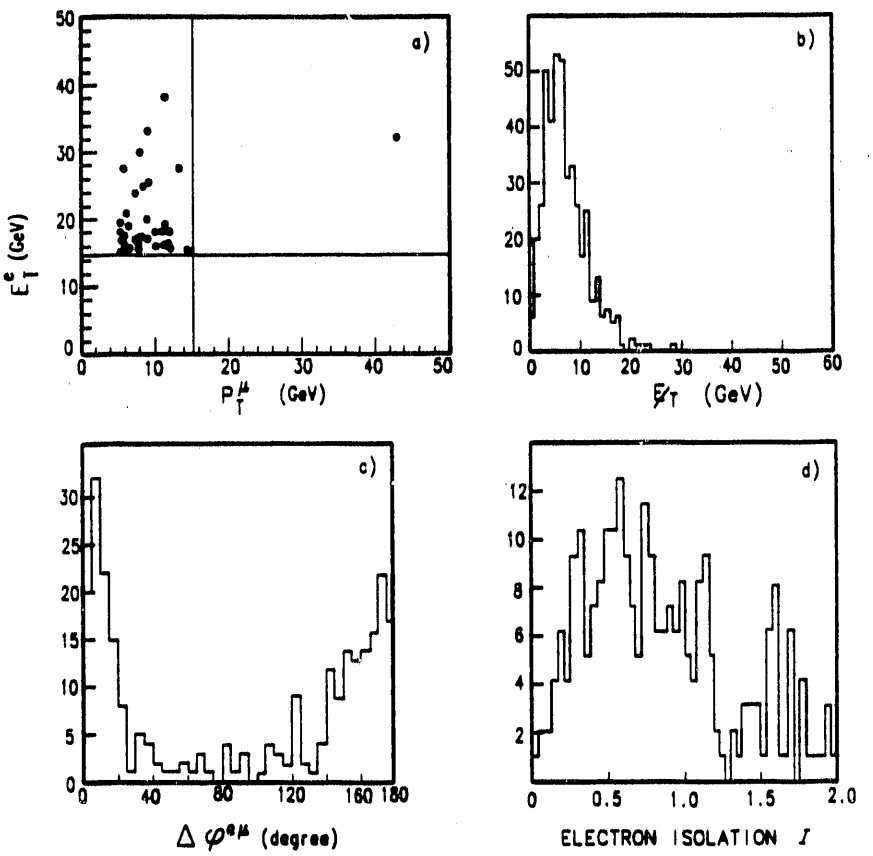

Fig. 65. CDF data from the $e\mu$ top quark search. (a) The electron E_T versus the muon P_T. The lines show the location of the cuts in these variables. (b) The missing E_T, (c) dilepton azimuthal separation, and (d) electron isolation for the data with looser lepton transverse momenta requirements.

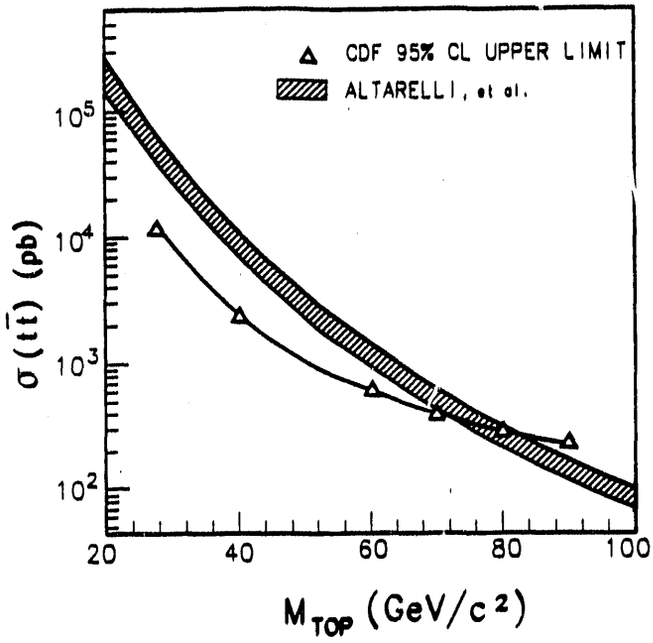

Fig. 66. The upper limit on the $t\bar{t}$ production cross section from the CDF $e\mu$ search. Also shown is the next to leading order calculation of the cross section.

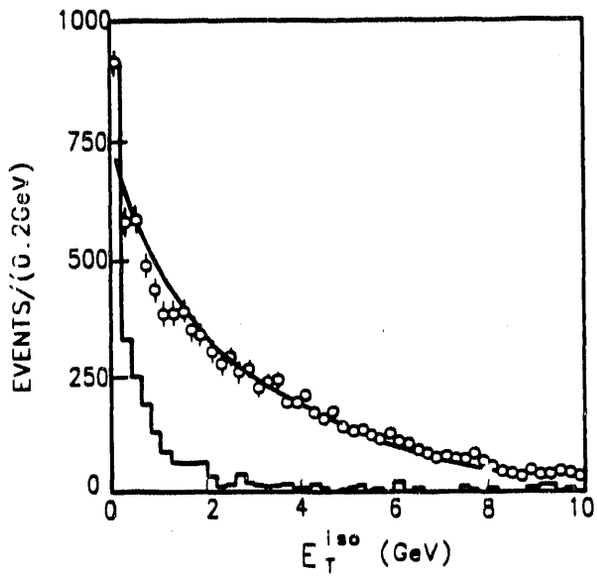

Fig. 67. Isolation for electrons with $E_T < 20$ GeV (circles), a sample that should be largely b decay. The solid curve is a $b\bar{b}$ Monte Carlo prediction, and the histogram is a 75 GeV/c^2 top prediction. The excess data in the first bin is due to residual W and Drell Yan events in the sample.

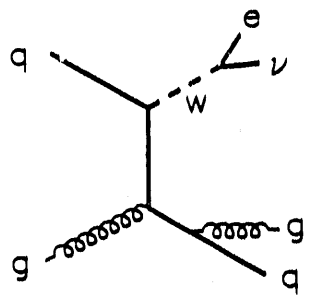

Fig. 68. Diagram producing W + 2 jets.

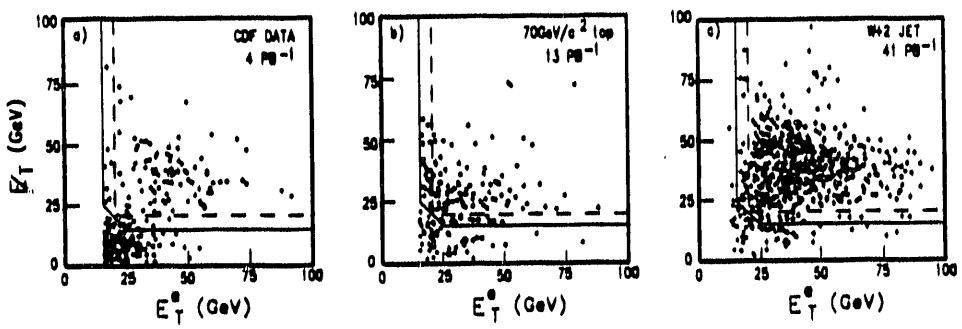

Fig. 69. Electron E_T versus missing E_T for (a) CDF $e + \geq 2$ jet sample, (b) 70 GeV/c^2 top Monte Carlo, and (c) W + 2 jet Monte Carlo. The solid (dashed) lines correspond to the loose (tight) cuts that are applied to the data. The trigger requirement, $E_T^e > 15$ GeV, has been applied.

background is due to the QCD production of W + jets (Fig. 68). This background cannot be removed by simple cuts because the event characteristics are so similar to that of a top quark signal. Rather a statistical method is employed to separate signal from background in the final sample.

The data in the $e + \geq 2$ jet sample are shown in Figure 69a. The concentration of events at low missing E_T and electron E_T near the trigger threshold is due to the $b\bar{b}$ background. The solid line in the figure represents a cut designed to remove most of this background. For very high top quark mass (> 65 GeV/c^2), a tighter cut (dashed lines) is used to further reduce background. Figure 69b and c show the expected distributions for a 70 GeV/c^2 top quark and the W + 2 jet background. The top signal is concentrated at lower E_T^e and missing E_T than the W background because the top quark decays to a virtual W when $M_{top} < M_W + M_b$. Thus the invariant mass of the final state $e\nu$ is less than the W mass, and the transverse momenta of the e and ν are smaller than they would be for the decay of an on-shell W. This translates into an $e\nu$ transverse mass distribution that is softer than for the W + jet background.

Figure 70a shows the data along with the expected shapes for signal and background. The data is consistent with pure background. This conclusion depends on an accurate

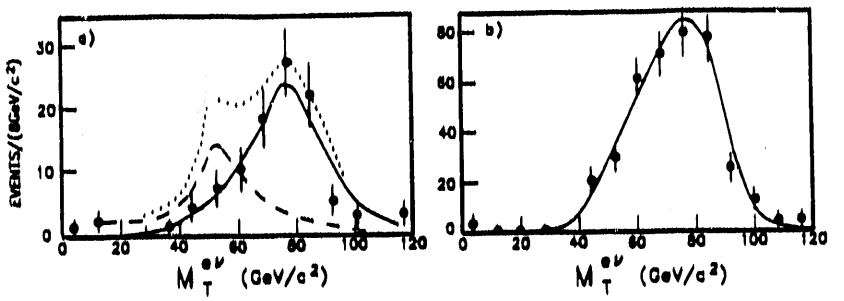

Fig. 70. (a) The CDF $e\nu$ transverse mass distribution for $e + \nu + \geq 2$ jet data. The solid curve is the Monte Carlo W + 2 jet shape. The expected distribution for a 70 GeV/c^2 top is shown by the dashed curve. The dotted curve is the sum of the other two curves. (b) CDF $e + \nu + 1$ jet data compared to the Monte Carlo expectation for QCD W + 1 jet production.

simulation of the background transverse mass distribution. The simulation can be checked with a similar data sample in which the top quark contribution would be very small. Such a sample, $e + \nu + 1$ jet, is shown in Figure 70b. The agreement between the data and the background simulation is excellent. The assumption that the $e + \nu + \geq 2$ jet data sample is entirely QCD W + jet background can be checked by looking at a number of other variables. Figure 71 shows the 2 jet invariant mass, the transverse momentum of the $e\nu$ system, and the azimuthal and rapidity separation between the two jets. In each case the agreement between the data and background simulation is excellent.

To obtain the top contribution for a given top mass, CDF fits the transverse mass spectrum to

$$\frac{dN}{dM_T^{e\nu}} = \alpha T(M_T^{e\nu}) + \beta W(M_T^{e\nu})$$

where $W(M_T^{e\nu})$ and $T(M_T^{e\nu})$ are the shapes of the W background and top signal transverse mass distributions respectively. W and T are normalized so that $\alpha = \beta = 1$ for the QCD predicted cross sections. The results of the fit are α and β along with their uncertainties. Table 5 gives these results for different assumptions for the top quark mass.

The data are consistent with the QCD W + jet prediction alone, which has an overall theoretical normalization uncertainty of 30 – 35%. The results of the fit are combined with the systematic uncertainties to obtain the upper limit on the $t\bar{t}$ production cross section. The major systematic sources are the detector jet energy scale and integrated luminosity, along with the effects of the underlying event, initial state gluon radiation, and top quark fragmentation. The 95% confidence level upper limit on the cross section is shown in Figure 72. At the 95% confidence level, the top quark mass must be $> 77\ GeV/c^2$.

4.4. Extended Dilepton Search

Although the $e\mu$ final state is the cleanest dilepton channel in which to search for the top quark, the ee and $\mu\mu$ channels also can be used. In extending the dilepton search,

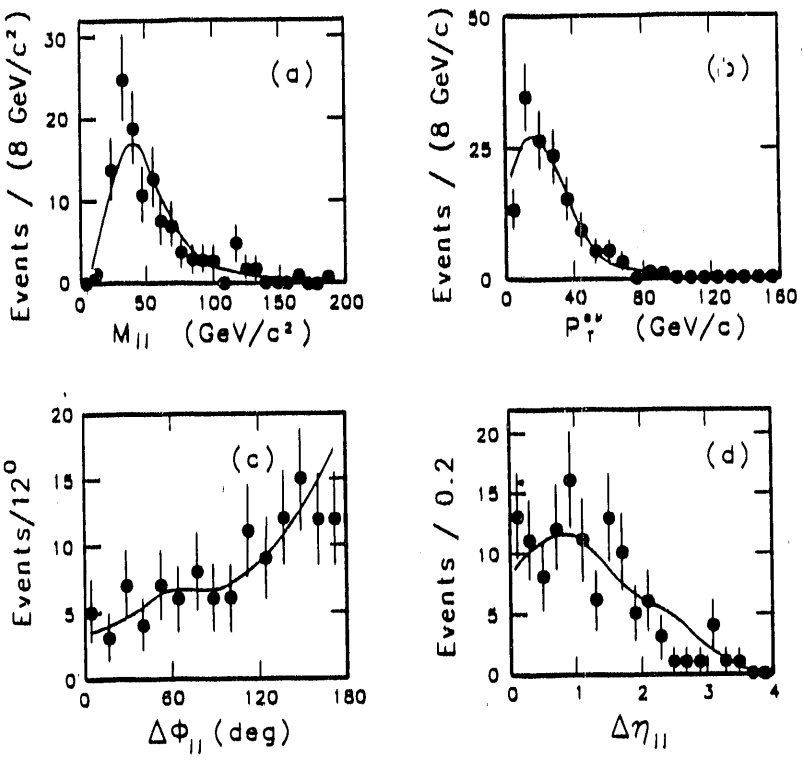

Fig. 71. The (a) dijet invariant mass, (b) P_T of the $e\nu$ system, (c) two jet azimuthal separation, and (d) two jet rapidity separation for CDF $e + \nu + \geq 2$ jet data. The curves are from a W + 2 jet Monte Carlo.

M_{top} $[GeV/c^2]$	α	β	χ^2 $(N_{df} = 10)$
40	0.07 ± 0.05	1.27 ± 0.14	9.7
50	0.06 ± 0.05	1.29 ± 0.14	10.4
60	0.11 ± 0.08	1.26 ± 0.15	10.4
70	$0.00^{+0.12}_{-0.00}$	1.28 ± 0.13	9.4
75	$0.00^{+0.18}_{-0.00}$	1.28 ± 0.13	9.4
80	$0.00^{+0.27}_{-0.00}$	1.28 ± 0.13	9.4

Table 5
Results of the transverse mass fits to the $e + \nu + \geq 2$ jet data along with the statistical fit uncertainties.

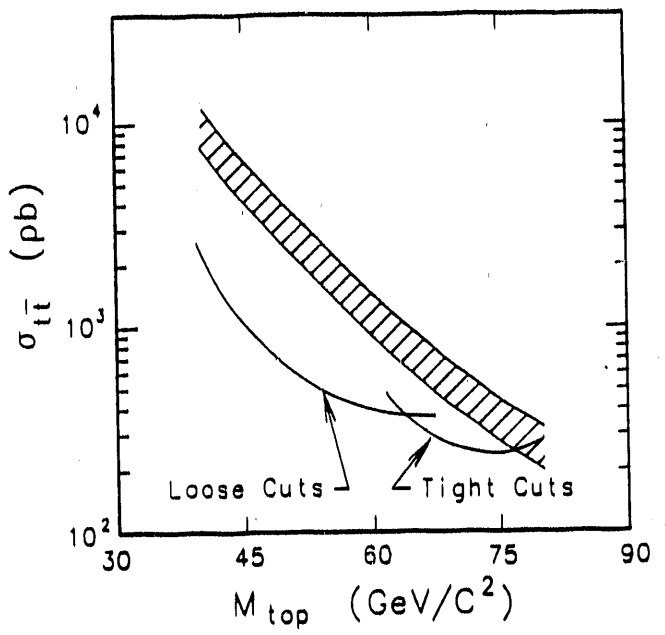

Fig. 72. The CDF upper limit on the top production cross section from the $e + \nu + \geq 2$ jet data sample, along with the next to leading order theoretical prediction.

we increase the acceptance for the $gg \rightarrow b\bar{b} \rightarrow l^+l^-$ and $Z \rightarrow \tau\tau \rightarrow l^+l^-$ backgrounds. More important, however, is a new major source of background, γ^* and $Z \rightarrow l^+l^-$. Much of the Z background can be removed by cutting out the dilepton invariant mass range $75 < M_{l^+l^-} < 105\ GeV/c^2$ (Fig. 73). In addition, we have to make use of the other discriminants mentioned earlier, missing E_T ($\not{E}_T$) and $\Delta\phi^{l^+l^-}$ (Fig. 74). The requirements are

$$\not{E}_T > 20\ GeV$$

$$20^\circ \leq \Delta\phi^{l^+l^-} \leq 160^\circ$$

As shown in Figure 75, there are no additional events in the signal region for the extended dilepton top search. The combined top mass limit from the dilepton searches, $e\mu$, ee, and $\mu\mu$, is $M_{top} > 84\ GeV/c^2$ at the 95% confidence level (Fig. 76).

4.5. Extended Single Lepton Search

The technique employed in the $e + \nu +$ jets search cannot be used for high mass top, since if $M_{top} > M_W + M_b$, the W from $t \rightarrow Wb$ is onshell. In this case, the $e\nu$ transverse mass distributions for signal and background are identical. Thus another discriminant is needed. CDF chose to look for a b quark in the event. Top events have two b quarks in each event ($\bar{t}t \rightarrow W\bar{b}Wb \rightarrow e\nu\bar{b}q\bar{q}b$ or $\mu\nu\bar{b}q\bar{q}b$), whereas the QCD produced W + jets background rarely contains b quarks. Here the b quark is tagged through its semileptonic decay into a muon; $b \rightarrow \mu\nu c$ occurs with a 10% branching ratio. The

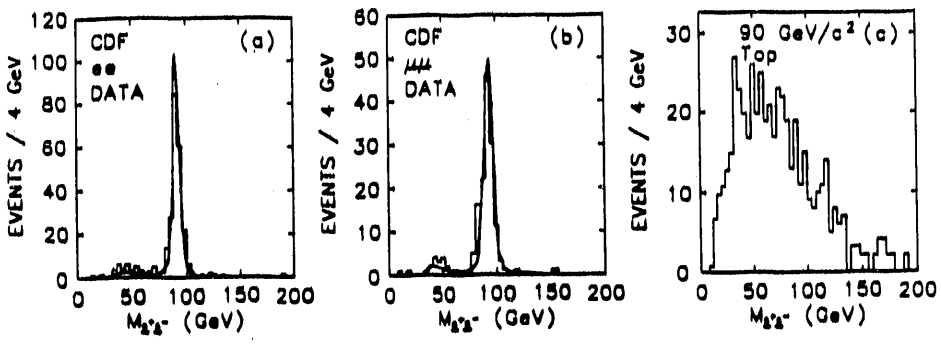

Fig. 73. Dilepton invariant mass for (a) CDF ee data, (b) $\mu\mu$ data, and (c) a 90 GeV/c^2 top simulation.

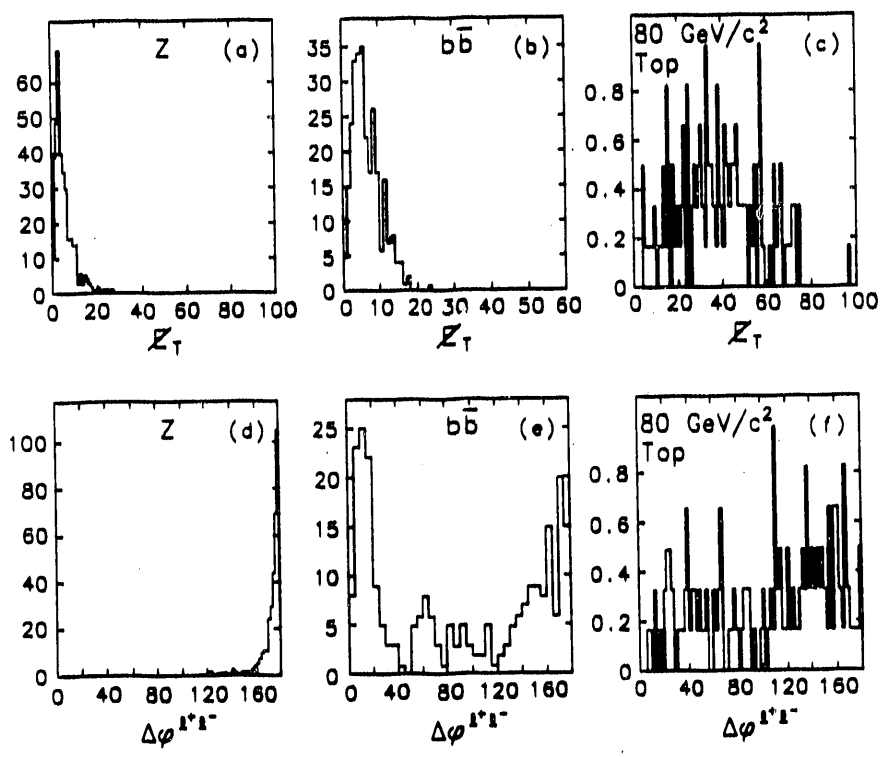

Fig. 74. The missing E_T distributions expected for (a) Z, (b) $b\bar{b}$, and (c) 80 GeV/c^2 top. The $\Delta\phi$ distributions from simulated samples of (d) Z, (e) $b\bar{b}$, and (f) 80 GeV/c^2 top.

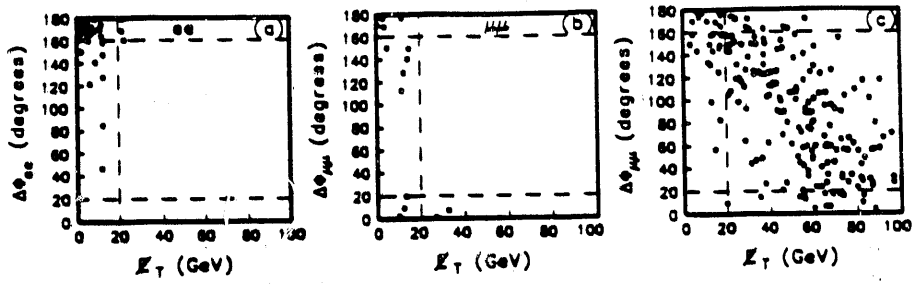

Fig. 75. The CDF (a) ee and (b) $\mu\mu$ data, and (c) simulated 90 GeV/c^2 top production. The dashed lines show the cuts applied to the data.

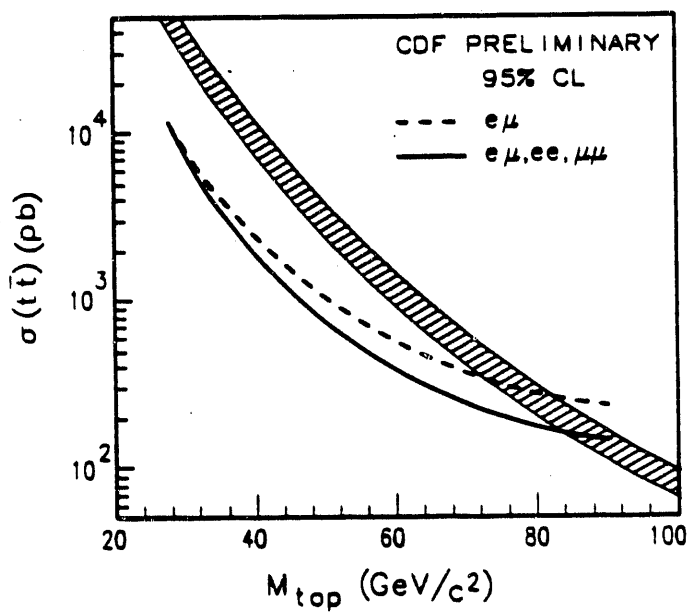

Fig. 76. The upper limits on the $t\bar{t}$ production cross section from the $e\mu$ (dashed) and combined dilepton (solid) searches along with the range of the theoretical prediction.

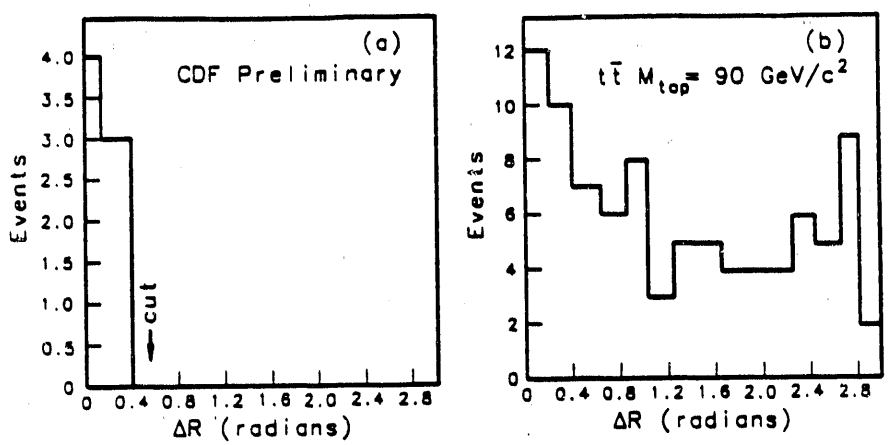

Fig. 77. The distance in $\eta - \phi$ space between a low energy muon candidate and the closest of the two high P_T jets in (a) the e or $\mu + \nu +$ jets data sample, (b) a 90 GeV/c^2 $t\bar{t}$ Monte Carlo sample.

single high P_T lepton sample (e or μ) was searched for the presence of an additional muon with $P_T < 15$ GeV/c. The upper limit on P_T^μ was placed both because muons from b typically have low energy and to avoid double counting with the dilepton $e\mu$ and $\mu\mu$ searches. A low P_T muon candidate also had to be outside the cones of radius 0.6 (in $\eta - \phi$ space) centered on the two leading jets. In top decay, these jets would be from the hadronic decay of a W; the b quarks are not usually near these jets. This cut has the advantage of greatly reducing fake muon candidates. Hadrons can fake muons either by penetrating the absorber iron or by decay in flight before entering the iron. The large hadron multiplicity in jets make the fake muon rate near a jet core rather large.

Figure 77 shows the distance between the low energy muon in an event and the nearest of the two high P_T jets. There are no events with $R > 0.6$. The CDF top mass limit from the combined extended dilepton and extended single lepton searches is (Fig. 78)

$$M_{top} > 91\ GeV/c^2 \qquad @\ 95\%\ CL$$

4.6. Top Searches at the $Sp\bar{p}S$ Collider

UA1 searched for the top quark in a number of channels [49]. For the $\mu + \nu +$ jets final state, they created a likelihood function to distinguish a top signal from the QCD W background. Four variables were included: muon isolation, muon P_T, missing E_T, and the azimuthal separation between the muon and the highest E_T jet. Figure 79 shows the log likelihood distribution for the data along with simulations of the background and a 50 GeV/c^2 top quark. From this sample, they found that $M_{top} > 52$ GeV/c^2 at the 95% confidence level.

UA1 also used a likelihood function for their dimuon search, with variables P_T^μ, muon isolation, and the azimuthal separation between the two muons. They found

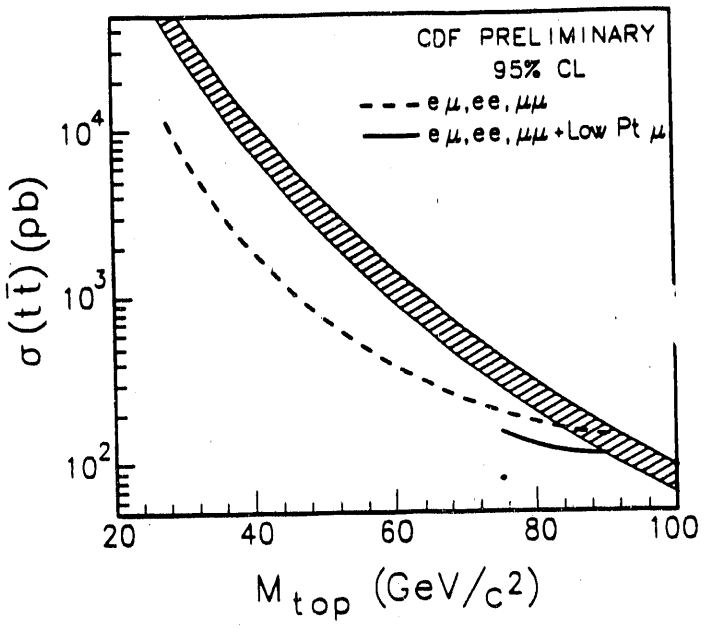

Fig. 78. The CDF upper limit on the $t\bar{t}$ production cross section from the combined searches.

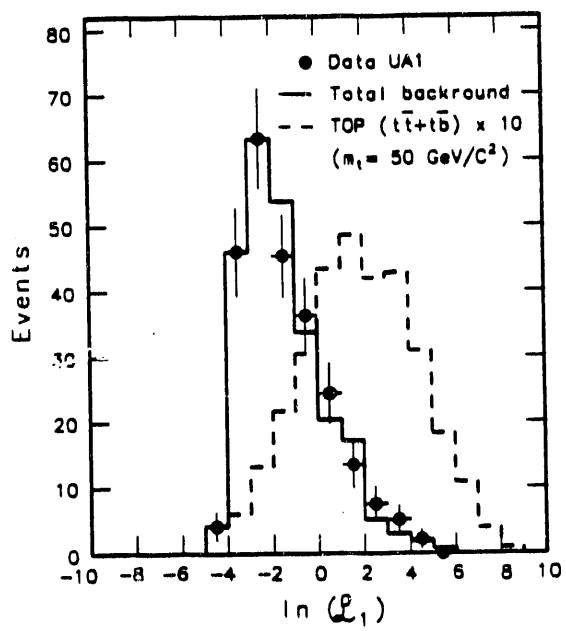

Fig. 79. The log likelihood distribution for UA1 $\mu + \nu +$ jets data compared with simulated background and a 50 GeV/c^2 top quark.

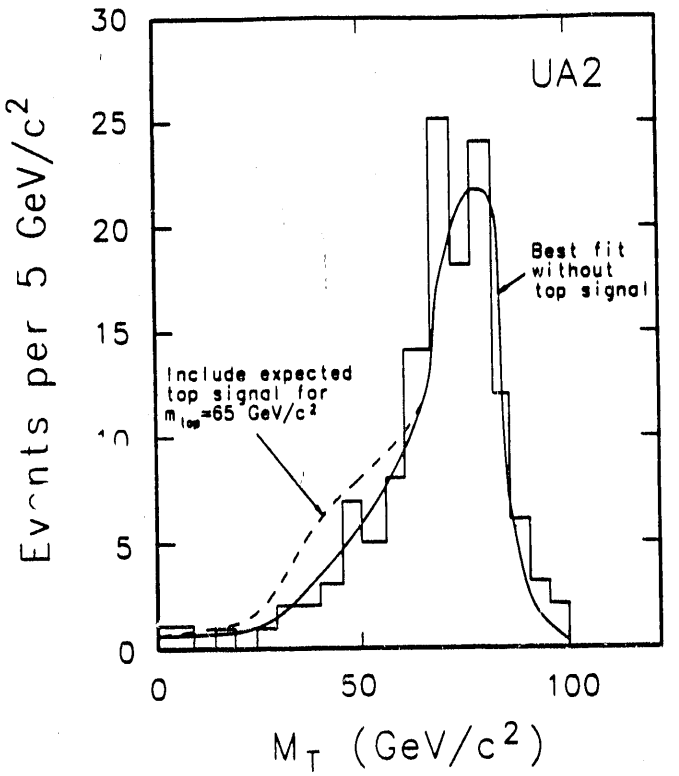

Fig. 80. UA2 $e\nu$ transverse mass distribution for events containing at least one jet. The solid line is the fit to the QCD W background shape, while the dashed line includes the signal expected from a 65 GeV/c^2 top quark.

$M_{top} > 46\ GeV/c^2$ at the 95% confidence level in this channel. When they combined these searches and their earlier work, they set an overall limit $M_{top} > 60\ GeV/c^2$ at the 95% confidence level.

UA2 performed a search with their sample of events containing an electron, missing E_T, and at least one jet with $E_T > 10\ GeV$ [50]. They fit the $e\nu$ transverse mass distribution to a sum of QCD W + jet and top contributions (Fig. 80). The resulting limit from UA2 is $M_{top} > 69\ GeV/c^2$ at the 95% confidence level.

5. b Physics at Hadron Colliders

Heavy flavors provide a window on many important physics issues. The production process, $p\bar{p} \rightarrow b\bar{b}X$, is a testbed for QCD calculations since higher order diagrams make a large contribution here and there are a large number of scales in the problem [51]

$$\sqrt{s} \gg P_T \gg M_b \gg \Lambda_{QCD}$$

Moreover, the future of electroweak studies using the b system depends on the value of the total cross section (how many b quarks can be produced) and the differential

cross sections (how efficiently can the second b in an event be tagged). With sufficient numbers of b quarks, significant electroweak studies can be carried out. These include $B\overline{B}$ mixing and rare B decays to obtain information about CKM matrix elements, the search for forbidden decays to investigate extensions to the Standard Model, and hopefully CP violation in B decay where CP asymmetries may be large.

5.1. b Production

For b production via leading order QCD diagrams (Fig. 81a,b,c), the b and $\overline{b}$ have equal and opposite transverse momenta. Valence $q\overline{q}$ annihilation (Fig. 81c) dominates when $2M/\sqrt{s} \gtrsim 0.1$. At Fermilab Collider energies, this condition is satisfied for heavy top quark production but not for b production. When $2M_b/\sqrt{s} \ll 1$ (it is ~ 0.005 at Fermilab), the two-gluon initial state dominates, and higher order diagrams (Fig. 81d,e) can give a larger contribution than the leading order diagrams. This is due to the large gluon density at small x, the increased color factor at a 3-gluon vertex, and the cross section enhancement for diagrams containing t-channel vector exchange.

The dominant higher order diagrams are gluon splitting (Fig. 81d) and flavor excitation (Fig. 81e), which essentially is initial state gluon splitting. Understanding these higher order production mechanisms is important for at least two reasons. First there is the theoretical interest in understanding higher order QCD processes. Figure 82 shows the dependence of the cross section on the renormalization scale [52]. Note that contrary to the usual expectation for well behaved perturbation expansions, the dependence is stronger when the next to leading order diagrams are included. This may be due to the large next to leading order contribution and the resulting need to include yet higher order diagrams in the calculation. Second, there is the implication for flavor tagging the second b in $b\overline{b}$ events, since the P_T and rapidity correlations between the b and $\overline{b}$ are quite different in the leading order and the various next to leading order diagrams. The prospect for measuring $B\overline{B}$ mixing and studying CP violation at hadron colliders thus depends on understanding the b production mechanisms.

The major experimental challenge in doing b physics is separating b events from the

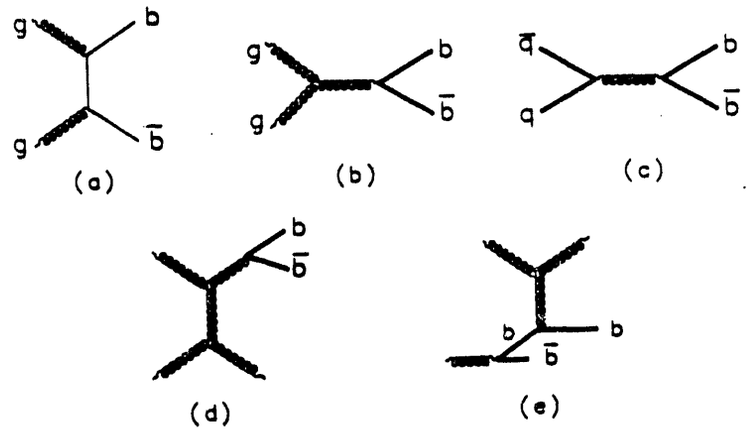

Fig. 81. (a,b,c) Leading order b production diagrams. (d,e) Next to leading order diagrams.

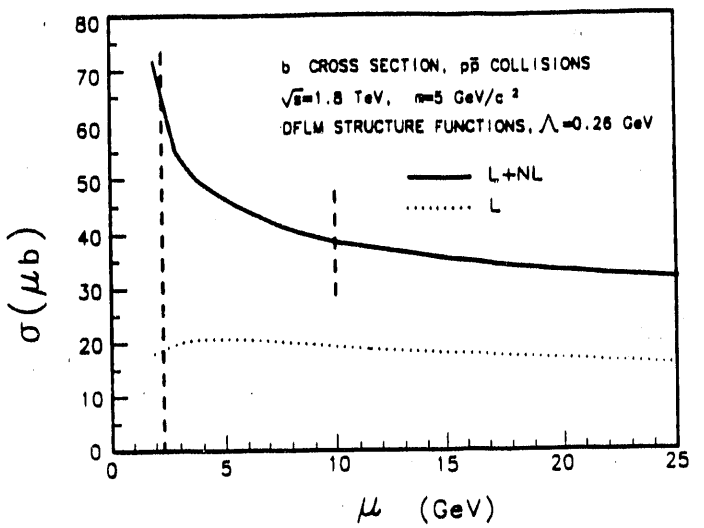

Fig. 82. The dependence of the calculated b production cross section on the renormalization scale for leading order (dashed curve) and leading plus next to leading order (solid curve) diagrams.

much more copious light quark background. Since the largest b branching ratio into final states without a neutrino is only a few percent, most of the studies so far have concentrated on inclusive final states. We will first consider inclusive lepton samples where the major challenges are separating moderate P_T electrons and muons from misidentified hadrons, and determining the charm, W, Z, and γ^* contributions to the data samples. Then we will look at the analyses of data samples containing $J/\psi \rightarrow \mu^+\mu^-$ where b production must be separated from other sources of J/ψ such as $\chi \rightarrow J/\psi + \gamma$. Finally, we will consider the recent reconstruction of exclusive final states in b decay.

5.1.1. Inclusive Lepton Channels

The study of b production at hadron colliders was initially carried out by the UA1 collaboration [53]. Their primary b physics data is the inclusive muon sample, chosen because the thick UA1 hadron absorber allows muon detection in and near hadron jets. Unfortunately π and K decay in the jets produces a large background. Of their 20,000 events with $P_T^\mu > 6$ GeV/c, approximately 70% are background. This fraction drops to 35% for $P_T^\mu > 10$ GeV/c. A UA1 focus is the $10 < P_T^\mu < 15$ GeV/c range where the decay background is manageable and the contribution from resonances (W, Z, γ^*, J/ψ, Υ) is small ($\sim 6\%$). To separate $b\bar{b}$ from $c\bar{c}$, they define the variable $P_T^{rel} \equiv P^\mu sin\theta_{rel}$ where θ_{rel} is the angle between the muon and the nearest jet. The larger b mass results in a larger P_T^{rel}. Figure 83 shows the UA1 data fit to a sum of $b\bar{b}$, $c\bar{c}$, and π/K decay contributions [54]. The UA1 result on the fraction of $b\bar{b}$ is

$$\frac{N_{b\bar{b}}}{N_{b\bar{b}} + N_{c\bar{c}}} = 0.76 \pm 0.12$$

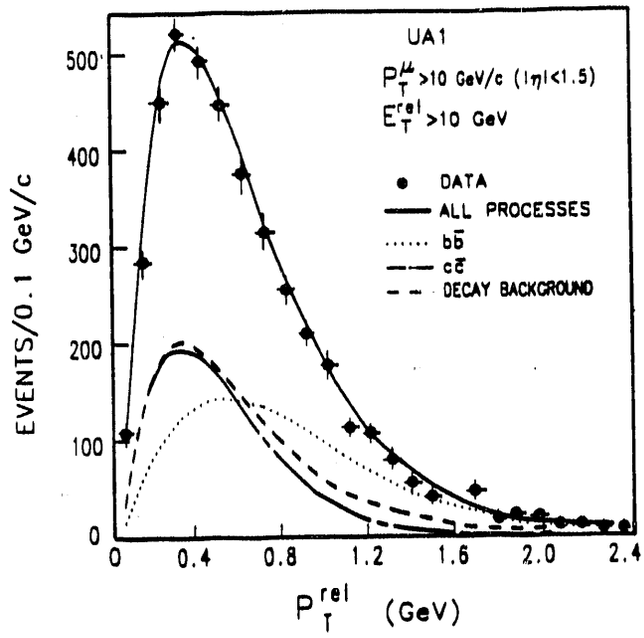

Fig. 83. P_T^{rel} for the UA1 single muon data sample. The solid line is the sum of $b\bar{b}$, $c\bar{c}$, and decay background contributions.

in agreement with predictions.

A Monte Carlo simulation is used to convert the measured muon differential cross section, $d\sigma/dP_T^{\mu}$, into the b quark production cross section, $d\sigma/dP_T^{b}$. The simulation uses b jet fragmentation, semileptonic B branching ratios, and B decay kinematics as measured in e^+e^- collisions. Figure 84 shows the relationship between the observed muon P_T and the parent b P_T . The resulting b cross section, integrated over the central three units of rapidity and over P_T above the P_T^{min} plotted, is shown in Figure 85. The results agree well with the next to leading order QCD calculation.

CDF used its electron data sample to study b production [55]. The advantage is relatively low background; misidentified electrons and unidentified gamma conversions constitute $\sim$ 30% for P_T^e > 7 GeV/c. The disadvantage in using electrons is the difficulty in identifying electrons within jets. However this mostly affects the charm contribution rather than the b signal. CDF selects its electron sample with P_T > 7 GeV/c based on the transverse and longitudinal shower shape, the agreement between the track momentum and the calorimeter energy, and position matching of the extrapolated track and cluster centroid. In addition, identified gamma conversions are removed. Figure 86 shows the electron P_T spectrum. The shoulder above 25 GeV/c is due to W and Z decay. W bosons are easily removed by requiring that there be small missing E_T in the event; events are removed as Z contamination if the electron and another high P_T track have an invariant mass near M_Z. The electron spectrum after W and Z removal is shown in Figure 87. The shape agrees well with that predicted by ISAJET plus the CDF detector simulation. Note that charm is expected to contribute

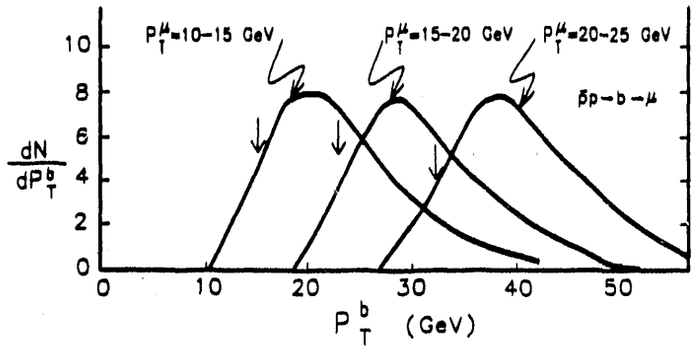

Fig. 84. The b quark spectrum for different bins of muon P_T, as predicted by the UA1 Monte Carlo.

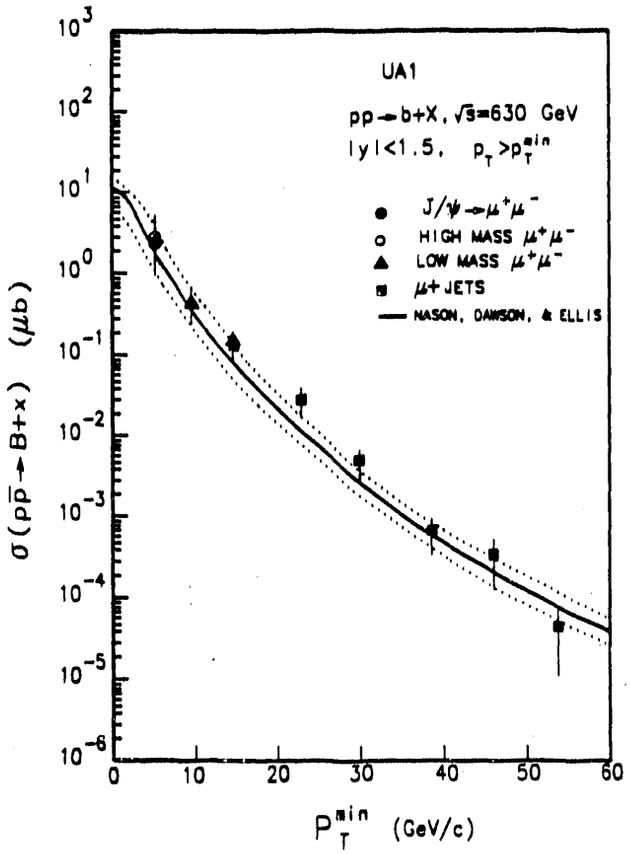

Fig. 85. The UA1 b quark production cross section integrated over $|y| < 1.5$ and $P_T > P_T^{min}$. The data points come from the single muon analysis as well as dimuon analyses. The curves show the range of the next to leading order calculation.

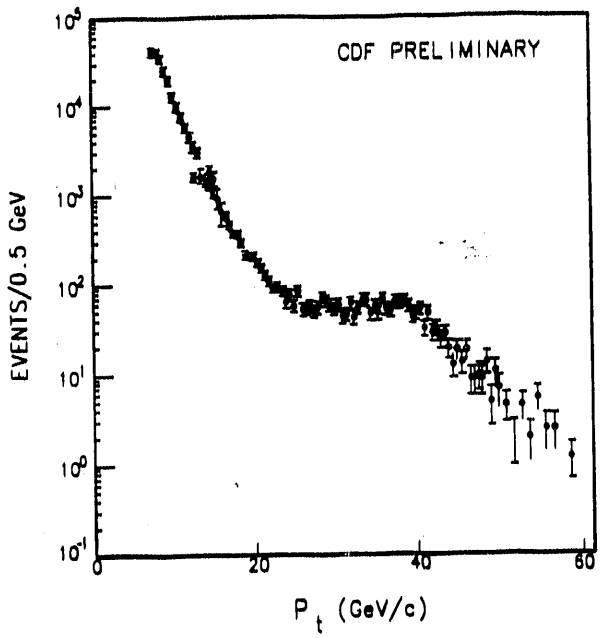

Fig. 86. The CDF electron P_T spectrum.

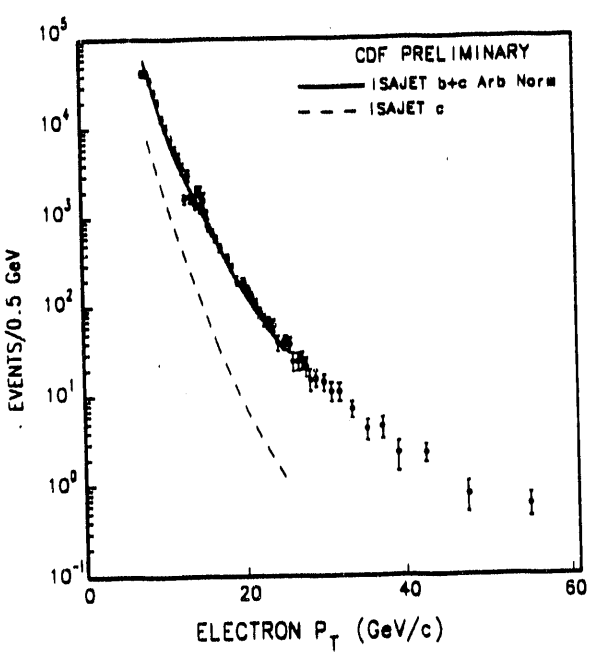

Fig. 87. The CDF electron P_T spectrum after removing W and Z events. The curves show the predicted shape for c and $b + c$ production.

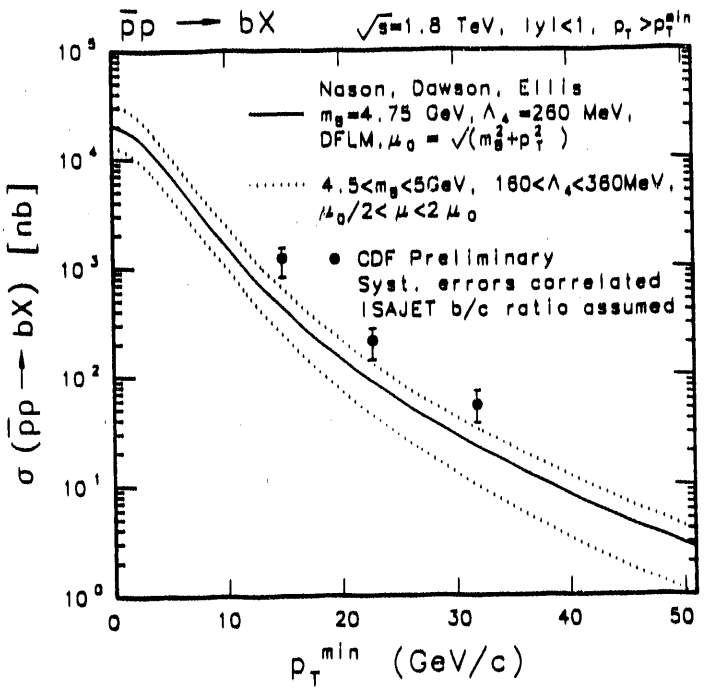

Fig. 88. The CDF b production cross section integrated over $|y| < 1$ and $P_T^b > P_T^{min}$.

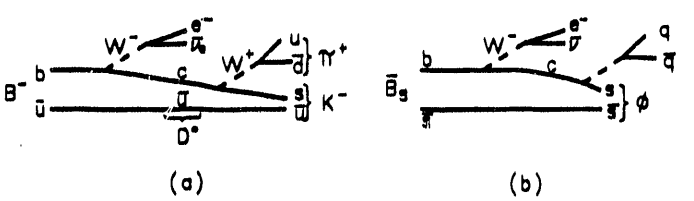

Fig. 89. The decay diagram for (a) $B^- \to D^0 e^- \overline{\nu} \to K^- \pi^+ e^- \overline{\nu}$, (b) $\overline{B}_s \to e^- \overline{\nu} \phi X$.

3-15% depending on the electron P_T .

As for UA1, the relation between the P_T^e and P_T^b spectra is obtained from a Monte Carlo study that incorporates the results from e^+e^- colliders. The CDF cross section is shown in Figure 88. The data lie somewhat above the upper end of the theoretical prediction.

Independent evidence that these inclusive lepton events are indeed from b decay comes from CDF [56]. Their high resolution tracking chamber allows them to search for resonances near the electron. Since B meson semileptonic decay usually produces a D meson in the final state, identifying a D near the electron would confirm that the electron was produced by B decay. Figure 89a shows the B decay diagram. Note that the K and the e have the same sign electric charge. CDF looked for $D \to K\pi$ in a cone (R=1.0) around the electron. Figure 90 shows the D^0 peak when the e and K have

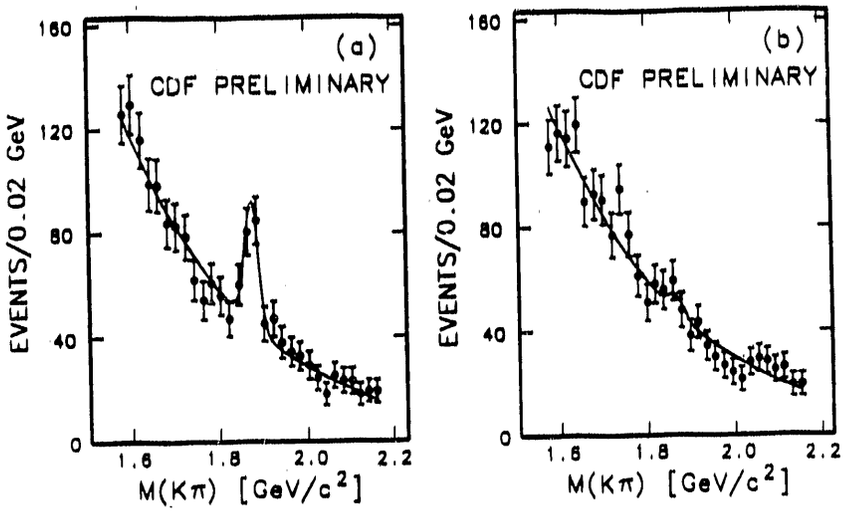

Fig. 90. The CDF $K\pi$ invariant mass when (a) the K and e have the same sign charge, (b) when the K and e have opposite sign charge.

the same sign, but no peak when they have the opposite sign. The number of events expected in the D^0 peak is 67 ± 20; 75 ± 17 are observed. Figure 91 shows that, for events in the D^0 peak, the $eK\pi$ invariant mass does not exceed M_B, as required if these are decay products of a single B meson.

CDF also looked for the charge correlation between the electron and a K from the decay of a K^*. The quark decay chain $b \to c \to s$ translates into the meson decay chain $\overline{B} \to e^- DX \to e^- \overline{K^*} X \to e^- K^- \pi^+ X$. Thus the electron and kaon must have the same sign charge. This is to be contrasted with an electron from $c\bar{c}$ production and decay, $c\bar{c} \to q\bar{q}se^-\bar{\nu}\bar{s}$. Here the s and $\bar{s}$ have equal probability to fragment into a K^*. Thus one would expect approximately equal numbers of same and opposite sign eK pairs. Figure 92 shows the $K\pi$ invariant mass spectrum for the same sign and opposite sign eK events. As expected for a data sample that is rich in b quarks, a K^* peak of the correct magnitude is seen in the same sign sample, but no peak appears in the opposite sign sample.

One last check comes from looking for $\phi \to KK$ near the electrons (Fig. 89b). Obviously there is no charge correlation to look for, but we can compare the rate of ϕ mesons observed in the inclusive electron sample and a control sample, electrons from identified photon conversions (Fig. 93). A mass peak at the ϕ mass is seen in the inclusive electron sample, while it is not observed in the control sample. These tests all give confidence that the inclusive electron data sample indeed is largely from b decay.

5.1.2. Inclusive J/ψ Channels

B decay into inclusive J/ψ mesons, $b \to cW^* \to c\bar{c}s \to J/\psi X$, with the J/ψ detected in the $\mu^+\mu^-$ mode suffers from a very small combined branching ratio

$$BR(B \to J/\psi X) \times BR(J/\psi \to \mu^+\mu^-) = 0.011 \times 0.069 = 8 \times 10^{-4}$$

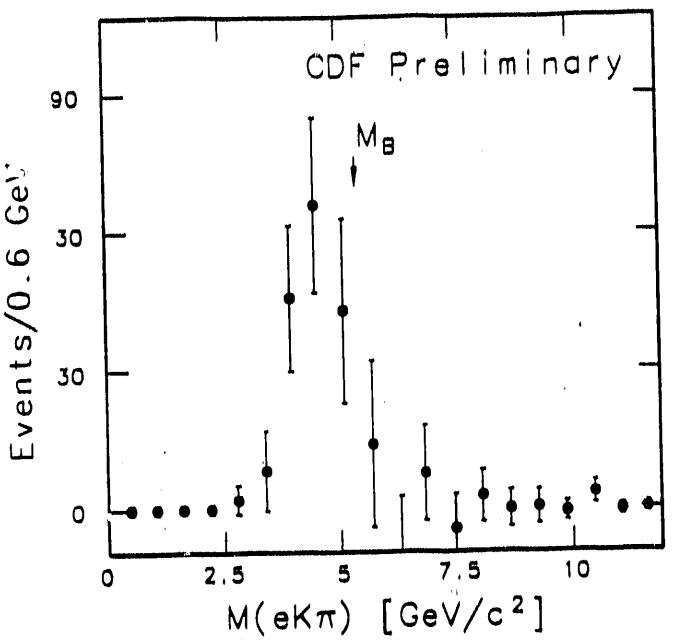

Fig. 91. The CDF $eK\pi$ invariant mass.

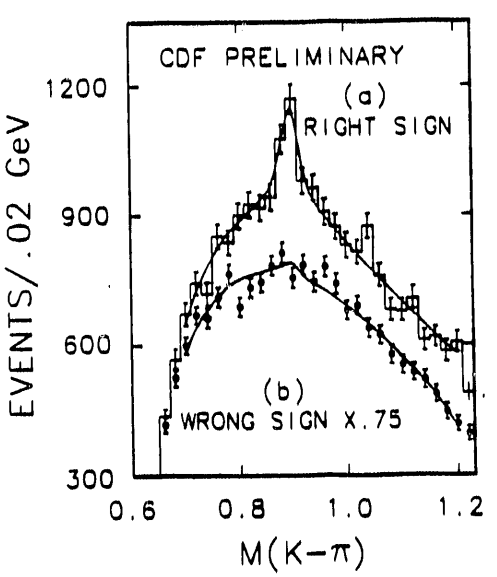

Fig. 92. The CDF invariant mass spectrum for $K\pi$ pairs found near an electron in events in which the e and K have (a) the same sign charge, (b) the opposite sign charge.

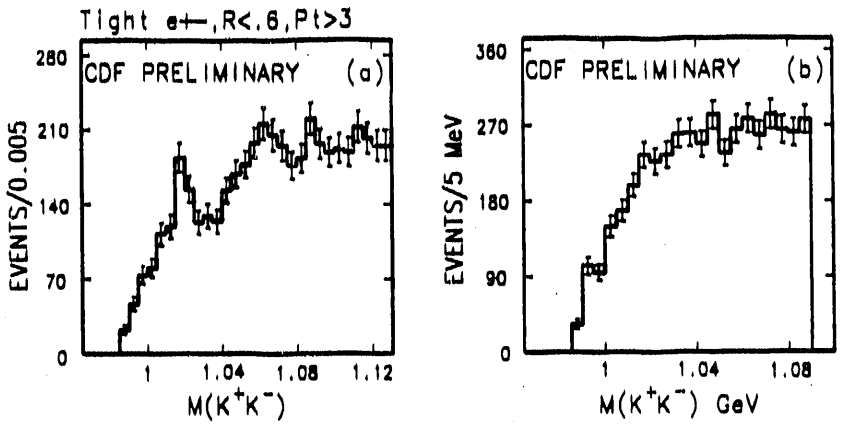

Fig. 93. The CDF invariant mass spectrum for K^+K^- pairs found (a) near electrons and (b) near electrons in a photon conversion sample.

To compensate, there are two advantages to this mode. Dimuon detection provides a very clean J/ψ signal with little background. In addition we shall see that the majority of J/ψ mesons come from B decay. The only other significant source of J/ψ is radiative decay of QCD produced χ_c. A χ_c can be produced from the annihilation of two gluons; at least three gluons must annihilate in order to directly produce a J/ψ.

The CDF J/ψ trigger requires two muons each with $P_T > 3$ GeV/c. The dimuon mass spectrum for this data set shows a J/ψ peak with very little background (Fig. 94) [57]. The fraction of J/ψ coming from either B or χ_c decay is determined independently from inclusive J/ψ production and from exclusive final states. For the inclusive analysis, the fraction of J/ψ that comes from B decay ($\equiv F$) can be determined in a relatively unbiased way from the ratio of the inclusive J/ψ cross section to the inclusive ψ' cross section. It is assumed in this analysis that ψ' is produced entirely from B decay, since χ_c cannot decay into ψ'. Figure 95 shows the ψ' signal. There are 72 ± 17 events in the peak. This gives for the ratio of the ψ' to J/ψ production cross sections

$$\frac{\sigma(\psi')}{\sigma(J/\psi)} = (4.2 \pm 1.0) \times 10^{-2}$$

When compared with the ratio of the $B \to \psi'$ to $B \to J/\psi$ branching ratios measured by CLEO [58], $(6.8 \pm 2.5) \times 10^{-2}$, the CDF result translates into

$$F = 64\% \pm 15\% \text{ (CDF stat)} \pm 5\% \text{ (syst)} \pm 23\% \text{ (CLEO stat)}$$

for the fraction of J/ψ coming from B decay. The largest uncertainty is from the CLEO statistics on the ψ' branching ratio; the second largest is due to the CDF ψ' statistics. Both of these should greatly improve in the next year or two.

5.1.9. Exclusive Final States

CDF has also studied J/ψ production by reconstructing exclusive χ_c and B final states. To find the former, $\chi_c \to J/\psi + \gamma$, CDF looks for isolated electromagnetic clusters of $E_T > 1$ GeV with a transverse shower shape consistent with that of a photon [59].

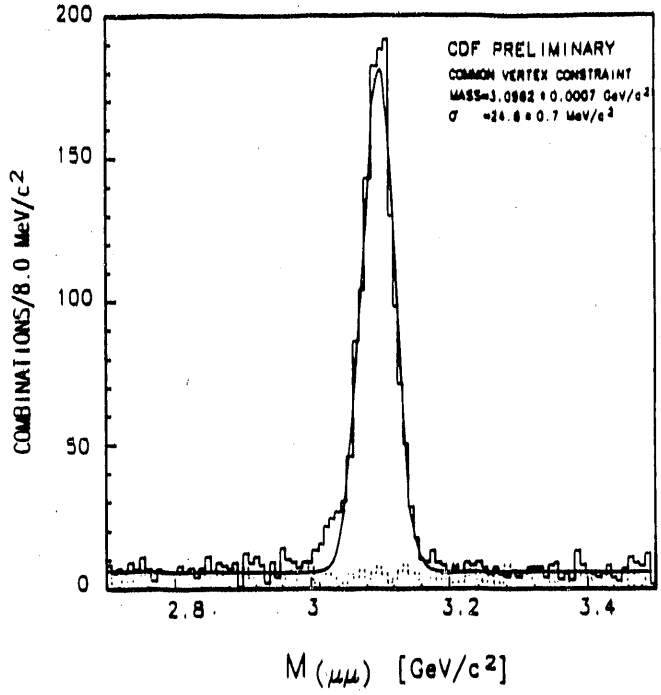

Fig. 94. The CDF dimuon invariant mass distribution in the J/ψ region. The dotted histogram is the same sign dimuon data.

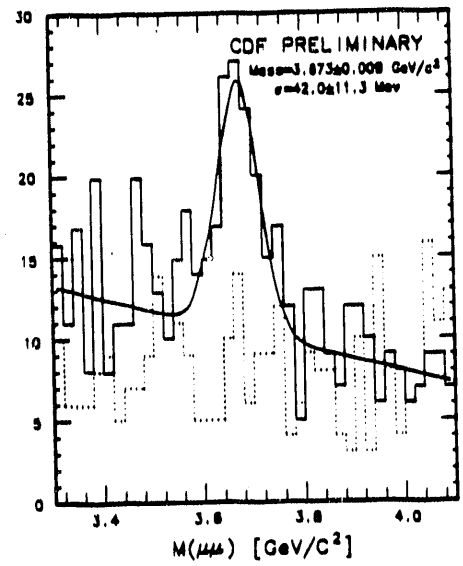

Fig. 95. The CDF ψ' signal. The dotted histogram is the same sign data.

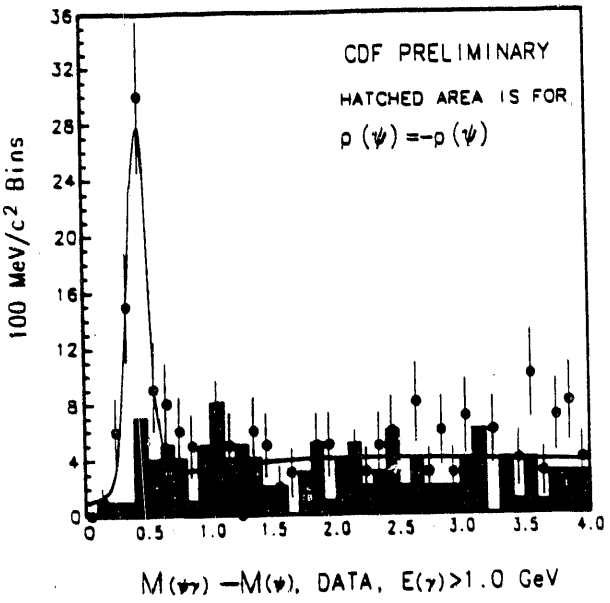

Fig. 96. The CDF $J/\psi\gamma$, J/ψ invariant mass difference. The uncorrelated background is estimated by reanalyzing the events with the J/ψ momentum direction reversed.

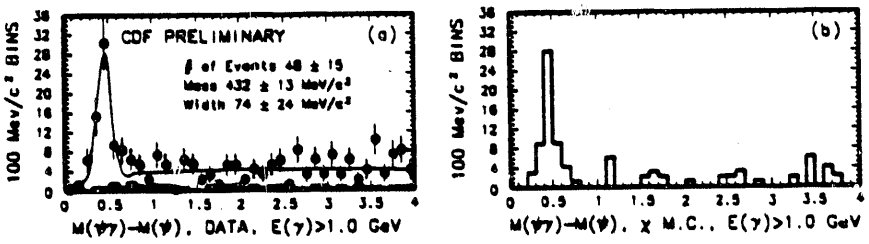

Fig. 97. (a) The CDF $J/\psi\gamma$, J/ψ invariant mass difference. The solid curve is a fit to a resonance plus smooth background, and the solid histogram is the data from the J/ψ sidebands. (b) A Monte Carlo simulation of a signal from χ_1 and χ_2 production.

The best resolution for the $J/\psi\gamma$ resonance is obtained by plotting the difference between the $J/\psi\gamma$ and J/ψ invariant masses (Fig. 96). In this figure, the uncorrelated background is estimated by reanalyzing the event sample after reversing the direction of each J/ψ. The background not associated with J/ψ production can be estimated using the $\mu^+\mu^-$ mass sidebands above and below the J/ψ. Figure 97 shows the data and the sideband background, as well as a Monte Carlo simulation of the signal for the appropriate mixture of χ_1 and χ_2. The peak in the data clearly is due to reconstructed $\chi_c \to J/\psi + \gamma$. From the number of observed events, CDF concludes that $\sim 30\%$ of J/ψ comes from χ_c decay.

Exclusive reconstruction of B mesons is carried out for two modes [60]

$$B_d^0 \to J/\psi K^{*0} \to J/\psi K\pi$$

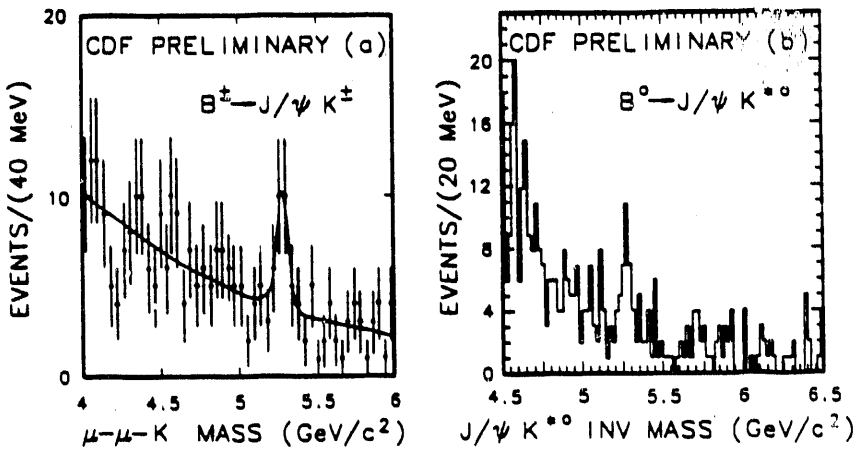

Fig. 98. (a) $B^{\pm} \to J/\psi K^{\pm}$ (b) $B^0 \to J/\psi K^{*0}$ from CDF.

$B_u^{\pm} \to J/\psi K^{\pm}$

CDF looks in a 60^0 cone around the J/ψ direction for additional tracks. For the B_u search, all tracks with $P_T > 2.5$ GeV/c are considered K candidates. For the B_d, all opposite sign track pairs from among the three highest P_T tracks are tried; a pair is used if the $K\pi$ invariant mass is within 50 MeV/c^2 of the K^{*0} mass. Figure 98 shows the individual mass spectra; the combined spectrum is in Figure 99. Until there is more data on final state polarization in $B \to J/\psi K^*$ decay (it affects the detection efficiency calculation), only $B \to J/\psi K^{\pm}$ is used to determine the B production cross section. CDF finds that $\sim 70\%$ of J/ψ comes from B, consistent with the value for F obtained in the inclusive J/ψ study. The B cross section is shown in Figure 100. As with the data points from the inclusive electron sample, the data is somewhat higher than the next to leading order theoretical prediction.

5.2. $B^0 \to \mu^+\mu^-$

$B_{d,s}^0 \to \mu^+\mu^-$ is a flavor changing neutral decay allowed by the Standard Model via higher order electroweak diagrams (Fig. 101). The theoretical expectations are

$$BR(B_d^0 \to \mu^+\mu^-) \approx 10^{-11}$$
$$BR(B_s^0 \to \mu^+\mu^-) \approx \text{few} \times 10^{-9}$$

The best published limit comes from CLEO and ARGUS [61]

$$BR(B_d^0 \to \mu^+\mu^-) < 0.5 \times 10^{-4} \text{ @ } 90\% \, CL$$

UA1 has a preliminary result [62]

$$BR(B_{d,s}^0 \to \mu^+\mu^-) < 1.0 \times 10^{-5}$$

The CDF dimuon spectrum is shown in Figure 102 along with the ψ' peak. Given the 72 observed ψ' events and the combined $B \to \psi' X \to \mu\mu X$ branching ratio of

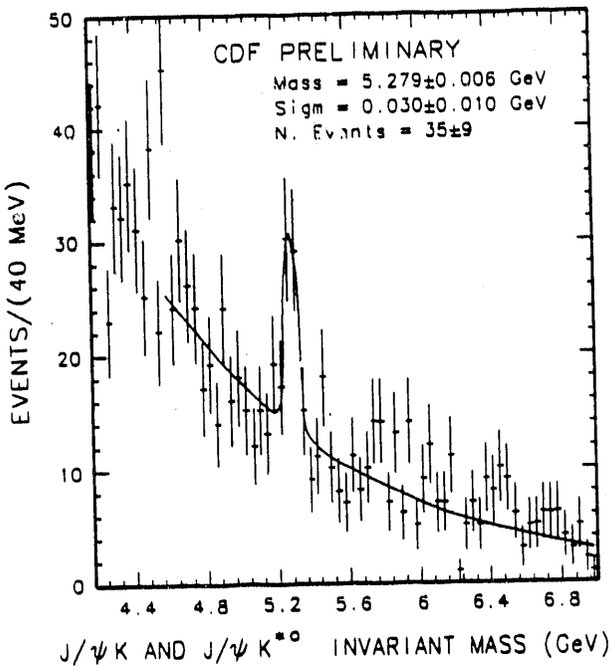

Fig. 99. The combined CDF $J/\psi K$ and $J/\psi K^*$ spectrum.

2.8×10^{-5}, the lack of a peak in the B region translates into a branching ratio limit of [63]

$$BR(B_d^0 \to \mu^+\mu^-) < 3.2 \times 10^{-6} \text{ @ } 90\% \, CL$$

The limit would be much better if it weren't for the size of the background in the B region. With the silicon vertex detector in the next CDF run, the background should be greatly reduced since candidate tracks can be required to point to a secondary vertex.

5.3. $B^0, \overline{B}^0$ Mixing

As is the case in $K^0, \overline{K}^0$ mixing, the transformation of a b quark into a $\bar{b}$ is a second order weak process (Fig. 103). The diagrams with t quark exchange dominate, and thus the difference between $B_d, \overline{B}_d$ mixing and $B_s, \overline{B}_s$ mixing comes from the CKM factors, V_{td}^2 and V_{ts}^2. Since V_{ts} is considerably larger than V_{td}, $B_s, \overline{B}_s$ mixing should be significantly larger than $B_d, \overline{B}_d$ mixing.

Mixing is characterized by

$$\chi \equiv \frac{\text{Prob}(B^0 \to \overline{B}^0)}{\text{Prob}(B^0 \to B^0) + \text{Prob}(B^0 \to \overline{B}^0)}$$

where the physical range is $0 \leq \chi_{d,s} \leq \frac{1}{2}$ (Fig. 104). The first evidence for $B\overline{B}$ mixing came from UA1 [64]. However in high energy $\overline{p}p$ colliders, both B_d^0 and B_s^0 are

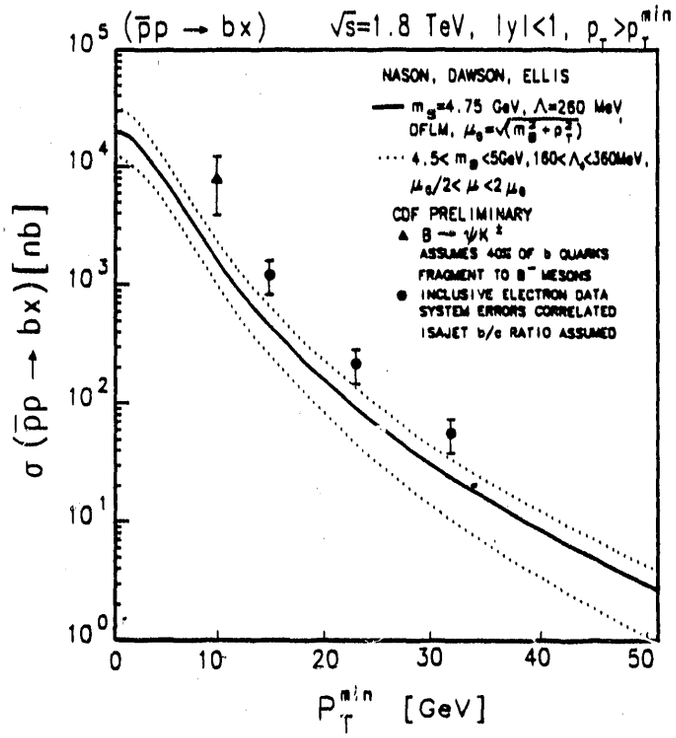

Fig. 100. The CDF B production cross section results from both the inclusive electron and exclusive $B \to J/\psi K^{\pm}$ analyses.

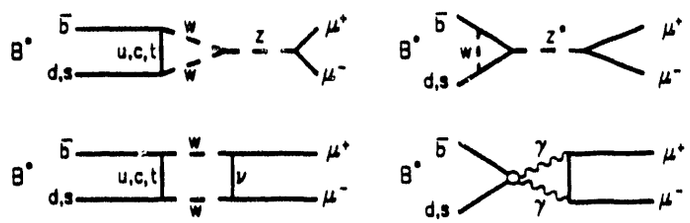

Fig. 101. Diagrams for $B^0 \to \mu^+\mu^-$ production.

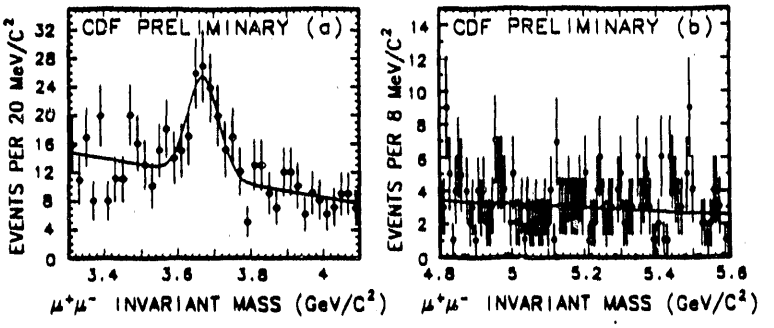

Fig. 102. The CDF dimuon invariant mass spectrum (a) near the ψ', (b) in the B mass region.

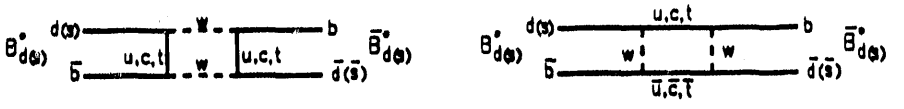

Fig. 103. $B^0, \overline{B}^0$ mixing diagrams.

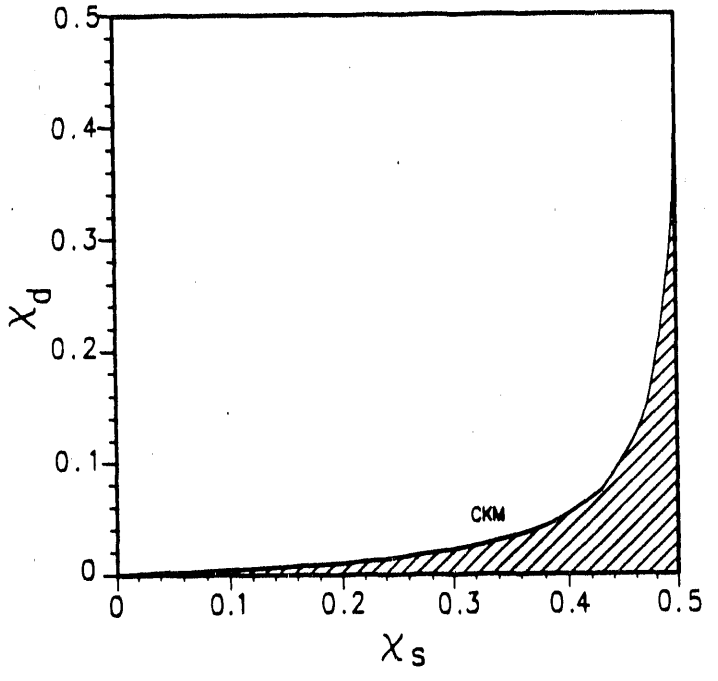

Fig. 104. The shaded region is allowed by the CKM matrix when the non-mixing experimental results and 3-generation unitarity are used.

produced. What is actually measured is the combined mixing, characterized by

$$\overline{\chi} \equiv \frac{\text{Prob}(b \to \overline{B}^0 \to B^0 \to l^+)}{\text{Prob}(b \to l^\pm)} = f_d\chi_d + f_s\chi_s$$

where f_d (f_s) is the fraction of B_d^0 (B_s^0) produced relative to all b mesons and baryons times $BR(B_{d,s}^0 \to lX)/BR(b \to lX)$. The Standard Model limits can be tested when the hadron collider results are combined with the measurement of χ_d from e^+e^- data on the $\Upsilon(4S)$, which gives $\chi_d = 0.16 \pm 0.04$ [65] (the $\Upsilon(4S)$ cannot decay into $B_s^0\overline{B}_s^0$). With higher statistics and smaller systematics than shown below, future $\overline{p}p$ results could extract V_{td}/V_{ts}.

Mixing is studied with a dilepton data sample, because if both B mesons in an event decay semileptonically, the lepton signs identify the parent mesons as $B\overline{B}$, BB, or $\overline{B}\,\overline{B}$. It should be noted, however, that there are other sources of leptons, most notably charm. The quantity directly measured in the $\overline{p}p$ experiments is

$$R = \frac{N(l^+l^+) + N(l^-l^-)}{N(l^+l^-)}$$

where UA1 uses their $\mu\mu$ sample [66] while CDF uses its $e\mu$ sample because of the lack of Drell Yan, J/ψ, and Υ background [67]. UA1 finds $R = 0.42 \pm 0.07 \pm 0.03$ and CDF finds $R = 0.55 \pm 0.05 \pm 0.04$, compared with the predictions of 0.26 ± 0.03 (UA1 energy) and 0.23 ± 0.06 (CDF energy) if there were no mixing. Clearly mixing is required by the data. The value of $\overline{\chi}$ can be extracted from R using

$$R = \frac{2\overline{\chi}(1-\overline{\chi})N_f + \left[(1-\overline{\chi})^2 + \overline{\chi}^2\right] N_s}{\left[(1-\overline{\chi})^2 + \overline{\chi}^2\right] N_f + 2\overline{\chi}(1-\overline{\chi})N_s + N_c}$$

N_f is the number of events in which both leptons come directly from B decay. N_s contains events where one lepton comes directly from B decay and the other comes from the sequential $b \to c \to l$ decay. N_c counts events in which the two leptons come from $c\overline{c}$ production. The equation can be understood if you note that in the numerator the coefficient in front of N_f is the probability that one and only one b mixes, while the coefficient in front of N_s is the probability that neither b mixes or both mix. Also note that $D\overline{D}$ mixing is negligible and has not been included. At present, N_s/N_f and N_c/N_f are determined from Monte Carlo calculations. The results are

$$\text{UA1}: \qquad \overline{\chi} = 0.158 \pm 0.059$$
$$\text{CDF}: \qquad \overline{\chi} = 0.176 \pm 0.028(stat) \pm 0.025(syst) \pm 0.032(Monte\ Carlo)$$

Figure 105 shows the CDF value rather than a combined CDF and UA1 result because the uncertainties in the two experiments are highly correlated due to the common Monte Carlo assumptions. The figure has been drawn with the assumption that b quarks form B_d, B_u, B_s, and b baryons 37.5%, 37.5%, 15%, and 10% of the time respectively. The $\overline{p}p$ and e^+e^- results overlap the allowed CKM region, but the uncertainties are big. In future Fermilab Collider runs, the large increase in the number of detected B events will allow for direct measurement of f_d and f_s from exclusive final states and a much more precise measurement of χ_s.

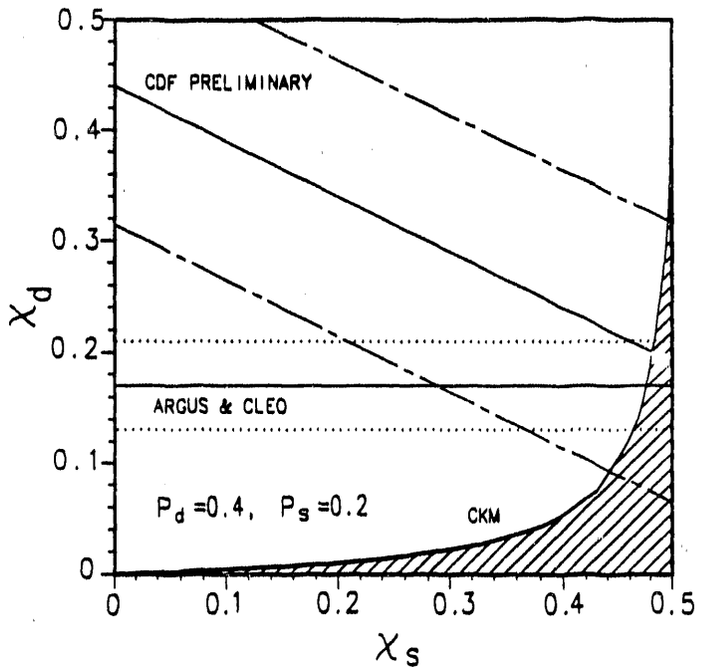

Fig. 105. B mixing results from e^+e^- and CDF. The dotted and dot-dashed lines are the one sigma limits.

6. The Search for Exotic Objects and Prospects for the Future

In this lecture, two separate topics will be considered. First I will present recent results from the search for new heavy objects. Then I will change focus from the present to the future and discuss the physics prospects with the extremely high integrated luminosity that should be provided by the upgraded Fermilab Collider.

6.1. The Search for Exotic Objects

Many objects outside the Minimal Standard Model have been searched for at the CERN and Fermilab Colliders. Four of these will be considered here, heavy Z and W bosons, quark compositeness, and supersymmetric objects.

6.1.1. Heavy Z Bosons

In many extensions to the Standard Model, there are additional U(1) symmetries and consequently neutral vector bosons (Z') [68]. CDF has searched its e^+e^- spectrum for the high-mass peak characteristic of a Z' (Fig. 106) [69]. The integrated high mass cross section is

$$\int_{110\ \mathrm{GeV/c^2}}^{\infty} \frac{d\sigma}{dM}\, dM = 4 \pm 1\ pb$$

to be compared to the Drell Yan continuum prediction of 4 pb. The lack of events above 200 GeV/c^2 translates into the limit

$$\int_{200}^{\infty} \frac{d\sigma}{dM}\, dM < 1.3\, pb \quad @95\%\, CL$$

The experimental upper limit on the Z' production cross section times the branching ratio into e^+e^- is compared in Figure 107 to a calculation assuming Standard Model couplings to quarks and leptons. For such couplings, additional heavy neutral vector bosons are excluded except in the region

$$M_{Z'} > 387\, GeV/c^2 \quad @95\%\, CL$$

For models in which Z' couplings to fermions are different than for the Standard Model Z^0 or for which $BR(Z' \to ee)$ is reduced because of other open channels such as $Z' \to W^+W^-$, the theoretical curve would change in the figure, but the experimental curve would remain the same.

6.1.2. Heavy W Bosons

Charged heavy vector bosons appear in some attempts to enlarge the $SU(2)_L \times U(1)_Y$ gauge group of the Standard Model [70]. In left-right symmetric models, for example, an additional $SU(2)_R$ symmetry produces a heavy right handed W. The best previous limit comes from the angular distribution in polarized μ decay [71]. The limit, $M_{W_R} > 450\ GeV/c^2$ @90% CL, is valid only if the right handed ν is very light ($m_{\nu_R} \lesssim 10\ MeV/c^2$).

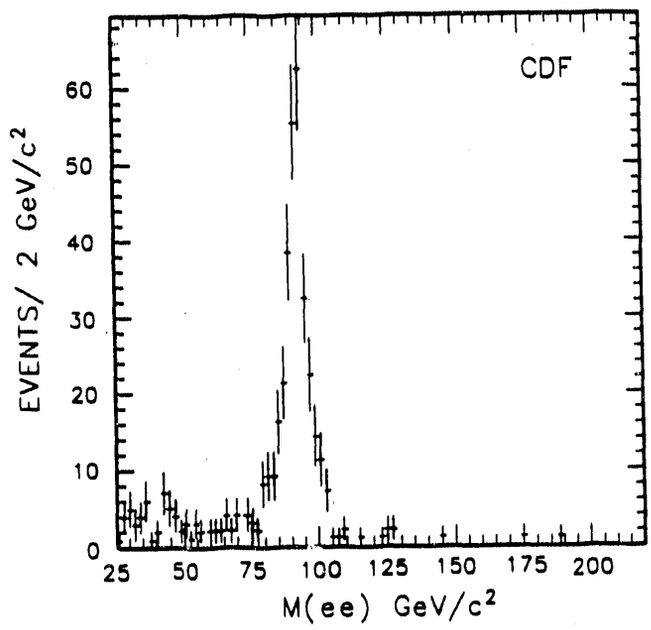

Fig. 106. The CDF e^+e^- spectrum.

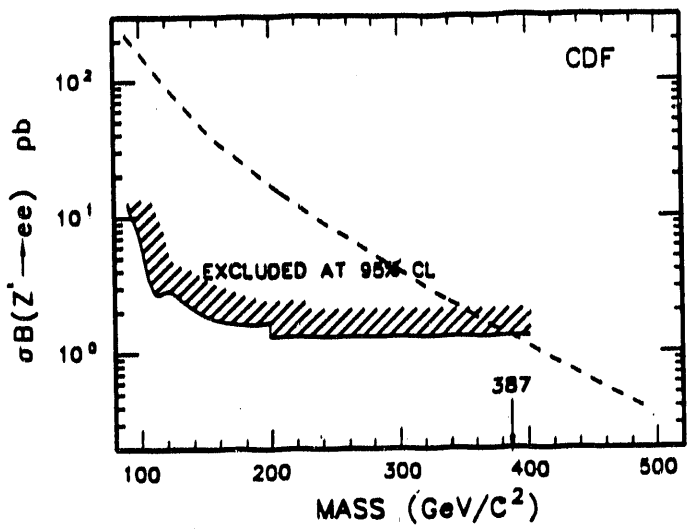

Fig. 107. The CDF 95% CL upper limit on the Z' production cross section times the branching ratio into e^+e^-. The dashed curve is the prediction assuming that the Z' couplings to quarks and leptons are the same as for the Standard Model Z^0.

A search for W_R with a much looser m_{ν_R} constraint ($m_{\nu_R} \lesssim \frac{1}{2}M_{W_R}$) can be carried out with the $l^{\pm}\nu$ transverse mass distribution in high energy $\bar{p}p$ collisions. Figure 108 shows the CDF data for both the $e\nu$ and $\mu\nu$ final states along with the expected distributions from the usual W [72]. There is clearly little room for additional sources of events. The data are fit to the form

$$\frac{dN}{dM_T} = \alpha W'(M_T) + \beta W(M_T)$$

where $W'(M_T)$ and $W(M_T)$ are the expected M_T distributions for W' and W decay normalized so that $\alpha = \beta = 1$ for Standard Model couplings. The fit is performed for the range of W' masses above 100 GeV/c^2. The resulting upper limit on $\sigma \cdot B(W' \to l\nu)$ places a limit

$$M_{W'} > 520\ GeV/c^2 \quad @95\%\ CL$$

for Standard Model couplings (Fig. 109).

6.1.3. Quark Compositeness

In some attempts to understand the origin of the fermion generations, it is postulated that the fermions are composite. However the experimental evidence on the pointlike nature of the fermions requires that such compositeness be at a very small distance scale or equivalently at a very large energy scale. The effect can be parametrized in terms of a 4-fermion interaction of unit strength between left handed quarks, characterized by a constant, Λ_c, with dimensions of energy (like $1/\sqrt{G_F}$) [73].

If quarks were composite objects, the inclusive jet production cross section would be enhanced at high E_T . Figure 110 shows the CDF inclusive jet production cross section

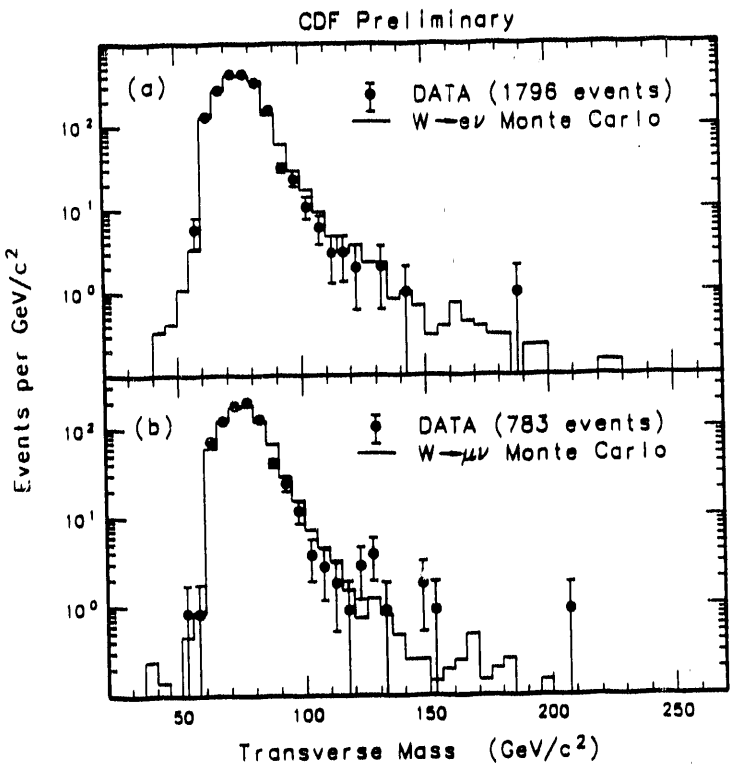

Fig. 108. The CDF transverse mass distributions for the (a) $e\nu$ and (b) $\mu\nu$ data samples. The solid lines are the expectations from the usual W.

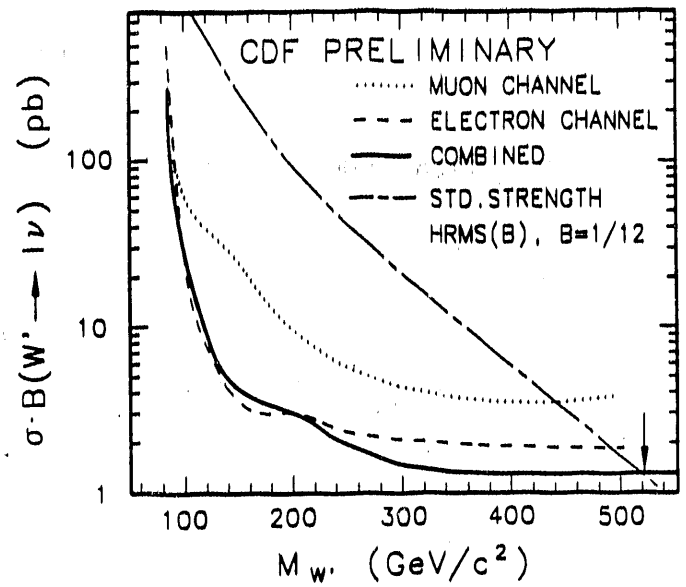

Fig. 109. The CDF 95% CL upper limit on the W' production cross section times the branching ratio into $l\nu$. Shown are the limits from the electron channel, the muon channel, and the combined sample. The dot-dashed curve is the prediction assuming Standard Model couplings of the W' to quarks and a 1/12 branching ratio into either $e\nu$ or $\mu\nu$.

as a function of E_T along with the predictions from lowest order QCD and lowest order QCD plus a composite-quark contact interaction [74]. CDF finds

$$\Lambda_c > 1.4\,TeV \quad @95\%\,CL$$

The absence of events with $E_T > 450\,GeV$ plays an important role in determining the limit.

If quarks and leptons share constituents, there should be an enhancement in continuum lepton pair production for large dilepton invariant mass. The CDF integral e^+e^- mass spectrum is shown in Figure 111 along with the predictions from Drell Yan production and quark-lepton compositeness [75]. The limits on a quark-lepton contact interaction are

$$\Lambda^-_{LL} > 2.2\,TeV \quad @95\%\,CL$$
$$\Lambda^+_{LL} > 1.7\,TeV \quad @95\%\,CL$$

where the $-$ $(+)$ limit is for constructive (destructive) interference with the usual u quark Drell Yan contribution.

6.1.4. Supersymmetry

If supersymmetric partners of the quarks and gluons exist, they can be pair produced via the strong interaction in $\bar{p}p$ collisions. If $m_{\tilde{g}} > m_{\tilde{q}}$, the dominant production mode is $p\bar{p} \to \tilde{q}\bar{\tilde{q}} \to q\tilde{\gamma}\bar{q}\tilde{\gamma} \to 2$ jets $+ \not{E}_T$. If, on the other hand, $m_{\tilde{q}} > m_{\tilde{g}}$, the dominant production mode is $p\bar{p} \to \tilde{g}\tilde{g} \to q\bar{q}\tilde{\gamma}q\bar{q}\tilde{\gamma} \to 4$ jets $+ \not{E}_T$. Here I have assumed the

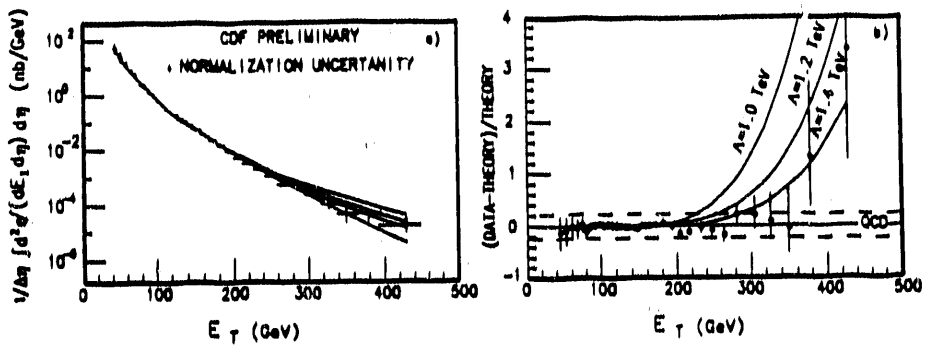

Fig. 110. (a) The CDF inclusive jet production cross section, and (b) the deviation of the data from the lowest order QCD calculation. The three upper curves include a 4-fermion interaction with different choices for Λ_c.

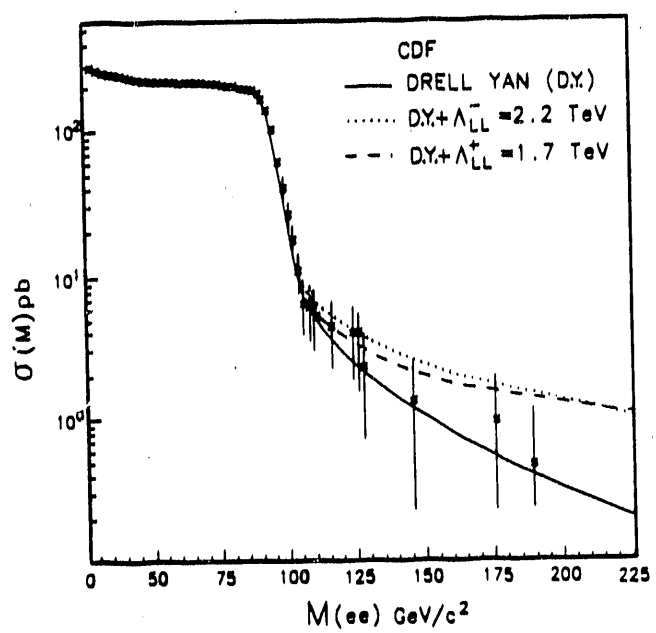

Fig. 111. The integral invariant mass distribution, $\sigma(M) = \int_M^\infty d\sigma$, for the CDF e^+e^- data. The curves are predictions for Drell Yan production alone and with a quark-lepton compositeness interaction added.

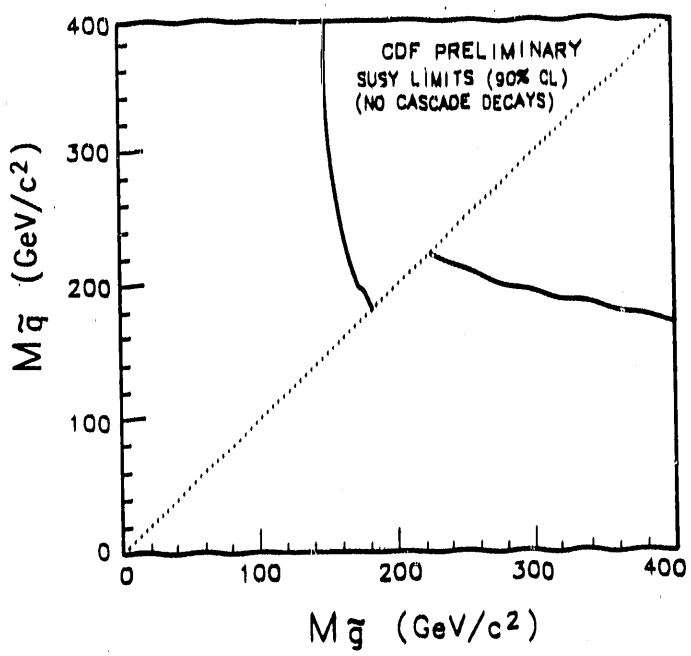

Fig. 112. The CDF supersymmetry limits. The region to the left and below the curves is ruled out.

simplest supersymmetric model in which the squark or gluino decays directly to the lightest supersymmetric particle (LSP), taken to be the photino which is stable and virtually non-interacting. In more realistic models for very heavy squarks and gluinos, the $\tilde{q}$ and $\tilde{g}$ cascade down to the LSP. This results in more partons in the final state and consequently less $\not{E}_T$.

CDF has searched for squarks and gluinos in the sample of events with $\not{E}_T$>40 GeV and two or more jets [76]. The 93 observed events are consistent with the rate expected from QCD production of Z + jets, where $Z \to \nu\nu$, and W + jets, where $W \to l\nu$ and the charged lepton is not identified in the detector. The lack of additional events translates into the supersymmetry limits shown in Figure 112. These limits are for the simple supersymmetry model with direct decay down to the LSP. It has been estimated that the limits are reduced by $10 - 20\ GeV/c^2$ when cascade decays are considered.

6.2. Collider Physics with the Fermilab Main Injector

The Fermilab upgrade including the construction of the Main Injector was described in Section 1. When it is completed, CDF and D0 should each be able to collect 1 fb^{-1} of integrated luminosity during two years of taking data. This assumes that the upgraded Collider runs at design luminosity and luminosity lifetime, that the efficiency of accelerator operation is as it was during the last data run, and that detector downtime and deadtime are each held to 10%. For the projections made below, I assume a detector with "full" lepton and jet coverage, as expected for the upgraded CDF and D0 detectors. Moreover, the assumed detector inefficiencies are based on the last CDF

run. This should be improved upon in the future for both detectors.

6.2.1. Search for the Top Quark

As we have seen, the current lower limit on the top quark mass is 91 GeV/c^2 at the 95% confidence level. The indirect evidence based on the consistency of the minimal Standard Model (Z decay, M_W, ν scattering, etc.) provides an upper limit, $M_{top} <$ 200 GeV/c^2. However more than a 3σ discrepancy with the Standard Model prediction would be required before the Standard Model would be abandoned. Thus to test the Standard Model, the top mass range up to 250–300 GeV/c^2 must be explored.

Detection of heavy top can occur in the $l\nu+4jet$ and $ll\nu\nu+2jet$ final states, where l includes electrons and muons. The branching ratio is 30% for the former and 5% for the latter, while the detection efficiency is approximately 30% for the single lepton mode and 25% for the dilepton mode. These efficiencies might in fact be larger, because there is no need to cut hard on the lepton identification variables. The dominant background is from W and Z decay into electrons or muons, so cutting hard reduces signal and background similarly. Table 6 gives, as a function of the top quark mass, the number of $t\bar{t}$ events produced and the number that should be detected in each mode for a 1 fb^{-1} data sample.

M_{top} $[GeV/c^2]$	$N_{t\bar{t}}^{produced}$	$N_{l+4\,jet}^{detected}$	$N_{ll+2\,jet}^{detected}$
100	80,000	<7200	1000
140	15,000	1350	200
180	3300	300	40
220	1000	90	12
260	350	30	5
300	120	10	2

Table 6
Number of $t\bar{t}$ events that should be produced and detected for a 1 fb^{-1} data sample as a function of M_{top}.

The number of signal events of course is not the only, or perhaps even the major consideration. The size of the background is also of crucial importance. For the single charged lepton final states, the dominant source of background is QCD W + 4 jet production. CDF does not as yet have a large sample of W + 4 jet events. Consequently we have to rely on Monte Carlo simulations. At the time these estimates were made, the W + 4 jet calculation was not yet available. We used the W + 3 jet calculation and multiplied the cross section by α_s to approximate the effect of requiring an additional jet. This is consistent with the CDF cross section ratio (W + 0 jet)/(W + 1 jet)/(W + 2 jet)/(W + 3 jet). Figure 113 shows the E_T spectrum of the third highest E_T jet for 150 and 210 GeV/c^2 top as well as for the background. The background jet E_T spectrum is rapidly falling, in contrast to the top decay spectrum which becomes harder as M_{top} increases. By selecting a jet E_T threshold that increases with M_{top}, a satisfactory signal to noise ratio can be maintained over a large M_{top} range extending to over 200 GeV/c^2.

If this proves not to be sufficient, a significant improvement in the signal to noise ratio can be obtained by identifying one or both of the b jets in the event. Low energy

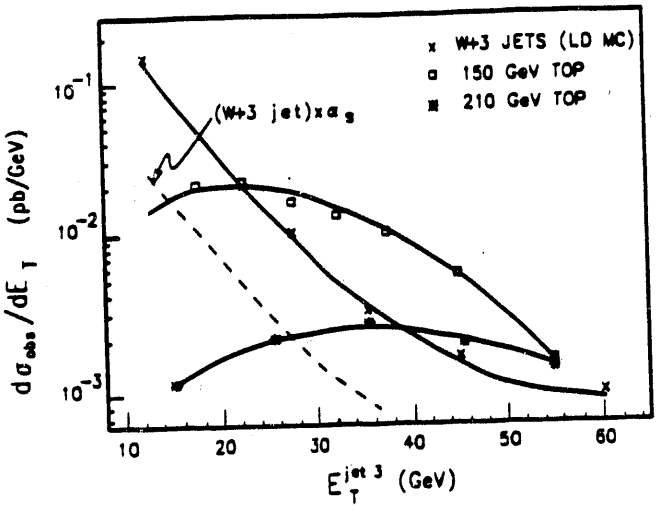

Fig. 113. The E_T spectrum for the third highest E_T jet in single charged lepton events from 150 and 210 GeV/c^2 top, a W + 3 jet Monte Carlo, and a W + 4 jet estimate taken to be α_s times the W + 3 jet spectrum.

leptons from semileptonic b decay can be used to tag b quarks, but a 10% branching ratio penalty must be paid. A higher b tagging efficiency can be obtained by observing the secondary vertex from b decay. The CDF silicon vertex detector should have a 10–15 μ impact parameter resolution, to be compared to $c\tau \simeq 300\mu$ for B mesons. It is estimated that at least one b jet can be identified in over 50% of heavy top events.

For the dilepton final states, there are two major sources of background to high mass top. The QCD production of Z + 2 jets followed by the decay $Z \to ee$, $Z \to \mu\mu$, or $Z \to \tau\tau \to ll\nu\nu\nu\nu$ can be easily removed using the dilepton invariant mass, $\not{E}_T$, and $\Delta\phi^{ll}$. The more difficult background is vector boson pair production, $p\bar{p} \to WW$ + 2 jets $\to ll\nu\nu + 2$ jets. Again, by choosing a jet E_T threshold that increases with M_{top}, a good signal to noise ratio can be maintained over the accessible M_{top} range (Fig. 114) [77].

If these background estimates prove accurate, there should be a significant number of detected $t\bar{t}$ events ($\geq 25\ l + \nu + 4$ jet events and $\geq 5\ ll\nu\nu + 2$ jet events per detector) with good signal to noise up to $M_{top} = 260 - 270\ GeV/c^2$. Approximately 10 single lepton and a few dilepton events are expected per detector at $M_{top} = 300\ GeV/c^2$. Thus the entire range allowed in the Standard Model would be covered.

If a signal appears, there are a number of ways that its identity as a top quark can be tested. The number of events with 0, 1, or 2 identified secondary vertices should be consistent with two b jets per $t\bar{t}$ event. The secondary vertex detection efficiency can be measured with the inclusive lepton data sample, which is mostly from b decay. One can also look at the ratio of the numbers of single lepton and dilepton events. This should be consistent with two W bosons per event. There can be additional confirmation of the presence of two W bosons using, for example, the $l\nu$ transverse mass and the dijet invariant mass. Finally, one can see if the production cross section is consistent with the QCD prediction. The theoretical cross section uncertainty is approximately ± 20-30%.

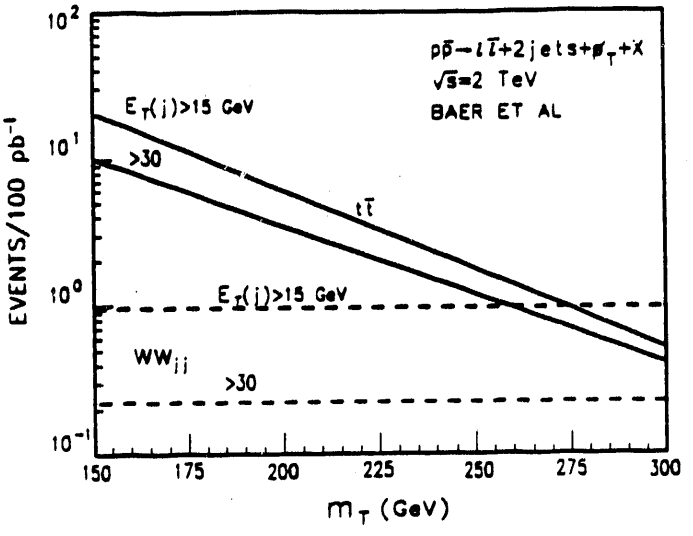

Fig. 114. The dilepton event rate for a top signal and the WW background as a function of the top quark mass. Curves are shown for two different jet E_T thresholds.

Another important issue is the accuracy with which the top quark mass can be measured. This question is actively being addressed at present in both the CDF and D0 collaborations. There are some preliminary estimates; much more will be done within the next year.

In the single lepton modes, the invariant mass of the W and b jet can be calculated. However finding the correct jet to match with the W is not easy because of the large number of jets in each event. One study showed that after making additional kinematic cuts to restrict the event sample, the $W + b$ jet invariant mass distribution has a 20% width. This would give a $\pm 5\ GeV/c^2$ statistical uncertainty for a 200 GeV/c^2 top. The systematic uncertainty could be studied using events in which both b jets are identified. The remaining two leading jets should have a mass peak centered on M_W with a width as predicted by the detector simulation. Other potentially precise techniques are under study in which the mass is determined by partial or full reconstruction of the t and $\bar{t}$ [78]. Another possibility is to compare the $\not{E}_T$ distribution and the E_T distributions of the lepton, W jets, and b jets with simulation results as a function of top mass.

For the dilepton modes, Baer et al [77] have considered a number of mass estimators. The best of these is the lowest reconstructed top mass when the transverse momenta of the two neutrinos are varied, but constrained so that the sum equals the observed $\not{E}_T$. They find a mass resolution of $\pm 10\ GeV/c^2$ for a 200 GeV/c^2 top mass using this method.

Finally, comparing the event rate with the calculated cross section provides an estimate of M_{top} with an uncertainty of $\leq 10\%$. This of course assumes that the branching ratio for $t \to Wb$ is 100%.

What else can be learned about the top quark once it is discovered? To be concrete, let us assume that $M_{top} = 150\ GeV/c^2$. A 1 fb^{-1} exposure would then provide 1000 detected single lepton events and 130 dilepton events. The most important study of

course is the precision test of the Standard Model. This is discussed in the next section.

A large data sample can also be used to search for non-standard decay modes. For example, the ratio of the numbers of events with one and two identified secondary vertices gives a sensitivity to a 10% branching ratio into modes with no b quarks, like $t \rightarrow W + s$. More likely is the decay of the top into modes with no W in the final state, such as $t \rightarrow H^+b$ which occurs in supersymmetry inspired extensions to the Higgs sector [79]. For the case of two Higgs doublets, there are two additional parameters in the theory, the mass of the charged Higgs and the ratio of the vacuum expectation values for the two Higgs doublets, $tan\beta \equiv v_2/v_1$. If $M_{H^+} < M_{\rm top}$, the dominant Higgs decays are to $\tau\nu$ and $c\bar{s}$, where $\tau\nu$ dominates for $tan\beta > 1$ and $c\bar{s}$ dominates for $tan\beta < 1$. The branching ratios for $t \rightarrow Wb$ and $t \rightarrow Hb$ also depend strongly on $tan\beta$. Typically $BR(t \rightarrow Wb)$ is $\gtrsim$ 10% when $0.1 < tan\beta < 100$. Initial studies show that $t\bar{t} \rightarrow HbHb \rightarrow \tau\tau\nu\nu bb$ can be observed with good signal to noise using a $\not{E}_T$ trigger, secondary vertex identification, and the characteristics of τ decay. From the rate of such decays, the rate of $l + \nu + 4$ jet events, and the dilepton to single lepton ratio, the top quark can be observed if $tan\beta > 0.1$, with the effect of the Higgs channel observable over most of this range.

A number of other studies can be done with the top sample. Some fraction of the 1000 events should be fully reconstructed. The decay angular distributions can provide information on the spin of the decaying object. One can also look at the $t\bar{t}$ invariant mass spectrum for resonances such as technimesons. One could also look for particles produced with the $t\bar{t}$, for example third generation leptoquark pairs $\rightarrow t\tau\bar{t}\bar{\tau}$. And finally one must be prepared for the totally unexpected. The top quark is already an oddity being the only elementary fermion with a mass close to the electroweak unification scale. Perhaps the top quark is unique in other ways as well.

6.2.2. Precision Measurement of the W Mass

With a 1 fb^{-1} data sample, more than 10^6 $W \rightarrow l\nu$ events and 10^5 $Z \rightarrow ll$ events will be detected. The very large Z sample is critical since it is used to study and measure many of the sources of systematic uncertainty in the W mass: calorimeter energy scale, detector resolution, P_T of the W, effect of electron energy leakage on the measured P_T of the ν, background, and the mass fitting procedure.

The statistical uncertainty in M_W should be $\lesssim$ 30 MeV/c^2. The dominant systematic uncertainty may well be the imprecise knowledge of the structure functions, which affects the W rapidity distribution. However the measurement of the W charge asymmetry will give the needed u to d ratio for the relevant range of x and q^2. If no unexpected new sources of systematic uncertainty arise, it is possible that the W mass can be measured to ± 50 MeV/c^2.

Such a measurement, coupled with the measurement of $M_{\rm top}$, provides a powerful test of the Standard Model at the level of electroweak radiative corrections (Fig. 115). If the result disagrees with the Standard Model, it is obviously extremely important. On the other hand, even if it is consistent with the Standard Model, it can provide information about the Higgs mass.

6.2.3. The W Lifetime and Hidden Top

As shown in section 3, the W lifetime can be deduced from a measurement of R, the ratio of the numbers of $W \rightarrow l\nu$ and $Z \rightarrow ll$ events produced. The measurement is important since the lifetime is a basic property of a gauge boson. Moreover, it allows a

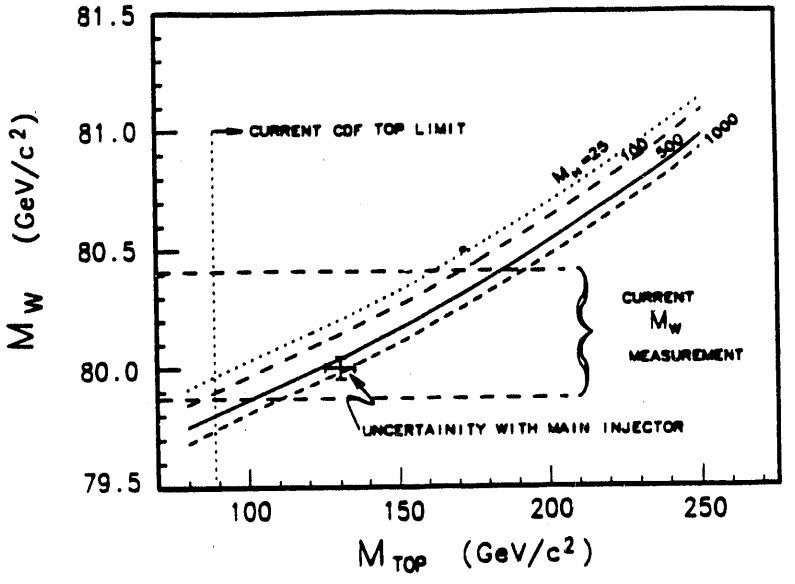

Fig. 115. The Standard Model relation between the W and top masses for different values of the Higgs mass. The data point shows the precision possible with a 1 fb^{-1} data sample.

loophole in the top quark search to be closed. If the top decay cannot be detected, for example because $t \to H^+b \to c\bar{s}b$, the usual top searches would fail. This is particularly important if M_{top} is between $M_Z/2$ and M_W, since the decay of top into a real Higgs could then dominate over the decay into a virtual W. However since the $W \to t\bar{b}$ channel is open for such a top quark mass, $\Gamma(W)$ would increase. A 1 fb^{-1} data sample would give a statistical uncertainty in the R measurement of approximately 0.5% and a systematic uncertainty of roughly 1%, dominated by structure function uncertainties. Figure 116 shows how the R measurement could largely close this loophole in the top quark search.

6.2.4. Vector Boson Pair Production

The rate and angular distribution for $q\bar{q} \to W\gamma$ can provide a measurement of the anomalous magnetic moment of the W. A 1 fb^{-1} data sample will contain approximately 2000 events with $W \to l\nu$ and $P_T^\gamma > 10$ GeV/c with which to measure the moment.

For the other vector boson pairs, WW or WZ or ZZ, QCD background swamps the signal unless both bosons are required to decay into e or μ. After paying the price of two leptonic branching ratios, we would only expect to see 5 WZ events and 1 ZZ event. The WW signal would be much larger, 125 events, but these events are not fully reconstructible since there are two neutrinos present. Moreover, there will hopefully be a large background to the WW signal from top quark decay! Although the number of reconstructed events will be small, the experiment will be quite sensitive to anomalous vector boson pair production, due either to a failure of the diagram cancellation in the Standard Model or to the presence of WW and WZ resonances predicted in some models.

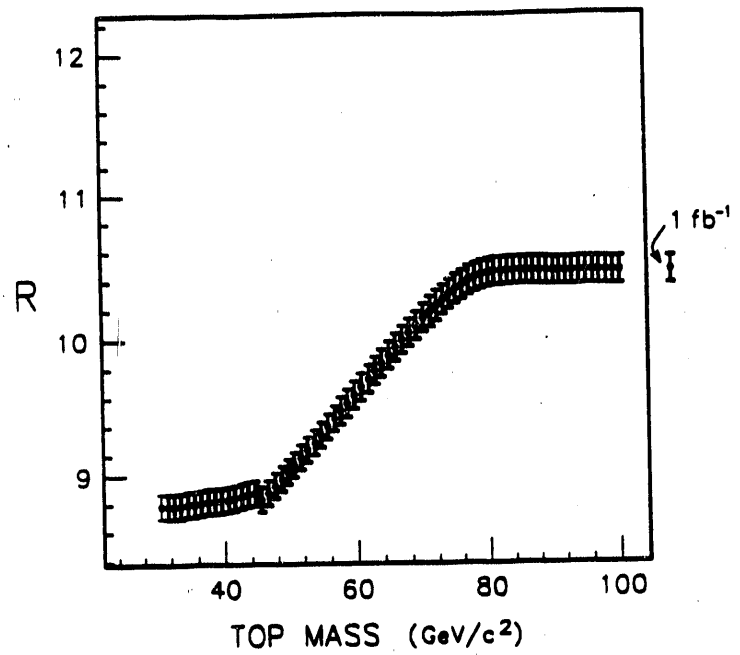

Fig. 116. The Standard Model relation between R and the top quark mass. The data point at the right shows the size of the uncertainty possible with 1 fb^{-1} of data.

6.2.5. Other Heavy Particles

A very large data sample can significantly extend the search for objects beyond the Standard Model. Heavy W or Z bosons could be detected for masses up to roughly 1 TeV/c^2 assuming Standard Model couplings. The limits for supersymmetric particles, technimesons, and leptoquarks should reach 250 – 300 GeV/c^2. Both inclusive jet production and Drell Yan lepton pair production can provide a compositeness search up to an energy scale approaching 3 TeV.

6.2.6. B Physics

The cross section for $b\bar{b}$ production in the central four units of rapidity is approximately 1×10^{-28} cm^2. This means that 10^{11} $b\bar{b}$ events will be produced for a 1 fb^{-1} integrated luminosity. With an instantaneous luminosity of 5×10^{31} $cm^{-2} - sec^{-1}$, the $b\bar{b}$ production rate would be 5 KHz! Even if the acceptance range is limited to $|y| < 1$ and $P_T^b > 10$ GeV/c, the event rate would still be 200 Hz, and 4×10^9 $b\bar{b}$ events would be collected.

There are many experimental challenges that have to be met if hadron collider experiments are to make a major impact on b physics. Since the b production cross section is only $\approx 0.2\%$ of the inelastic $\bar{p}p$ cross section and the rate for writing events to magnetic tape is limited by the bandwidth of the data acquisition system, the purity and efficiency of the b trigger is critical. This means having low P_T thresholds for e, μ, and J/ψ while maintaining a high signal to noise ratio. Of enormous utility would be fast (~ 10 μsec) secondary vertex finding. Another problem is data storage

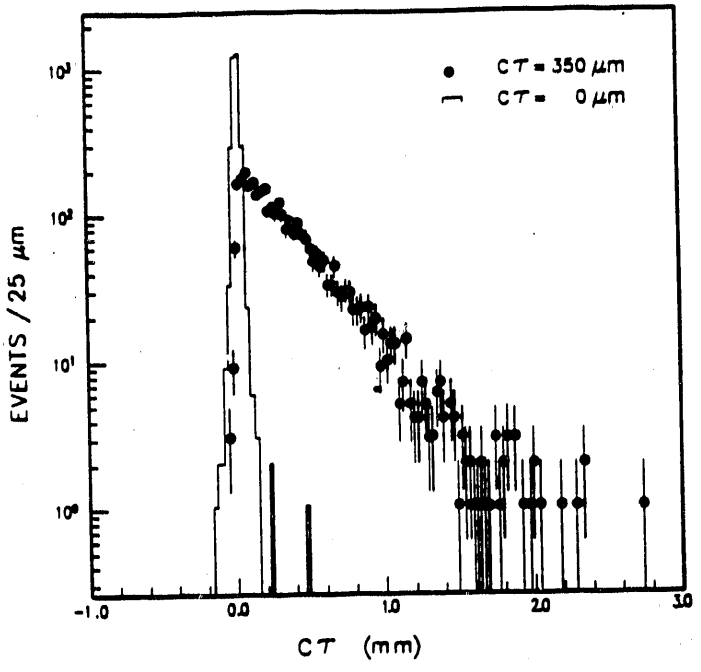

Fig. 117. Monte Carlo simulation of the reconstructed proper lifetime distribution for $B^{\pm} \to J/\psi K^{\pm}$ (data points) and for a similar resonance that decays at the primary vertex.

for very large event samples. This requires efficient online separation of signal from background and data compaction to minimize the size of each event. Identification of b jets is also critical; it requires an efficient secondary vertex detector. But perhaps most important for the observation of CP violation is flavor tagging of the second b in an event. Techniques under study include K identification, efficient detection of moderate P_T leptons, and very efficient track finding at the secondary vertex so that the charge of the decaying B can be measured. During the last CDF run, the flavor tagging efficiency was approximately $\frac{1}{2}$% due to the B semileptonic branching ratio, the muon identification requirements, and the limited range of rapidity and P_T covered. If CP violation is to be studied in $\bar{p}p$ collisions, the tagging efficiency must be increased by approximately a factor of ten.

The b physics opportunities are extensive. The B_s, B_c, Λ_b, and other b hadrons should be observed and their masses measured (a 13 MeV/c^2 mass resolution is expected for the next run). Precision measurements will be made of the individual lifetimes for B_u, B_d, and B_s; a 3% uncertainty is expected in the next run for B_u and B_d (Fig. 117). A sensitive search for rare B decay modes can also be carried out. The predicted 10^{-9} branching ratio for $B \to \mu\mu$ could be observed. In addition, $B \to \mu\mu K$, which occurs through an electromagnetic penguin diagram, should be seen with good statistics. It is sensitive to $M_{\rm top}$ as well as other new massive particles and provides a measure of the CKM matrix element V_{ts}.

Direct observation of the interference effects of B_s mixing is a major b physics goal. Figure 118 shows what could be observed with dilepton events for $X_s \equiv \frac{\Delta M}{\Gamma} = 5$.

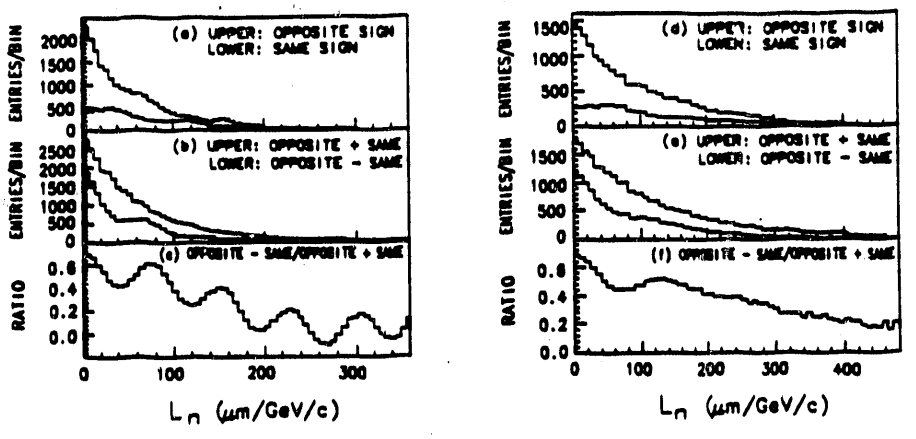

Fig. 118. The distribution in $b\bar{b} \to 2$ lepton events of $L \equiv c\tau$, where τ is the proper decay time of each B. (a) The distributions for events with opposite sign or same sign leptons. (b) The sum and the difference of the curves in (a). (c) The ratio of the difference and sum curves in (b). (d), (e), and (f) are the same as (a), (b), and (c), except that the B momentum used to obtain the proper decay time is approximated by the lepton momentum.

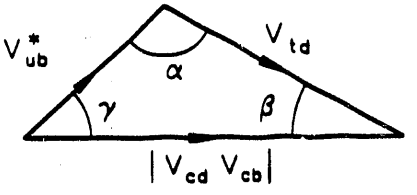

Fig. 119. The CKM unitarity triangle.

Figure 118c clearly shows the oscillations due to B_s, $\overline{B}_s$ mixing. The major challenge here is to find the best estimator of the B momentum for determining the proper time of the B decay. Figure 118f shows the degradation of Figure 118c if the lepton momentum is used as the B momentum.

The ultimate goal for $\bar{p}p$ b physics is the observation of CP violation in B decay. Let us review how this can be done. The unitarity of the CKM matrix for the three known fermion generations requires

$$V_{ud}V^*_{ub} + V_{cd}V^*_{cb} + V_{td}V^*_{tb} = 0$$

Since $V_{ud} \approx 1$, $V_{tb} \approx 1$, and with the usual phase convention V_{cb} is positive real and V_{cd} is negative real, the equation becomes

$$V^*_{ub} + V_{td} = |V_{cd}V_{cb}|$$

which is a triangle in the complex plane (Fig. 119). CP violation can result if the angles are non-zero. Information on the lengths of the sides of the triangle comes from semileptonic B decay (V_{ub}, V_{cb}), opposite sign dimuon production in ν interactions (V_{cd}), and $B-\overline{B}$ mixing (V_{td}). The angles can be determined by measuring CP violating

asymmetries in the decay of B and $\overline{B}$ into CP eigenstates, specifically

α : $B_d \rightarrow \pi^+\pi^-$
β : $B_d \rightarrow \psi K_s$
γ : $B_s \rightarrow \rho K_s$

To determine whether CP violation as observed in the K system is consistent with a CKM origin, one could measure the three sides and one angle. Hadron colliders could contribute to the measurement of V_{td} ($B_s - \overline{B}_s$ mixing, rare B decay, top mass) and β (CP asymmetry in $B_d \rightarrow \psi K_s$). Current data on the CKM matrix and CP violation in K decay suggest that $0.1 < sin2\beta < 1$, with 0.34 the most likely value [80]. A future measurement of this quantity with the ψK_s final state will have its accuracy limited by luminosity (number of events) and the efficiency for tagging the parent as B or $\overline{B}$. The latter is characterized by

$$d_{tag} = \epsilon_{tag}(1-2w)^2(1-2\overline{\chi})^2$$

where ϵ_{tag} is the efficiency for tagging the other B meson, w is the probability that the tag gives the wrong answer, and the last factor in the equation is due to dilution from B mixing. Figure 120 shows how this translates into uncertainty in the $sin2\beta$ determination. An uncertainty in $sin2\beta$ of 0.33 (0.11) can be expected if the b tagging efficiency can be improved by a factor of 2 (10) over what is expected in the next CDF data run.

Studying CP violation in B decay at hadron colliders will be very challenging, but it appears quite possible.

7. Acknowledgements

I would like to thank my CDF colleagues, who are responsible for much of the work presented here. Special thanks go to Henry Frisch, Chris Hill, John Huth, Hans Jensen, Jon Rosner, Paul Tipton, and Alvin Tollestrup for helpful discussions about accelerator physics, electroweak tests, and the future of Collider b physics.

References

[1] *Design Report, Tevatron 1 Project*, Fermi National Accelerator Laboratory, 1984 (unpublished)
[2] *The Fermilab Upgrade - The Main Injector*, Fermi National Accelerator Laboratory, 1989 (unpublished)
[3] F. Abe et al, NIM A271 (1988), 387, and references therein.
[4] F Abe et al, PRL 63 (1989), 720
Particle Data Group, PL B239 (1990), 1
James Pilcher, Washington APS meeting, April 1991 (unpublished)
[5] D. Perkins, *Introduction to High Energy Physics*, 3rd edition, 304
[6] G. Altarelli and G. Parisi, Nucl.Phys. B126 (1977), 298
[7] F. Abe et al, Fermilab preprint FNAL PUB 91/181 (1991), submitted to Physical Review D
[8] M. Banner et al, PL B118 (1982), 203
[9] P. Gianetti, *Proceedings of Les Rencontres de Physique de la Valee d'Aoste*, La Thuile, Italy (1991)

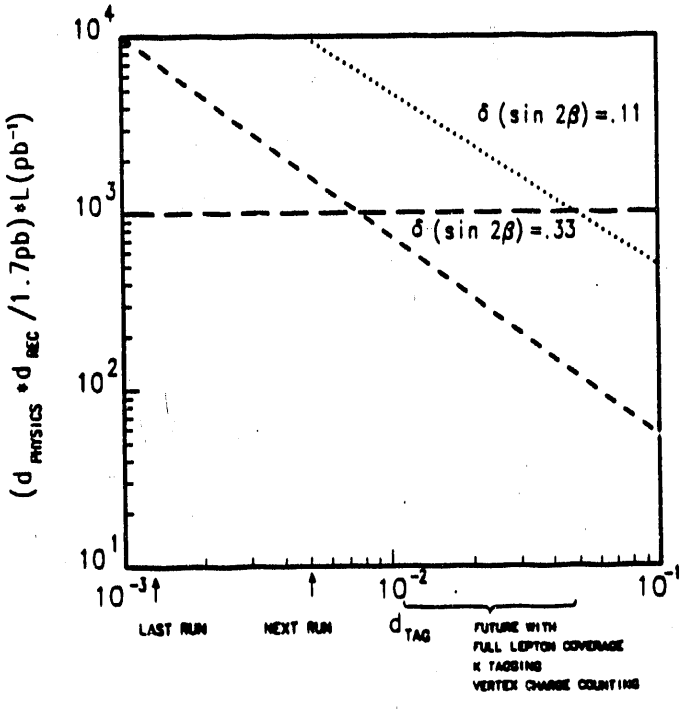

Fig. 120. The luminosity required to observe a CP asymmetry as a function of d_{tag}. The two dotted lines correspond to measurement uncertainties in $sin2\beta$ of 0.11 and 0.33. The horizontal line is the integrated luminosity expected in a two year run with the upgraded Fermilab Collider.

[10] G. Marchesini and B. Webber, Nucl.Phys. B310 (1988), 461
[11] R. Plunkett, *Proceedings of the 1991 Lepton-Photon Conference*, Geneva, (1991)
[12] S. Ellis, Z. Kunst, and D. Soper, PRL 64 (1990), 2121
[13] P. Harriman et al, Rutherford Laboratory Preprint RAL-90-007 (1990)
[14] G. Arnison et al, PL B136 (1984), 294
[15] G. Arnison et al, PL B136 (1984), 294
[16] M. Dell'Orso, *Proceedings of the XXVth International Conference on High Energy Physics*, Singapore (1990)
[17] G. Arnison et al, PL B158 (1985), 494
[18] J.A. Appel et al, Z.Phys. C30 (1986), 341
[19] G. Punzi, *Proceedings of the XXVth Rencontres de Moriond* (1990)
[20] I. Hinchliffe (in preparation)
[21] E. Buckley-Geer, *Proceedings of the VI Conference on Intersections of Particle and Nuclear Physics*, Tuscon (1991)
[22] J. Patrick, *Proceedings of the SLAC Summer Institute* (1991)
[23] S. Ellis and D. Soper, private communication
[24] C. Albajar et al, PL B209 (1988), 385
[25] J.A. Appel et al, PL B176 (1986), 239
[26] P. Aurenche et al, PR D42 (1990), 1440
[27] R. Plunkett, *Proceedings of the 1991 Lepton-Photon Conference*, Geneva, (1991)
[28] C. Albajar et al, PL B209 (1988), 385
[29] R. Ansari et al, PL B215 (1988), 175
[30] A few recent references:
W.A. Bardeen and C.T. Hill (in preparation)
D.C. Kennedy and P. Langacker, PRL 65 (1990), 2967
J.L. Rosner, University of Chicago preprint EFI 90-18 (1990)
Z Physics at LEP 1, CERN 89-08 (1989), 55
[31] J. Alitti et al, PL B241 (1990), 150
[32] F. Abe et al, PR D43 (1991), 2070
[33] The fine structure constant has been run from $q^2 \simeq 0$ to $q^2 = M_Z^2$. See the references in [30].
[34] James Pilcher, Washington APS meeting, April 1991 (unpublished)
[35] F. Abe et al, PRL 67 (1991), 1502
[36] C. Albajar et al, Z.Phys. C44 (1989), 15
[37] B. Winer, *Proceedings of the 1991 Lepton-Photon Conference*, Geneva (1991)
[38] A.D. Martin, W.J. Stirling, and R.G. Roberts, PL B228 (1989), 149
[39] C. Albajar et al, CERN-PPE/90-141
[40] J. Alitti et al, Z.Phys. C47 (1990), 11
[41] F. Abe et al, PRL 64 (1990), 152
[42] C. Albajar et al, Z.Phys. C44 (1989), 15
[43] H. Plothow-besch, CERN-PPE/90-168 (1990)
[44] F. Abe et al, submitted to PRL
[45] W. Bartel et al, PL B146 (1984), 437
[46] Particle Data Group, PL B239 (1990), 1
[47] G. Altarelli et al, Nucl.Phys. B308 (1988), 724
R.K. Ellis, Fermilab-Pub-91/30-T
These use the next-to-leading-order calculation in
P. Nason, S. Dawson, and R.K. Ellis, Nucl.Phys. B303 (1988), 607

[48] F. Abe et al, PRL 64 (1990), 147
F. Abe et al, PRL 64 (1990),142
F. Abe et al, PR D43 (1991), 664
F. Abe et al, Fermilab-Pub-91/280-E, submitted to PRL
F. Abe et al, submitted to Physical Review D
[49] C Albajar et al, Z.Phys. C48 (1990),1
[50] T. Akesson et al, Z.Phys. C46 (1990), 179
[51] For example, see:
R.K. Ellis, *Proceedings of the 7th Topical Workshop on Proton–Antiproton Collider Physics*, Fermilab (1988), 639
P. Nason, *Proceedings of the XXIV International Conference on High Energy Physics*, Munich (1989), 962
[52] G. Altarelli et al, Nucl.Phys. B308 (1988), 724, based on the order α_s^3 calculation of P. Nason, S. Dawson, and R.K. Ellis, Nucl.Phys. B303 (1988), 607
[53] An excellent summary of the b studies carried out by the UA1 collaboration is given in N. Ellis and A. Kernan, Phys.Rep. 195 (1990), 23
[54] C. Albajar et al, PL B256 (1991), 121
[55] A. Sansoni, *Proceedings of the 25th Rencontres de Moriond*, (1991)
[56] *b Physics at CDF*, Fermilab (1991), unpublished
[57] R. Hughes et al, CDF Internal Note 1448 (1991), unpublished
[58] M.S. Alam et al, PR D34 (1986), 3279
H. Albrecht et al, PL B199 (1987), 451
[59] A. Yagil, CDF Internal Note 1526 (1991), unpublished
[60] D.A. Crane, *Proceedings of the XIth International Conference on Physics in Collision*, Colmar, France (1991)
[61] Particle Data Group, PL B239 (1990), 1
[62] C. Albajar et al, CERN-PPE/91-54, submitted to Phys.Lett.
[63] L. Pondrom, *Proceedings of the 25th International Conference on High Energy Physics*, Singapore (1990)
[64] C. Albajar et al, PL B186 (1987), 247
[65] H. Albrecht et al, PL B192 (1987), 245
M. Artuso et al, PRL 62 (1989), 2233
[66] C. Albajar et al, CERN-PPE/91-55 (1991), submitted to Phys.Lett.
[67] F. Abe et al, PRL 67 (1991)
[68] See for example,
G.G. Ross, *Grand Unified Theories*, Cambridge U.P. (1987) and references therein
R.N. Mohapatra, *Unification and Supersymmetry*, Springer (1986)
X.G. He, G.C. Joshi, and R.R. Volkas, PR D43 (1991), R22
[69] F. Abe et al, PRL 67 (1991), 2418
[70] J. Pati and A. Salam, PR D10 (1974), 275
R.E. Marshak and R.N. Mohapatra, PL B91 (1980), 222
[71] J. Carr et al, PRL 51 (1983), 627
B. Balke et al, PR D37 (1988), 587
[72] F. Abe et al, PRL 67 (1991), 2609
[73] E. Eichten, K. Lane, and M. Peskin, PRL 50 (1983), 811
[74] R. Plunkett, *Proceedings of the 1991 Lepton-Photon Conference*, Geneva, (1991)
[75] F. Abe et al, PRL 67 (1991), 2418
[76] A. Beretvas, *Proceedings of the 1990 Summer Study on High Energy Physics*,

Snowmass (1990)
[77] H. Baer et al, University of Wisconsin preprint MAD/PH/540 (1990)
[78] K. Kondo, Journal of the Phys.Soc.Japan 57 (1988), 4126
[79] S.L. Glashow and E.E. Jenkins, PL B196 (1987), 233
V. Barger and R.J.N. Phillips, PR D40 (1989), 2875
[80] C.S. Kim, J.L. Rosner, and C.P. Yuan, PR D42 (1990), 96

DATE
FILMED
3 / 10 / 92